Novel Angular Domain Spectroscopic Analysis Devices and Techniques

by

Yan Zhang

M.A. Sc., Simon Fraser University, 2005
B.Sc., Tsinghua University, 2000

Thesis Submitted in Partial Fulfillment

of the Requirements for the Degree of

Doctor of Philosophy

in the

School of Engineering Science

Faculty of Applied Sciences

© Yan Zhang 2013

SIMON FRASER UNIVERSITY

Fall 2013

Approval

Name: **Yan Zhang**

Degree: **Doctor of Philosophy**

Title of Thesis: ***Novel Angular Domain Spectroscopic Analysis Devices and Techniques***

Examining Committee:

Chair: **Dr. Faisal Beg**
Associate Professor, P. Eng.

Dr. Bozena Kaminska
Senior Supervisor
Professor

Dr. Karen L. Kavanagh
Supervisor
Professor

Dr. Carlo Menon
Internal Examiner
Professor
School of Engineering Science

Dr. Alexandre Brolo
External Examiner
Associate Professor, Chemistry Department
University of Victoria

Date Defended: Dec 10, 2013

Partial Copyright Licence

SFU

Abstract

The first objective of this thesis is to design, fabricate and characterize Radial Angular Filter Arrays (RAFAs). The motivation is to replace bulky and slower goniometer-based instruments or complicated interferometric systems to achieve low-cost, real-time and simplified optical scattering measurement. In addition, RAFAs are designed to support angle-resolved spectroscopic analysis for structural characterization, bio-sensing, and material identification. RAFAs originate from Angular Filter Array (AFA) in Angular Domain Imaging (ADI). They consist of radially-distributed micro-machined channels in a silicon substrate. Each channel collects photons emitted from the focal point at a specific angle and only passes through photons traveling within a small acceptance angle of the channel direction. This angular filtering function is independent of photon wavelength in the visible and near infrared range. A RAFA provides a means to obtain both angular and spectral information of scattered light in a single exposure. The primary contribution of this thesis project in this field is to develop a RAFA from a concept to a fully functioning device, which expands the applications of AFA beyond biomedical imaging and facilitates the applications of angular spectroscopy. A novel optical characterization system based on both Nano Hole Arrays and RAFAs for potential Surface Plasmon Resonance sensing applications is proposed and tested.

The second objective of this thesis is to advance the angular domain spectroscopic analysis in the biomedical imaging field by applying the multi-spectral analysis to reflectance ADI setups other than the conventional transillumination systems. This new technique allows non-invasive *in vivo* angular domain spectroscopic imaging samples too thick to perform transillumination. The contribution in this field is to add spectroscopy to the existing Deep-Illumination ADI system. A series of improvements in setup and image processing are practiced to enable Deep-Illumination Angular Domain Spectroscopic Imaging (DI-ADSI) for tissue-mimicking phantoms. The results obtained demonstrate that its depth penetration, field of view and spatial resolution are between micro-reflectance-imaging technologies such as Optical Coherent Tomography and Confocal Microscopy, and macro-reflectance-imaging technologies such as Diffuse Optical Tomography, satisfying the value-proposition of DI-ADSI. It suggests that DI-

ADSI has the potential for low-cost and fast *in vivo* tissue scanning for superficial targets.

Dedication

This thesis is dedicated to my beloved family and friends who gave me exceptional support, determination, and enthusiasm in the past 10 years.

Acknowledgements

Table of Contents

List of Tables

List of Figures

xvi

xviii

List of Acronyms

2D	Two Dimensional
3D	Three Dimensional
ADFI	Angular Domain Fluorescent Imaging
ADI	Angular Domain Imaging
ADSI	Angular Domain Spectroscopic Imaging
AFA	Angular Filter Array
BSDF	Bidirectional Scattering Distribution Function
BRDF	Bidirectional Reflectance Distribution Function
BTDF	Bidirectional Transmission Distribution Function
CM	Confocal Microscopy
CT	Computered Tomography
CW	Continuum Wave
dd-H2O	Distilled-Deionized Water
DI-ADI	Deep Illumination Angular Domain Imaging
DI-ADSI	Deep Illumination Angular Domain Spectroscopic Imaging
DOT	Diffuse Optical Tomography
EOT	Extraordinary Optical Transmission
FDTD	Finite Difference Time Domain
FWHM	Full Width at Half Maximum
Hb	Hemoglobin
HbO	Oxygenated Hemoglobin
ICG	Indocyanine Green
LDV	Laser Doppler Velocimetry
MFP	Mean Free Path
MRI	Magnetic Resonance Imaging
NHA	Nano-Hole Array
NIR	Near Infrared
OA	Optical Axis
OCT	Optical Coherent Tomography
OT	Optical Tomography
PAM	Photoacoustic Microscopy

PBS	Phosphate-Buffered Saline
PCS	Photo Correlation Spectroscopy
PDA	Phase Doppler Anemometry
PET	Positron Emission Tomography
PIDS	Polarized Intensity Differential Scattering
PSF	Point Spread Function
QTH	Quartz Tungsten Halogen
ROC	Receiver Operating Characteristic
RTE	Radiative Transport Equation
RAFA	Radial Angular Filter Array
SERS	Surface Enhanced Raman Spectroscopy
SNOM	Scanning Near-field Optical Microscope
SNR	Signal-to-Noise Ratio
SPECT	Single Photon Emission Computed Tomography
SP	Surface Plasmon
SPC	Specificity or True Negative Rate
SPP	Surface Plasmon Polariton
SPR	Surface Plasmon Resonance
TD	Time-Domain
TPR	True Positive Rate

1.   Introduction

This thesis is the exploration of angle-resolved spectroscopic analysis in both imaging and non-imaging fields. The proposed devices and techniques are aimed at working with bio-medical turbid samples in visible and near-infrared spectra. However, their applications could be extended to other circumstances wherever the angular and spectroscopic information need to be processed or analyzed simultaneously.

This chapter will first provide an overview of photon transport models with detailed discussion on the interactions between photons and turbid media. This guides the development of angular spectroscopic analysis techniques. Then, the common methods utilized for optical scattering characterization systems and their limitations will be described. The primary motivation of this thesis is to develop angle-resolved spectroscopic analysis devices and techniques to overcome such short-comings and generate new applications. Subsequent sections will introduce the angular domain analysis in imaging fields: Angular Domain Imaging (ADI) and Angular Domain Spectroscopic Imaging (ADSI). The current progress in both areas will be reviewed. The chapter will conclude with the objectives of the research and an outline of the thesis.

1.1. Photon Transmission and Scattering Theory

1.1.1.   The Radiation Transport Model

A photon is an elementary particle and the quantum of light. Photons are known to have wave-particle duality. The propagation of radiation through a medium is affected by absorption, emission, and scattering processes. The radiation transport model describes these interactions mathematically in the Radiative Transfer Equation (RTE) [1, 2, 3]:

$$\frac{\partial I(r,\Omega,t)}{c\partial t} + \Omega \cdot \nabla I(r,\Omega,t) = -\mu_{ext}I(r,\Omega,t) + \mu_{em} + Q(r,\Omega,t)\,, \tag{1.1}$$

where $I(r,\Omega,t)$ represents the specific radiative intensity with units of Wm^{-2}sr^{-1} at distance, r, propagating in the fixed direction, $\Omega(\vartheta,\varphi)$, and at time, t, per solid angle and per unit area normal to direction Ω (Fig. 1-1). The first item at the left side of the equation represents the time variation of $I(r,\Omega,t)$ and the second item describes the space variation. μ_{ext} and μ_{em} are the extinction and emission coefficients. $Q(r,\Omega,t)$ represents the radiative source inside the medium. The decrease in intensity is caused by the removal of photons in direction $\Omega(\vartheta,\varphi)$ due to their absorption and scattering to other directions. This process is described by the first term at the right side of the Equation (1.1). Thus, the value of μ_{ext} can be divided into two parts:

$$\mu_{ext} = \mu_a + \mu_s \, , \tag{1.2}$$

where μ_a and μ_s are absorption and scattering coefficients with the unit of cm^{-1}. These values are proportional to the particle concentration, N, the absorption cross-section, C_{abs}, and the scattering cross-section, C_{sca}. A parameter named as Albedo is defined as the relative strength between the scattering and absorption [1, 3]:

$$albedo = \frac{\mu_s}{\mu_a + \mu_s} \, . \tag{1.3}$$

The second item at the right side of Equation (1.1) is the emission coefficient, μ_{em}, and it consists of two parts:

$$\mu_{em} = \mu'_{em} + \mu''_{em} \, , \tag{1.4}$$

where μ'_{em} is due to the internal sources of radiation and μ''_{em} accounts for photons scattered from the other direction to this direction. μ'_{em} could be presented by the Planck function:

$$\mu'_{em} = B(T) = \frac{2h\upsilon^3}{c^2} \frac{1}{e^{h\upsilon/kT} - 1} \, , \tag{1.5}$$

where T is the temperature, υ is the frequency, c is the speed of light, h and k are the Boltzmann and Planck constants. μ''_{em} could be presented by the function below:

$$\mu''_{em} = \int_{4\pi} \delta(\Omega, \Omega') I(\Omega') d\Omega' \, , \tag{1.6}$$

where $\delta(\Omega,\Omega')$ is the differential scattering cross-section from direction $\Omega'(\vartheta',\varphi')$ to $\Omega(\vartheta,\varphi)$. $\delta(\Omega,\Omega')$ is the geometrical cross-section of a particle, which would produce an amount of scattering equal to the observed scattered power between Ω and Ω'. μ_s and $\delta(\Omega,\Omega')$ satisfy:

$$\mu_s = \int_{4\pi} \delta(\Omega, \Omega')d\Omega' \ . \tag{1.7}$$

Besides $\delta(\Omega,\Omega')$, $p(\Omega,\Omega')$ is another parameter that describes the angular distribution of the scattered field. $p(\Omega,\Omega')$ is defined as the scattering phase function that represents the probability for a photon propagating in direction Ω to be scattered into Ω'. $p(\Omega,\Omega')$ is proportional to the ratio between $\delta(\Omega,\Omega')$ and the total scattering cross-section, δ_s, across all angles and normalized such that the integral over all angles of scattering equals one [4]:

$$\int_{4\pi} p(\Omega, \Omega')d\Omega' = 1 \ . \tag{1.8}$$

Thus,

$$p(\Omega, \Omega') = \frac{\delta(\Omega',\Omega)}{\mu_s} \ . \tag{1.9}$$

For isotropic media, the cross-section $\delta(\Omega,\Omega')$ in Equation (1.6) is only related to the scattering angle, θ:

$$\cos\theta = \cos\vartheta \ \cos\vartheta' + \ \sin\vartheta \ \sin\vartheta' \ \cos(\varphi - \varphi') \ . \tag{1.10}$$

Thus, $p(\theta)/4\pi$ represents the probability of photon scattering from one direction to direction Ω at the scattering angle of θ [1]:

$$p(\theta) = \frac{4\pi\delta(\theta)}{\int_0^{2\pi} d\varphi \int_0^{\pi} \delta(\theta)sin\theta d\theta} \tag{1.11}$$

and

$$\frac{1}{2}\int_0^{\pi} p(\theta)sin(\theta)d\theta = 1 \ . \tag{1.12}$$

In the end, Equation (1.1) can be updated as:

$$\frac{dI(r,\Omega,t)}{cdt} + \Omega \cdot \nabla I(r,\Omega,t) = -(\mu_a + \mu_s)I(r,\Omega,t) + \mu_s \int p(\Omega,\Omega')\, I(r,\Omega,t)d\Omega' +$$

$$Q(r,\Omega,t) \ . \tag{1.13}$$

Please note that μ'_{em} is ignored in this thesis as it is often not important in the visible and near infrared range and $B(T)$->0 [1].
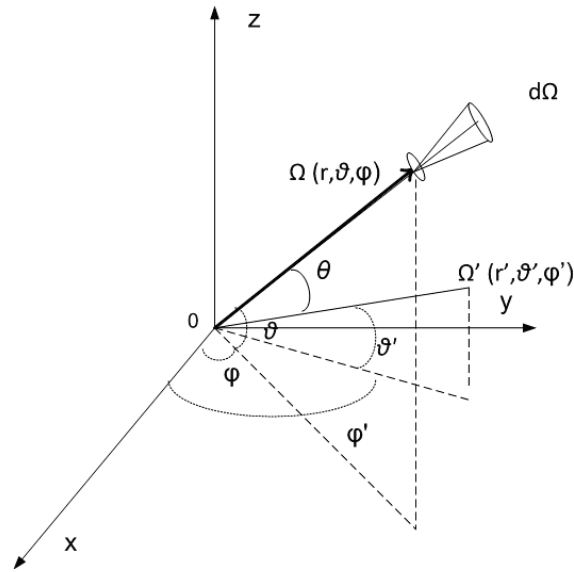
Fig. 1-1 Light energy propagates along the direction Ω and Ω'

1.1.2. *Light matter interaction*

Light propagates in a fixed direction in the vacuum without energy loss until it encounters the interface with a medium. It causes the charges to oscillate and thus emit additional light waves in any directions as scattering. The interference can happen between the incident beam and the emitted beams. If it is destructive, the incident light is attenuated or absorbed. The interference might be constructive in certain directions, forming reflected or transmitted light [1, 5].

As the light propagates inside the medium, the photon can either transmit ballistically if it does not encounter any particles, or be absorbed or be scattered as described above (Fig. 1-2). While it is absorbed due to resonant with some molecular transitions, that molecule will absorb the photon energy and transform it to heat or fall apart due to photo-chemical process or emit extra energy as a photon. The later is called fluorescence [2, 5]. Scattering involves both the properties of the light and those of the

medium. Multiple scattering processes exist and in general, they could be categorized into either elastic processes or inelastic processes. Inelastic process involves permanent energy exchange between the light and the medium at the scattering location while the elastic process does not. An overview of major scattering processes are listed in Ref. [5] (Table 1-1). The scattering intensity is wavelength dependent. In the regime of Reyleigh scattering, where particle dimension is much smaller than the wavelength of light, the scattering intensity is inversely proportional to the fourth power of the wavelength [1, 5, 6].

Table 1-1   Major scattering processes [5]

Scattering or other process	Scatterer	Frequency shift δv/v	Comments
Mie scattering	Particles, which is large compared to the wavelength (dust, soot and etc)	0	Elastic process
Rayleigh-scattering	Particles, which are small to the wavelength (molecules, micro-particles)	0	Elastic process
Bragg-scattering	Structure of crystals	$\pm(10^{-4} \sim 10^{-2})$	Elastic process but frequency shift connected to Brillouin scattering
Brillouin-scattering	Acoustic vibration in crystals and liquids	$\pm(10^{-6} \sim 10^{-5})$	Inelastic process
Raman-scattering	Molecules	$\pm(10^{-5} \sim 10^{-1})$	Inelastic process. Incident photon perturbs the molecule vibration or rotational energy states
Compton-scattering	Molecular vibration optical lattice vibration	$\pm(10^{-3} \sim 10^{-2})$	Inelastic process, high energy photons interacts with the electron closely bounded in the atom
Fluorescence	Atoms, molecules	$\pm(0 \sim 10^{-2})$	Absorption and re-emission

Scattering direction is also determined by the medium properties. The anisotropy coefficient *g* represents the direction where the photons will be scattered to:

$$g = \frac{\int_{4\pi}(\Omega,\Omega')\mathrm{p}(\Omega,\Omega')\mathrm{d}\Omega'}{\int_{4\pi}\mathrm{p}(\Omega,\Omega')\mathrm{d}\Omega'} = < cos\theta >. \tag{1.14}$$

g will be 0 in isotropic medium. *g* = 1 for 100% forward scattering and -1 for 100% backward scattering. When *g* value is high, most photons will be scattered to the original propagating direction. This case is named as quasi-ballistic scattering [2, 7] (Fig. 1-2).
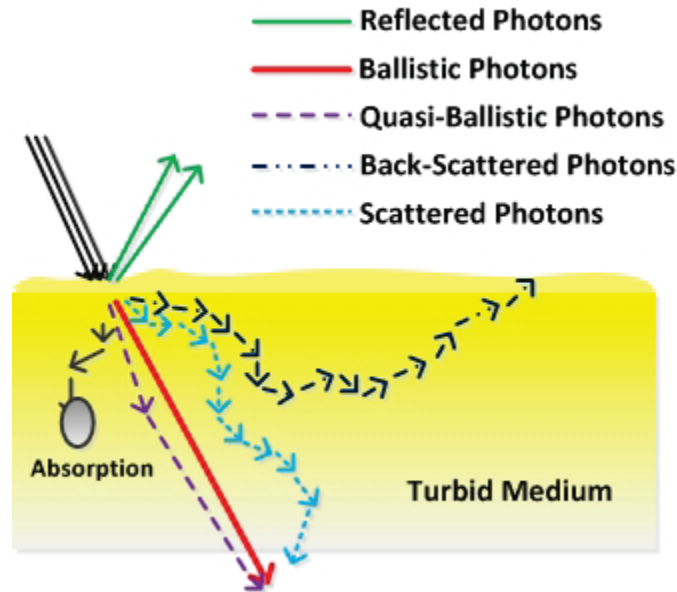
Fig. 1-2 Photon interacts with a turbid medium

1.1.3. *Light transport model in turbid medium*

Turbid medium includes clouds, fog, smoke, suspensions, emulsions, colloidal solutions and most biological tissues. A light wave incident into a turbid medium may be scattered consecutively by a number of optical non-uniformities before leaving the medium. Single scattering is observed only for a low optical thickness τ (for example $\tau \leq$ 0.1)[1], which is defined as the negative natural logarithm of the faction of radiation that is not scattered or absorbed on a path. The problem of light scattering in highly turbid media of thick optical thickness could be modeled in one of two basic ways: an essentially discrete model of individual photon interactions, such as Monte Carlo or a continuous model based on a RTE (Equation (1.13)) [8].

This section will review the light transport in a turbid medium using the RTE model. In Equation (1.13), there are six independent variables: *x*, *y*, *z* from *r*, polar angle ϑ and azimuthal angle φ from Ω, and *t*. Analytic solutions of RTE are difficult and typically exist only for simple geometries. However, these difficulties can be reduced by considering approximate solutions that leads to the reduction of the number of independent variables in RTE. One approximation is made in an infinite, isotropic and homogeneous medium without any light source, if the scattering from other direction Ω' to the propagating direction Ω is neglected, Equation (1.13) will transform to Beer-Lambert Law [9]:

$$\frac{dI(r)}{dr} = -(\mu_a + \mu_s)I(r) \ .$$

(1.15)

Diffusion approximation is a more accurate model which makes appropriate assumptions about the behaviour of photons in a high-albedo turbid medium. The approximation is performed with the scattering between different directions and the radiative sources inside the medium.

In a high albedo medium, scattering is predominant. There are very few absorption events relative to scattering events. Thus, the time for substantial flux change is much longer than the time to traverse one transport mean free path. In addition, the radiance will become nearly isotropic after numerous scattering events, also called directional broadening [1, 3, 8, 10]. This isotropic scattering is described by the reduced scattering coefficient, μ'_s:

$$\mu'_s = \mu_s(1 - g) \ .$$

(1.16)

The purpose of the introduction of μ'_s is to describe diffusion of photons in a random walk of step size of $1/\mu'_s$ (reduced mean free path) where each step involves isotropic scattering. This isotropic scattering step is the accumulation of many small anisotropic steps with the mean free path of $1/\mu_s$. The mean number of anisotropic steps can be estimated by $1/(1-g)$.

The next step of approximation is known as the P_N approximation in the spherical coordinates. The method of the P_N approximation is simply to expand the radiance,

phase function, and light source in spherical harmonics $Y_{l,m}$, truncating the series for the radiance at $l=N$ [1, 3]. The radiance and light source are expanded as

$$I(r,\Omega,t) = \sum_{l=0}^{N} \sum_{m=-l}^{l} \phi_{l,m}(r,t) Y_{l,m}(\Omega) \; , \tag{1.17}$$

$$Q(r,\Omega,t) = \sum_{l=0}^{N} \sum_{m=-l}^{l} q_{l,m}(r,t) Y_{l,m}(\Omega) \; , \tag{1.18}$$

where,

$$\phi(r,t) = \int I(r,\Omega,t) d\Omega \; . \tag{1.19}$$

In addition,

$$J(r,t) = \int I(r,\Omega,t)\Omega d\Omega \; , \tag{1.20}$$

$\phi(r,t)$ is the fluence rate which is the energy flow per unit area per unit time regardless of the flow direction. $J(r,t)$ is the photon flux or current density. Both the fluence and the flux have units of W/m^2.

$q_{l,m}(r,t)$ in Equation (1.18) is the different angular moments of the source at position r and time t. $Y_{l,m}(\Omega)$ in Equation (1.18) is defined as

$$Y_{l,m}(\Omega) = Y_{l,m}(\vartheta,\varphi) = \sqrt{\frac{2l+1}{4\pi} \frac{(l-m)!}{(l+m)!}} P_l^m(\cos\vartheta) e^{im\varphi} \; , \tag{1.21}$$

$P^m{}_l$ is an associated Legendre Polynomial of order l with a complex constant, m, and

$$Y_{0,0}(\vartheta,\varphi) = \frac{1}{\sqrt{4\pi}} \; , \tag{1.22}$$

$$Y_{1,-1}(\vartheta,\varphi) = \sqrt{\frac{3}{8\pi}} \sin\vartheta e^{-i\varphi} \; , \tag{1.23}$$

$$Y_{1,0}(\vartheta,\varphi) = \sqrt{\frac{3}{8\pi}} \cos\vartheta \; , \tag{1.24}$$

$$Y_{1,1}(\vartheta,\varphi) = -\sqrt{\frac{3}{8\pi}} \sin\vartheta e^{i\varphi} \; , \tag{1.25}$$

$Y_{0,0}$ is the isotropic component. $Y_{1,-1,}$, $Y_{1,0,}$and $Y_{1,1}$ are the anisotropic components with P_1 approximation [3, 11]. Substituting Equation (1.17) into (1.19), With P_1 approximation, we obtain

$$\phi(r,t) = 4\pi I_{0,0}(r,t)Y_{0,0}(\Omega) . \tag{1.26}$$

It means that the isotropic term is equal to the fluence rate divided by the entire 4π solid angle. We also have

$$\int_{4\pi} \Omega_i d\Omega = 0 , \tag{1.27}$$

$$\int_{4\pi} \Omega_i \Omega_j d\Omega = \frac{4\pi}{3} \delta_{ij} , \tag{1.28}$$

$$\int_{4\pi} \Omega_i \Omega_j \Omega_k d\Omega = 0 , \tag{1.29}$$

where $\delta i,j = 0$ if $i{\neq}j$ and 1 if $i{=}j$ [12]. Substituting Equation (1.17) into (1.20), considering the property of spherical harmonics and with P_1 approximation, we obtain

$$J(r,t) \cdot \Omega = \frac{4\pi}{3} \sum_{m=-1}^{1} I_{1,m}(r,t)Y_{1,m}(\Omega) . \tag{1.30}$$

From Equation (1.19), (1.20), (1.26), and (1.30), we obtain:

$$I(r,\Omega,t) = \frac{1}{4\pi} \phi(r,t) + \frac{3}{4\pi} J(r,t) \cdot \Omega , \tag{1.31}$$

$$Q(r,\Omega,t) = \frac{1}{4\pi} Q_0(r,t) + \frac{3}{4\pi} Q_1(r,t) \cdot \Omega , \tag{1.32}$$

$Q_0(r,t)$ and $Q_1(r,t)$ are the monopole (isotropic) isotropic and dipole moments of the source [3]. If the scattering amplitude is only dependent on the change in direction of the photon and the phase function could be updated as

$$p(\Omega,\Omega') = \sum_{l=0}^{\infty} \frac{2l+1}{4\pi} g_l P_l(\Omega,\Omega') = \sum_{l=0}^{\infty} \sum_{m=-l}^{l} g_l Y_{l,m}^{*}(\Omega') Y_{l,m}(\Omega) , \tag{1.33}$$

where $g_0 = 1$ and $g_1 = <cos\theta>$ after the normalization [3].

P_1 approximation is acceptable when the albedo is close to unity and the phase function is not too anisotropic ($g_1<0.99$), and the source-detector separation is large

9

compared to *1/(μ_s(1-g_1))* [3]. From Equation (1.17), (1.19), (1.20), (1.22), (1.23), (1.24), (1.27) and (1.31), we obtain the following equation under diffusion approximation [13]:

$$\int_{4\pi} p(\Omega, \Omega') I(r, \Omega, t) d\Omega' = \int_{4\pi} \left[g_0 \frac{1}{4\pi} + g_1 \sum_{m=-1}^{1} Y_{1,m}^*(\Omega') Y_{1,m}(\Omega) \right] \left[\frac{1}{4\pi} \phi(r, t) + \frac{3}{4\pi} J(r, t) \cdot \Omega \right] d\Omega' = \frac{\phi(r,t)}{4\pi} .$$

(1.34)

From Equation (1.27), (1.28) and (1.30) we obtain:

$$\int_{4\pi} \Omega \cdot \nabla I(r, \Omega, t) d\Omega = \int_{4\pi} \Omega \cdot \nabla \left[\frac{1}{4\pi} \phi(r, t) + \frac{3}{4\pi} J(r, t) \cdot \Omega \right] d\Omega = \nabla J(r, t) .$$

(1.35)

Finally, derive from RTE Equation (1.13) with Equation (1.32), (1.34) and (1.35), then integrate over Ω:

$$\frac{d\phi(r,t)}{cdt} = -\mu_a \phi(r, t) - \nabla \cdot J(r, t) + Q_0(r, t) ,$$

(1.36)

The above is the scalar form of the RTE. In order to review the vector form, multiply Ω to both sides of Equation (1.13) and integrate over the entire solid angle of 4π, using Equation (1.13), (1.17), (1.27), (1.28), (1.29), (1.31), (1.32), (1.33), (1.34), (1.35), and diffusion approximation [13], we obtain

$$\frac{dJ(r,t)}{cdt} = -(\mu_a + \mu'_s) J(r, t) - \frac{1}{3} \nabla \cdot \phi(r, t) + Q_1(r, t) ,$$

(1.37)

According to diffusion approximation, the flux change is negligible within one mean free path. Thus, Equation (1.37) reduces to Fick's Law (assuming no additional light source) in which the flux is proportional to the gradient of fluence rate.

$$J(r, t) = -\frac{1}{3(\mu_a + \mu'_s)} \nabla \cdot \phi(r, t) = -D \nabla \cdot \phi(r, t) ,$$

(1.38)

where *D = 1/3(μ_a+μ'_s)*. Plug Equation (1.38) into (1.36) and assume there is not any radiative source:

$$\frac{d\phi(r,t)}{cdt} = -\mu_a \phi(r, t) + D \nabla^2 \cdot \Phi(r, t) .$$

(1.39)

The scattering coefficient and scattering anisotropy do not explicitly appear in Equation (1.39). Instead, they appear together in the reduced scattering coefficient in *D*, indicating that diffusion is unaffected if the anisotropy of the scattering medium is changed while the reduced scattering coefficient stays the same.

Phase function reveals the angular distribution of the photons after scattering. The analytic model of phase function would help to quantify the scattering events inside the turbid medium. Ref [14] reveals that the following equation, named as Henyey and Greenstein (HG) function, developed in Ref [15] to characterize the angular distribution of light after scattering due to small particles in interstellar dust clouds, could also accurately characterizes the scattering in a turbid biological medium:

$$p(g,\theta) = \frac{1-g^2}{4\pi(1+g^2-2g\cos\theta)^{3/2}} \; .$$
(1.40)

For biological turbid media, *g* ranges from 0.4 to 0.99 [16]. Equation (1.40) is one-term HG function, for applications that one term HG function is not sufficiently accurate, a two-term HG functions could be used and the details are explained in Ref [9, 17].

1.2. Optical Scattering Characterization System

1.2.1. *Optical scattering characterization functions*

The accurate knowledge of optical scattering at specific angles is the target of angular optical scattering characterization as the scattered photons carry both angular and spectroscopic information that facilitates to characterize the medium [5]. The measurement results are typically presented in Bidirectional Scattering Distribution Functions (BSDF) which could be further explained as Bidirectional Reflectance or Transmission Distribution Functions (BRDF or BTDF) [6]. BSDF is treated as a black box with two inputs, one for incoming (incident) ray and the other for the outgoing (reflected or transmitted) ray at a given point where the scattering occurs. The angle of the output ray is defined as the difference between the scattered direction and the normal direction (Fig. 1-3(a)). The output of this black box is the ratio between the incoming and the

outgoing light energies. Further study reveals that the BSDF function could be presented as,

$$BSDF \cong \frac{P_s / \Omega_s}{P_i \cos\theta_s} \ ,$$

<div align="right">(1.41)</div>

where P_i is the incident beam power per source area and P_s is the scattered beam power per source area in the solid angle Ω_s. The projected solid angle in a specific direction is Ω_s times $cos\theta_s$ where θ_s is defined as the angle between the scatter direction and the normal direction (Fig. 1-3(b)). The $cos\theta_s$ factor could be also reviewed as the correction to the illumination area, whose apparent size from the scatter direction deviates from the actual size by a factor of $cos\theta_s$ [6].
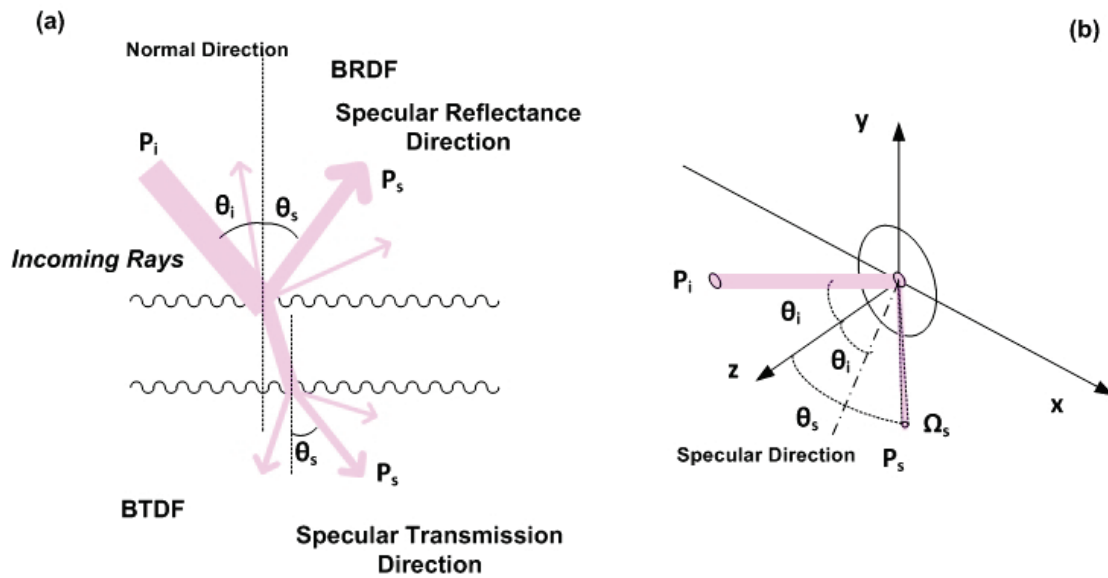
Fig. 1-3 (a) BRDF, BTDF and the specular direction. (b) A scattering event in 3 dimension

Both BRDF and BTDF and Equation (1.41) are directly measurable when a scattering event happens. They present the angular distribution of photons in regards to the specular direction after the scattering event and can be correlated to the surface or the transmission properties of medium. Ref [6] listed a series of measured BSDFs for different optical components and demonstrated that BSDFs vary with even subtle changes in surface roughness, crystal structure, bulk index fluctuation and particularly photon wavelength. There are two BSDF measurement standards developed by ASTM

committee, SEMI ME1392, "Guide for angle resolved optical scatter measurements on specular or diffuse surface", and ASTM E2387, "Standard practice for goniometric optical scatter measurement". Both standards consider that the angular distribution of scatter is a property of the surface or the medium, and they define how to characterize this property by measuring BSDF.

While most optical scattering characterization systems focus on measuring the BSDF, some specific systems are not. Instead, they typically utilize multiple incident beams and try to quantify target properties via the interaction between these incident beams after scattering. For example, Laser-Doppler Velocimetry is an optical measuring method which allows the determination of the velocity of a fluid with a very high temporal solution [5]. In this case the velocity is the function of photon wavelength, frequency doppler shift and the angle between two incident beams.

1.2.2. Optical scattering characterization system

Conventionally, in order to measure the angular distribution of the photons and BSDF, a goniometer type of instrument was employed with which either the detector or the sample was rotationally scanned over all angles (Fig. 1-4 (a)) [6, 16, 17, 20, 20, 23]. The measurement of angular distribution of scattered photons has broad applications in numerous industries. Ref [6] describes a typical BSDF scatterometer with a motorized receiver-rotation stage to provide the characterization capability over nearly the entire angular range. This scatterometer was used to quantify and correct the scatter loss of the mirrors in high precision optical characterization systems. In semiconductor industry, BSDF measurement is a useful tool to evaluate the surface roughness and can help to find small particulates and point defects on polished surface [6, 18, 20]. In metal processing industry, optical scattering measurement is practical to measure the temperature via tracing the surface deformation due to heat or control the quality of metal surface[6, 20]. In Solar industry, scattering measurement is the primary tool to evaluate the haze in solar cell which is critical to cell efficiency [29]. The material characterization process performed with optical scattering system is non-invasive and it allows a lot of applications in biomedical field. For instance, it becomes the primary approach to evaluate the retinal degradation inducted by intraocular lens aging [6]. Particle counting and characterization are other popular applications of optical scattering

13

measurement. Classical (static) light scattering characterization measures the intensity of the scattered light as a function of angle. For macromolecules, this method can yield the molar mass, root-mean-square radius and second virial coefficient via Rayleigh scattering model [32]. Photon Correlation Spectroscopy (PCS) is a technology for measuring the dynamic light scattering (quasi-elastic light scattering) of small scatters in a suspension and can determine the hydrodynamic radius of macromolecules or particles [28, 32, 33]. Ref [28] also presented Phase Doppler Anemometry (PDA) as a particle characterization tool. It was based a well-established flow measurement technology - Laser Doppler Velocimetry [5]. With PDA, detectors rotate around the direction of flow at the opposite side of the incident beam.

The goniometer type of setup is a complex system which involves a motor or stepper and the alignment is very challenging. Furthermore, the measurement with such system is a time-consuming process due to the large number of scanning steps. There are also practical difficulties with configurations that move the sample or the source during the measurement. If the sample is optically smooth, the reflected beam will sweep the entire testing area. It will be a safety hazard in particular when laser source is implemented. One solution is to use multiple detectors at different angles to obtain all signals at once (Fig. 1-4 (b)) [19]. Ref [28] demonstrated a PCS system with multiple detectors aligned to focus the sample cell. Another alternative approach is to use a video camera to obtain the entire light distribution at once or to use raster scans (Fig. 1-4 (c)). In this case, additional tools are needed to couple photons propagating in different directions into the same camera, e.g. fiber optics bundles around the sample or lenses with large numerical apertures [19, 20, 22, 28]. Ref [22] reported to use a fiber to provide illumination to the skin and measure the diffusive reflectance via the neighbouring fibers around the source fiber in the same bundle. The chapter 3 in Ref [28] introduced a polarization intensity differential scattering system that obtains the particle size distribution through measurements of scattering intensity as a function of the scattering angle and the wavelength of light based on applicable scattering models. In this system, the laser beam is projected to the sample module and the scattered light is collected by a lens.

In some applications, where the measurement of the entire angular distribution of photons is not critical but the measurement speed, instrument size and cost are critical,

optical scattering characterization system is designed to only measure the light scattered to some particularly directions. Though the full BSDF will not be obtained, such system has proven to be sufficient in many applications. In paper and pulp industry, the paper flaw detection is mainly conducted by a simplified optical scattering measurement that focuses on the light change at specular direction only [6]. Ref [24] describes an application for using multi-spectral imaging prototype for real-time detection of fruit firmness. In this case, a light beam scattered to the side at a specific angle is spectrally analyzed.

Optical scattering measurement is also often combined with other optical characterization systems. As an emerging biomedical imaging technology, angle-resolved low coherence interferometry has demonstrated its capability to measure the average size of the cell structures using the properties of scattered light in a coherent system. In such system, the illumination beam and the scattered lights are provided and collected by an fiber optics bundle with micro-lens, respectively. The obtained angular scattering distributions are compared to the prediction of Mie theory. The comparison results could be transformed to quantitative morphological and optical scattering information for features. Furthermore, like optical coherent tomography, the depth resolution of the cell targets inside the tissue samples could be measured according to the differences in the optical path [25, 26, 27].

1.2.3. Angle-resolved spectroscopic measurement system

As described in section 1.1.2, besides the directional change, energy exchange occurs while the scattering is inelastic. Spectroscopic analysis is able to characterize such process. In addition, it will provide the absorption information of the material under study. Thus, the spectroscopic analysis has become necessary in a lot of optical scattering measurement applications.

Angle-resolved spectroscopic analysis can be conducted by simply using a spectrometer to replace the regular photodetector or use multiple spectral filters in the setup. In Ref [6], a Rayleigh scattering measurement is employed to evaluate air pollution. Low contamination and pollution levels can be detected by measuring the variations in scattering signal at wavelengths in and near contaminant absorption bands.

Spectroscopy is used to identify the contamination material and scattering is used to provide the signal and subsequent analysis. As described in the section above, the optical scattering measurement system could determine the fruit firmness via measuring just one scattering angle. It is possible only because the spectroscopic analysis is added to compensate the loss in angular information [24]. Ref [28] presents the improvement of Polarized Intensity Differential Scattering (PIDS) measurement limit to as low as 50 nm, almost reaching the theoretical limit via combining polarization effects with wavelength dependence at large angles.
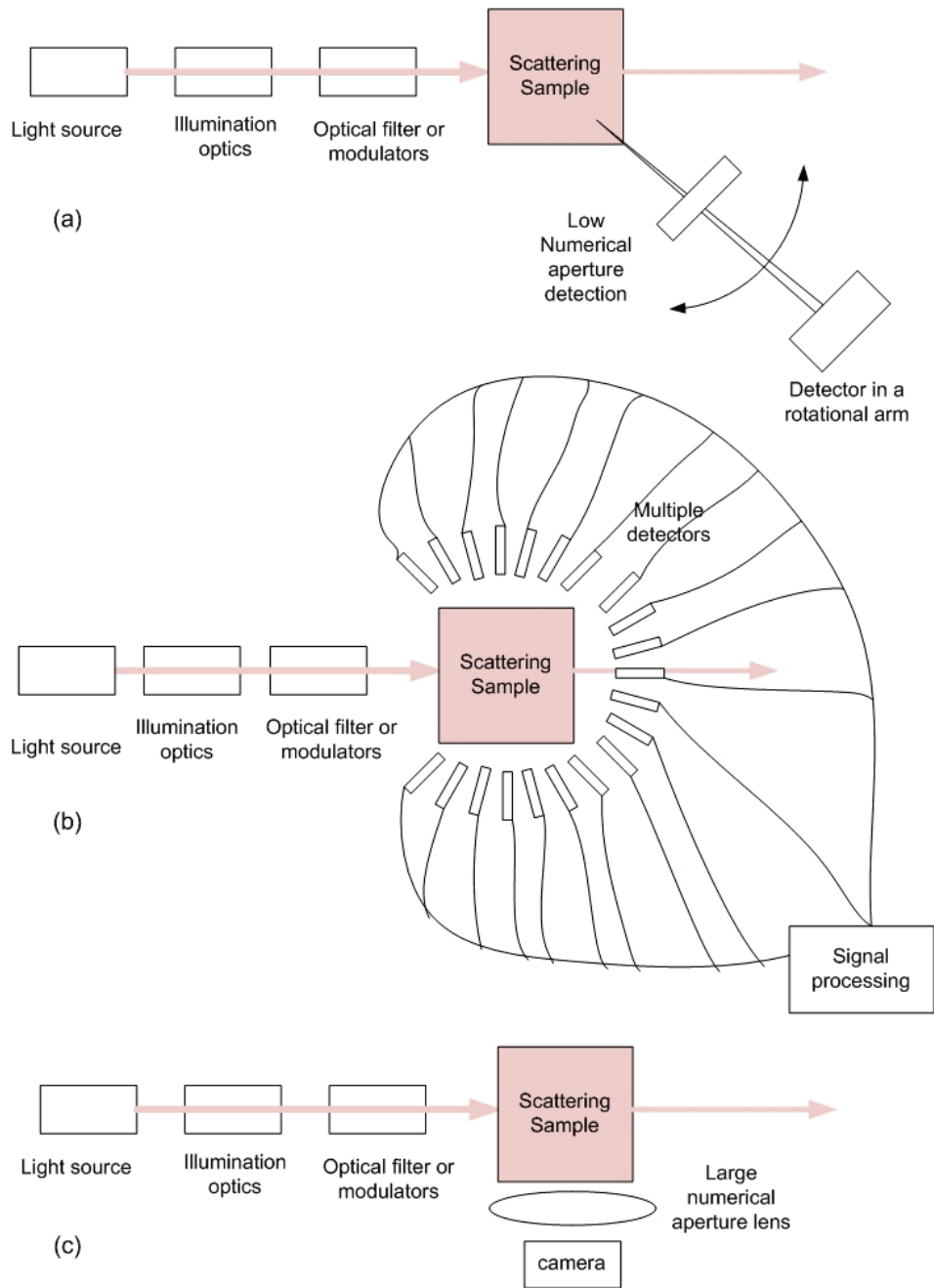
Fig. 1-4 Principle behind experimental setups for collecting angular scatter (a) scanning goniometer (b) multi-detector setup (c) camera setup.

Spectroscopic analysis is an essential part of the biomedical optical scattering measurement as well. Recently, light scattering systems have been used for applications such as the study of cellular morphology [35] as well as the diagnosis of dysplasia [34]. Both applications were based on the variations in scattering distributions as a function of

17

angle and wavelength. These relationships revealed that the information regarding the size of cells and subcellular objects such as nuclei and organelles, and helped to diagnostically detect tissue changes which might lead to cancer. Spectroscopic analysis also facilitates angle-resolved low coherence interferometry as both μ_s and μ_a are wavelength dependent. Ref [26] uses both low-coherence spectroscopy and Mie theory calculation to obtain the μ_s and μ_a of the media with varying scattering properties and containing different sized polystyrene spheres. Ref [27] further expands upon low-coherent interferometry by introducing spectroscopic information as an additional tool for diagnosing pre-cancerous cellular states.

1.3. Angular Domain Imaging (ADI) and Angular Domain Spectroscopic Imaging (ADSI)

This thesis will focus on angular domain spectroscopic analysis, particularly its applications in biomedical samples. The technology is originated from two optical tomography (OT) modalities: Angular Domain Imaging (ADI) and Angular Domain Spectroscopic Imaging (ADSI). Both of them are Optical Tomography (OT) techniques that are developed to replace low resolution X-ray screening in areas such as mammograms and brain scans. Besides the advancement in novel angular domain filter devices and their applications, this thesis will also improve the ADI and ADSI using the developed technology.

1.3.1.   Optical tomography modalities

According to Fig. 1-2, photons traveling in a turbid medium experience one of the following processes: reflection, low angle scattering (ballistic/quasi-ballistic trajectories), large angle scattering, and absorption [5, 7]. Optical tomography is a technique that creates a digital model of an object by reconstructing images made from those photons transmitted or scattered through the object. The interaction between the photons and the object is described by the object's absorption and scattering properties. The unique feature of these properties in specific spectra could be used to characterize the cellular morphology of biological tissues. In addition, the change in these optical properties is

typically associated with abnormal physiological activities. Thus, optical tomography modalities have become important tools for medical diagnosis [36, 37, 38, 39].

With the widespread availability of near-infrared and infrared lasers, the working spectrum of optical tomography becomes broad and expands from the white visible light to infrared lights. A longer wavelength is found to result in enhanced contrast, higher resolution, and deeper penetration due to the reduction in scattering [40]. In other cases, the imaging system performs better at some specific wavelengths. For instance, the three primary absorbers in tissue at near-infrared wavelengths are water, oxygenated hemoglobin (HbO) and deoxygenated hemoglobin (Hb). Choosing a near-infrared spectrum between 700 nm and 900 nm will allow Hb to be seen as the water absorption is extremely low at these wavelengths but both HbO and Hb absorption are detectable [40, 41]. Overall, the imaging forming photons in optical tomography are in low frequency domains and will not ionize tissue cells. It offers a significant advantage over X-rays, Positron Emission Tomography (PET) and Single Photon Emission CT (SPECT) as nearly all optical tomography techniques are radiation free.

Beside radiation free, optical tomography also offers other advantages over competitive tomography techniques. Optical tomography techniques can potentially detect abnormal physiological activities earlier than Ultrasonography as the optical properties of the cells in dysplasia typically change earlier than the mechanical properties and density [36, 37, 38]. Most OT techniques have low infrastructure costs and high spatial resolution (sub-mm) [40], This is important in applications which can not afford Magnetic Resonance Imaging (MRI) or require good system portability. The comparison between OT and other imaging tomography methods are presented in the table below.

Table 1-2   ***Comparison between OT and other major imaging tomography methods [36, 40, 74, 75, 76, 77]***

Method	Spatial resolution	Temporal resolution	Side effect	Mechanism and comments
OT	10 µm at best	Some approaches are near real time	No	Based on ballistic photons or diffused photons + inversion algorithm. Low cost solution
Xray and CT	0.1 mm	X-ray 10 ms CT: 0.5 s	Radiation	Relies on contrast from electron density
SPECT and PET	3 -10 mm	5 - 10 mins	Strong radiation	Relies on radiolabel
MRI	0.1 mm	100 ms	No	Relies on proton density and mechanical properties of the tissue
Ultrasonic	2-3 mm	40 ms	No	Based on differences in acoustic impedance

The biggest challenge for OT is that instead of penetrating the tissue with predominantly straight transmission as X-rays, the majority of photons are highly scattered and the Signal to Noise Ratio (SNR) is poor. Optical tomography modalities could be categorized based on how to solve this issue. Diffuse Optical Tomography (DOT) represents one type of solution that works on re-constructing the image based on the propagation model of light diffusion. The other methods, like Time-Domain (TD) tomography, Optical Coherence Tomography (OCT) and Confocal Microscopy (CM), focus on separate ballistic or quasi-ballistic photons from scattered ones first and then build the image based on them.

DOT (Fig. 1-5(a)) is the most representative optical tomography modality in the first group. With DOT, tissues are illuminated with light sources and an array of detectors are employed to measure all the lights exiting the tissue. A diffusive light propagation model inside the tissue has been developed and parameterized in terms of the scattering and absorption as a function of position based on the result matrix between the light sources and the detector array. Once the photon distribution is mapped, the scattering/absorption parameters of the tissue could be recovered via the inversing process according to the light propagation model. Both time-domain (light pulse source)

and frequency domain (modulated light source) analyses could be implemented to facilitate the reconstruction of the image [40, 42, 43].

In stead of working with the sophisticated light propagation model as DOT, other OT approaches focus on how to separate ballistic photons out of scattered ones experimentally. Time-Domain (TD) tomography [23] introduces a time shutter with a pulse light source. Photons scattered will reach the shutter later than the ballistic ones due to longer optical paths (Fig. 1-5(b)). Since only a small portion of photons emitted by the light source is captured, the signal in TD is weak and the data acquisition takes longer than the modalities working in Continuum Wave (CW) mode [7, 40]. Optical Coherence Tomography (OCT) [40, 45, 46] distinguishes non-scattered and scattered photons based on the differences between the length of their optical paths as well (Fig. 1-5(c)). Similar to ultrasonic imaging which collects sound wave reflected when encountering an interface where the impedance changes, OCT works with photons reflected at interrogated tissue interfaces. Ballistic photons will be coherent with photons in the reference beam. However, the optical path difference between the scattered photons and the reference will be too large to maintain the coherence. The resolution of OCT is much higher than ultrasonic imaging. On the other side, it cannot penetrate as far. With OCT, images can be produced in real time with a micrometer-scale resolution at imaging depths of 1–2 mm [40, 47]. Confocal Microscopy (CM) identifies the ballistic photons by using a spatial aperture to remove anything out of the depth of the focus. As the result, it only takes the fluorescent ballistic photons excited by the illumination lights and emitted from the interested volume (Fig. 1-5(d)). The depth range of CM is around 200-300 μm, and it can non-invasively image tissues *in vivo*, especially for the skin, eyes and gastrointestinal tract [40]. Like a conventional optical microscope, the resolution of a confocal microscope is limited by diffraction of light. For the optical setup of most commercially available CMs, this limit is 200 ~ 500 μm [62].
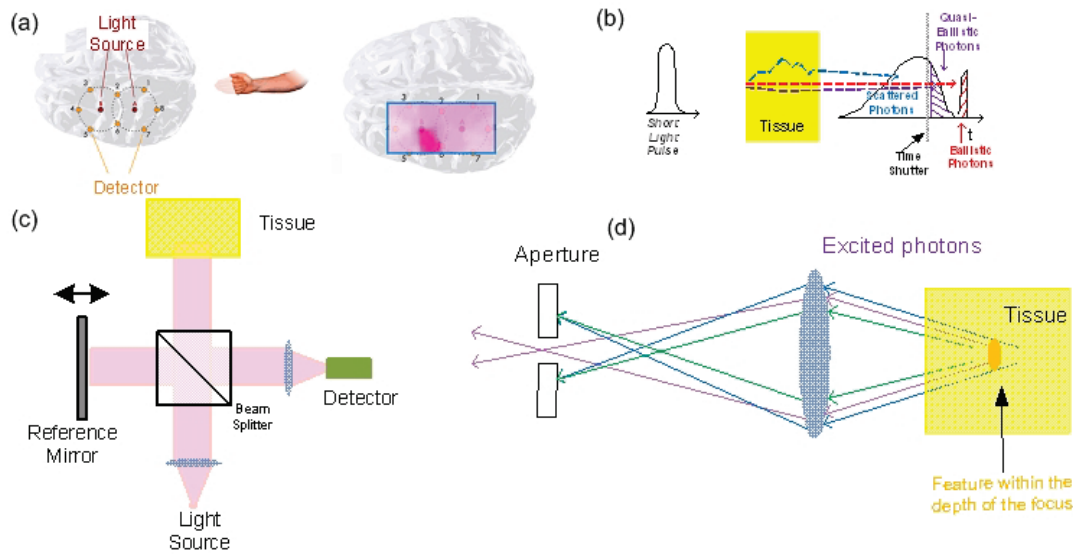
Fig. 1-5 Sample optical tomography modalities: (a) a DOT application: the light distribution in the brain is mapped while the patient is performing 4 finger flexion-extension movements. The information collected could generate the brain image and help to study cerebral hermodynamics. Figure adapted from reference [39]; (b) a timer shutter is implemented to filter out scattered photons in TD; (c) Scattered photons are not coherent with the reference beam due to light path difference in OCT; (d) Excited photons which are out of the depth of the focus or not ballistic transmitted will be rejected by the spatial aperture in CM.

Optical tomography modalities typically either operate in transillumination mode or epi (reflectance) -illumination mode. The illumination optics and the detection optics are placed at different sides of the sample in transillumination setup, but at the same side in epi-illumination setup. Reflectance systems have become widely used largely due to the impracticalities related to transillumination setups in non-invasive *in vivo* optical imaging, which arise from the strong attenuation of light through thick tissue. Chapter 7 of this thesis will focus on the implementation of angular domain spectroscopic imaging with a reflectance setup. However, as most scattering in biological tissues is forward oriented and a relatively small number of photons are back-scattered, reflectance setups suffer from low signal-to-noise ratio (SNR), resulting in weaker signals than transillumination setups [48, 49, 50]. OCT, CM, Two-photon Excitation Microscopy and Speckle Imaging are common optical tomography modalities operating in the reflectance mode. They rely on contrast mechanisms such as coherent

scatter, light emission from genetically engineered sources, or exogenously administered agents to improve SNR. They can achieve high spatial resolution, but the depth penetration remains limited (within 1-2 mm of the surface) [40, 42, 43, 45, 46, 51, 52, 53, 54, 55]. Therefore, considerable efforts have been directed at developing reflectance methods that provide better depth penetration and utilize endogenous contrast mechanisms. For example, Photoacoustic Microscopy (PAM) provides images of biological tissues via the capture of the ultrasonic emission generated by optically absorbing structures in response to high energy laser pulses. Optical absorption of hemoglobin and melanin represents the primary contrast mechanism in PAM images of unstained tissues. PAM provides good depth penetration (up to 3 mm) with lateral resolution approaching OCT and CM, however, the setup can be complex [56]. As described above, DOT is also a reflectance optical tomography modality and it works with both scattering and absorption contrast mechanisms as well as exogenous agents. DOT provides excellent depth penetration and a large field of view. However, DOT has limited spatial resolution, which is at best on the order of several millimetres and degrades with depth [40, 43].

1.3.2.   ADI and ADSI concepts

Angular domain imaging (ADI) is a method to extract optical contrast for features embedded in a turbid medium via filtering photons according to their propagating directions. It also falls into the category of ballistic imaging. Extensive investigation has been conducted with different angular filter methods including collimator, spatial filter, lens and pinhole in the early stage of ADI development [57, 58, 59, 60]. In addition, angular filter array (AFA) based ADI was first introduced in the year of 2000 by Tank and Chapman [61]. AFA is a line silicon micro-machined optical collimator consisting of a series of parallel micro-channels. AFA is capable of selecting image-bearing photons that travel within the acceptance angle of AFA channels and absorbing image-destroying photons that travel beyond the acceptance angle (Fig. 1-6). By scanning an AFA over the sample, the intensity of the light along a certain direction is acquired as a function of location, representing the change in both scattering and absorption properties of the objects along the scan direction. Subsequently, a two dimensional image could be constructed from the obtained one dimensional line images. AFA is proposed to provide

23

sub-millimetre resolution, small acceptance angle, and broad operating spectral range with a simple and compact system. AFA based ADI prevailed recently as none of other ADI approaches can offer these features at the same time [10].

The filtering function of AFA is independent of photon frequency from visible to near-infrared range, which allows researchers to take images at multiple wavelengths for spectroscopic analysis and leads to the invention of Angular Domain Spectroscopic Imaging (ADSI). It also enables potential applications in fluorescence detection. The other appealing feature which ADI offers is the removal of the requirement for coherent light sources (as OCT) or ultra-fast pulse lasers. Therefore, low cost lamp or LEDs can be used and the system infrastructure is much simplified. It enables the applications in portable imaging system and low cost clinical screening system [10]. Please check the table below in regards to the ADI value proposition versus other competitive OT modalities.

Table 1-3   ***Comparison between ADI and other major OT modalities [10, 40, 50, 62]***

Method	Spatial Resolution	Depth	System	Comments
TD	1 mm	1 cm	Need expensive ultra-fast laser and detector	Long scan time, poor temporal solution
OCT	10 - 20 µm or better	1-2 mm (retina)	Complex, it is a interferometry method. Need coherent light source	Limited penetration, successful in ophthalmology
DOT	1 mm ~ 1 cm	1.5 cm	Multiple sources and detectors.	Need complex algorithms
PAM	0.2 mm ~ 0.5 mm	1 mm - 1 cm	Need high power pulse laser	High cost
CM	0.5 µm	100 - 200 µm	Need spatial filter. Need fluorescein	Limited penetration, high spatial resolution approaching diffraction limit
ADI	0.2 mm	3 mm - 1cm	Any light source, simple setup	Low cost.

1.3.3. *Angular Filter Array (AFA) design*

As a collimator array, the key feature of AFA is the acceptance angle which is defined in Fig. 1-6(c). With the first order of approximation, the ideal AFA channel restricts photons to a maximum angle of θ

$$\theta \approx \tan \theta = \frac{w}{l}, \tag{1.42}$$

where *w* represents the width, *l* represents the length and *w/l* is also named as the aspect ratio of the AFA channel. Equation (1.42) remains accurate as long as the requirement of paraxial approximation is satisfied. Please note that *w* shall be replaced by *h* (height) while the calculation is performed along the height direction. In practical, the acceptance angle of AFA is typically less than 0.5°. Photons propagating beyond this angle are absorbed by the channel walls after a couple of reflectance events. Photon traps could help to suppress them faster and reduce the noise [10].

Typical AFA channels are ~ 10 mm in length, 50 ~ 80 μm in width and 60 ~ 80 μm in height. The wall between two AFA channels will be projected as a dark strip in the camera and it shall remain thin to improve the spatial resolution. However, a thicker channel wall can keep the light outputs of two neighboring channels from mixing with each other. The actual channel wall thickness in the latest devices is compromised to 10~20 μm to allow a propagating distance of 1 - 3 mm without any cross-talk and achieving sub-millimetre spatial resolution. The overall AFA device is 20~ 25 cm in width and has around 200 channels. The spatial period of AFA is the total width of the channel and channel wall. The typical value is 100 ~ 120 μm (Fig. 1-6). AFA outputs collimated light beams, which lowers the numerical aperture requirements of the detection optics. In some cases, AFA could be directly coupled to a line camera or spectrometer without additional lenses [73].
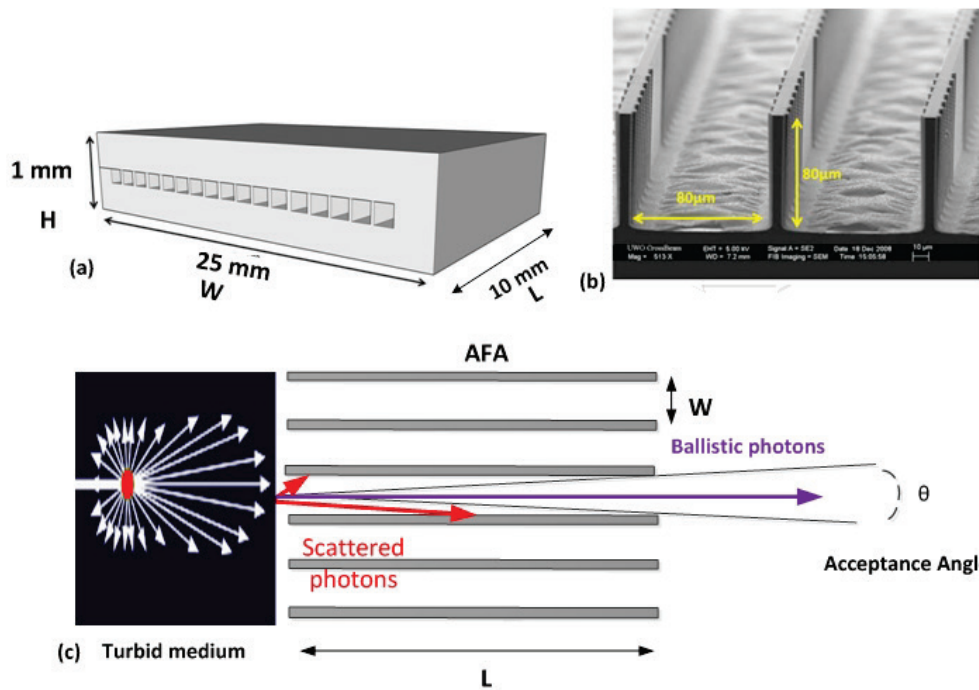
Fig. 1-6 (a) A sample AFA. Figure adapted from reference [44], (b) AFA channels. Figure adapted from reference [70] (c) AFA acceptance angle.

1.3.4. AFA fabrication

AFAs were typically fabricated from low cost silicon wafers. The first step was to grow a silicon dioxide layer of 500 ~ 800 nm as a masking layer via wet oxidation process. The next step was to pattern the silicon dioxide layer using a regular lithography process. After the development, the pattern in the photoresist could be transferred to the underneath silicon dioxide layer via a wet etching process. Buffered HF was used as the etchant. Subsequently, the photoresist layer was removed by the acetone. The next step was to etch the AFA channel in the silicon wafer with the patterned silicon dioxide layer as the mask. Conventionally, AFA channel was etched using wet isotropic etchant of silicon. However, the etching depth was limited to half of the width when the channel width was fixed. In this thesis project, all AFAs employed were etched by Deep Reactive-Ion Etching (DRIE), which permitted deep channels (*w/h* ~ 1). In addition, DRIE permitted the photo trap structure inside the channel as shown in Ref [69]

In the end, the masking silicon dioxide is striped by the buffed HF and the channel is enclosed by a polished the silicon wafer piece which has the same dimension of the substrate. Then AFA will be loaded into a cradle which clamps the cover piece and the substrate together. The cradle can be mounted into a 6 degree-of-freedom optical mounting device for testing. The overall fabrication process has been detailed in Ref [10] and [61].

1.3.5.   ADI systems

AFA is essentially a single dimensional device with limited field of view, and a scanning procedure is needed to create a two dimensional shadowgram of the test object. The vertical and horizontal spatial resolutions were limited by the scanning steps, detection optics, AFA channel aperture and the absorption and scattering properties of the medium. It is also affected by the system setup. Transillumination is the most developed ADI system configuration as shown in Fig. 1-7(a). In this case, the illumination is performed either by a laser or Quartz Tungsten Halogen (QTH) lamp. Then it passes the optical filter and is projected to the sample as a collimated beam. AFA is handled by 6 degree-of-freedom sample holders and scanned across the sample. AFA output beam will either be directly coupled into the detector or collected by the detection optics. Besides the transillumination setup, reflectance illumination has also been developed. Ref [50] presents a preliminary trial with reflectance illumination setup. The incident beam is supplied from the side of the sample and the objects inside the turbid medium are illuminated by back-scattered photons (Fig. 1-7(b)). This illumination configuration is named as deep-illumination. One of the contributions of this thesis project is to advance the ADSI in the reflective image modality.
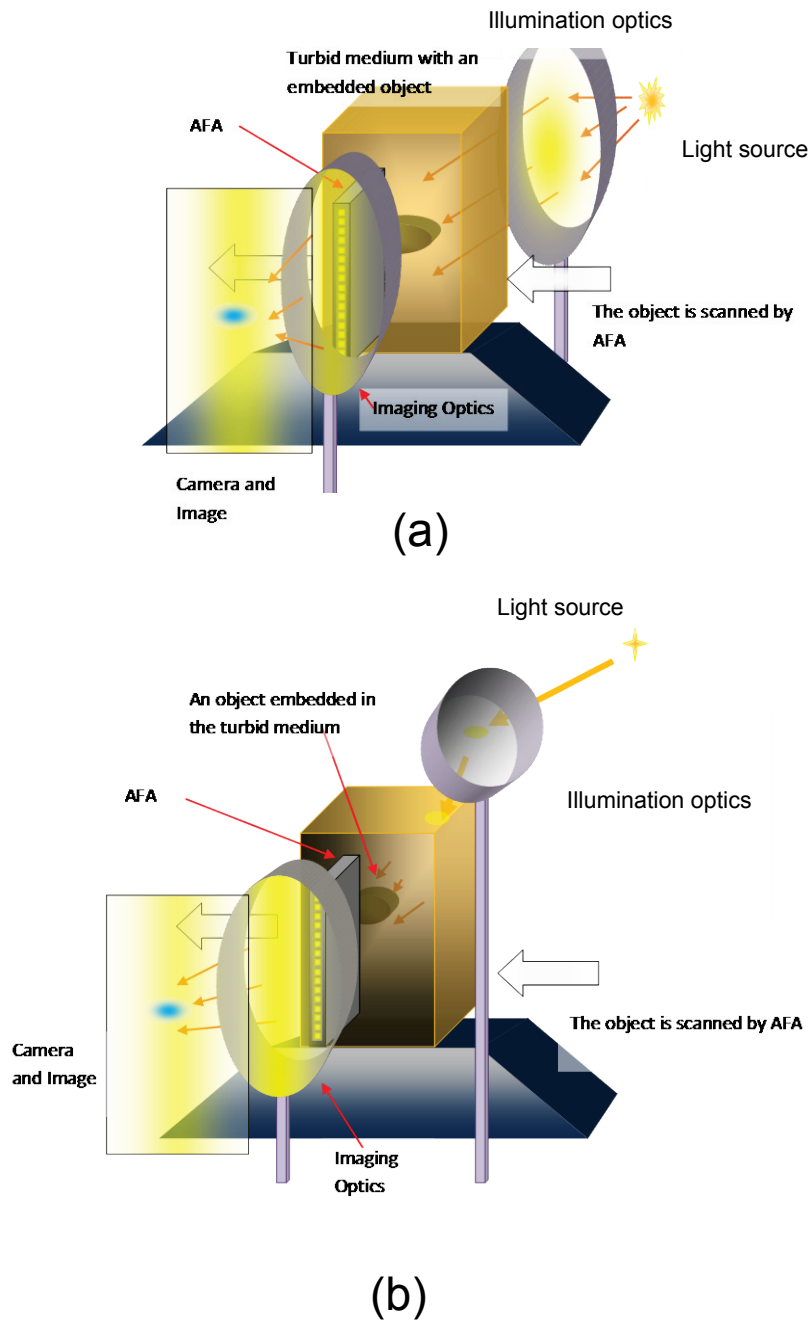
Fig. 1-7 (a) A transillumination ADI setup, (b) a deep-illumination ADI setup.

1.3.6. Current progress in ADI and ADSI

The early result for ADI based on Silicon Micromachined Collimator Array (SMCA) was published in 2000 [58]. It introduced the idea to use the AFA for imaging an object in

turbid medium in transillumination setup. A series of simulation work were performed after that and they validated the ADI concept. It confirmed that AFA channels would select photons traveling the shortest optical path, which were ballistic photons, and the channel acted as an optical filter to remove undesired scattered light without sacrificing the image resolution. Furthermore, they suggested that a narrower but longer channel could further enhance the detectability as long as they do not violate diffraction and Rayleigh range limitations [9, 62].

The next step of ADI development focused on the improvement in experiment setup and imaging results. The first attempt was to optimize the illumination source. Ref [64] and [65] explored the ideas to reduce the background noise by tuning the collimated illumination beam to match the AFA apertures better. Subsequently, Ref [67] introduced a series of contrast enhancement methods: using a polarized gating, capturing and subtracting scattered photons using a wedge prism, and using image processing algorithms to estimate the background noise and subtract it from the final results. The obtained results furthered the capabilities of ADI into the realm of highly scattering biological specimens (equivalent to 1% Intralipid^{TM} and beyond) up to 1 cm in thickness with the spatial resolution of sub-millimetres, leading towards the potential application of histological analysis of thick tissues. In parallel, further efforts have been spent on collaborating ADI with other imaging methods to improve the performance. Ref [69] demonstrated the new system combined ADI with time domain detection. Experimental results in tissue-mimicking phantoms explained that the collaboration between these two modalities further enhanced the imaging contrast without losing the spatial resolution. This paper also introduced the idea of microchannel wall reflection suppression with reflection-traps. This structure was widely used in the subsequent studies. Ref [68] and [72] demonstrated a system in conjunction with Optical Projection Tomography setup. It characterized the contrast and resolution of an ADI system at a multitude of locations within the imaging plane, then conducted the reconstructions of different targets using filtered back projection and iterative reconstruction algorithms. Similar to the Computered Tomography (CT) with X-ray imaging, this method provided three dimensional images for objects inside the turbid medium.

Besides the improvement of ADI systems, two important approaches were introduced to ADI imaging in the past a couple of years: multi- or hyper-spectral imaging

which led to ADSI, and fluorescent imaging, which led to Angular Domain Fluorescent Imaging (ADFI). Ref [66] presented a trial in multi-spectral ADI. The work provided confidence in the success of multispectral ADI for soft tissue up to 5 mm. Ref [73] extended the analysis from multi-spectral to hyper-spectral domain. It demonstrated the success in angular domain spectroscopic imaging for a 7-mm thick gel phantom with 0.5% Intralipid™ and 3-mm spherical absorptive targets doped with from 1 μM to 15 μM Indocyanine Green (ICG). Image-based spectral correlation analysis was developed using transmission spectra and their first order derivatives. The hyperspectral images obtained with ADSI were observed to depend on target concentration, target depth, and scattering level of the background medium. Besides ADSI, ref [68] and [70] described a novel macroscopic fluorescent imaging technique named ADFI. The method exploited the collimation detection capabilities of an angular filter array (AFA) for fluorescent imaging in both tissue-mimicking phantoms and murine model. They demonstrated that ADFI could achieve a large field of view with submillimeter spatial resolution at tissue depths up to 2 mm via mapping the fluorophores inside the tissue.

The recent progress in ADI and ADSI focused on applying the technology in real biological tissues. ADI was performed with small animal tissues, including a hairless mouse in ref [70]. Structural and morphometric data of vertebrae were collected using ADFI and correlated with data derived from volumetric X-ray CT and other conventional optical imaging systems. In ref [73], a SCCVII-tumor-bearing mice were sacrificed when tumor diameter reached 9-12 mm and each tumor with surrounding muscle was dissected in phosphate-buffered saline (PBS) solution. Hyper-spectral ADSI successfully detected these tumour tissues and identified their boundaries as well.

1.4. Thesis objectives and scopes

The first objective of this thesis was to design, fabricate and characterize Radial Angular Filter Arrays (RAFA). The aim was to develop RAFA from a concept to a full functioning device and use it to replace bulky and slower goniometer-based instruments or complicated interferometric systems to achieve low-cost, real-time and simplified optical scattering measurements. The RAFA based characterization systems would enable users to measure the angular spectroscopy of the object, which was important for

structural characterization, bio-sensing, and material identification. The successful development of RAFA would expand the applications of optical angular filtration devices beyond biomedical imaging. The proposed system would be validated via performing angular spectroscopy measurement and localization measurement of embedded targets with a series of homogenous and heterogeneous turbid media. In addition, the possibility of developing novel optical characterization system based on the combination of RAFA and other optical sensing device or filters would be discussed.

The second objective of this thesis was to advance the angular domain spectroscopic analysis in the biomedical imaging field by applying the multi-spectral analysis to reflectance ADI setups other than the conventional trans-illumination systems. This new technique allowed ADSI to perform non-invasive *in vivo* imaging while the sample was too thick to perform trans-illumination. A series of test system improvements and extensive imaging process techniques would be practised to enable Deep-Illumination Angular Domain Spectroscopic Imaging (DI-ADSI) to image tissue-mimicking phantoms. The obtained results would be evaluated against the value-proposition of DI-ADSI to assess whether DI-ADSI was a feasible alternative optical tomography modality in low-cost and fast *in-vivo* tissue scanning for superficial targets.

1.5. Research approach and chapter summary

This thesis contains the results of my research in angular spectroscopic characterization and imaging systems. The project started from designing a series of novel angular domain optical filters, called Radial Angular Filter Arrays (RAFAs). Those RAFAs were then fabricated and characterized under a collimated laser beam or a broadband QTH illumination beam for hyperspectral analysis. After that, applications of RAFA were explored with the recommended designs. Particularly, the experiments were performed with a series of tissue mimicking phantoms for potential applications in biomedical engineering. In order to extend the application of RAFA further, a novel angular spectroscopic measurement and sensing system was constructed based on RAFA and a Nano-Hole Array (NHA). The results obtained from the above angle-resolved spectroscopic analysis results motivated the author to advance the

spectroscopic analysis in angular domain imaging as well. Deep-illumination angular domain spectroscopic system was proposed and characterized in the end.

Chapter 2 describes the basic concept of RAFA. It reviews the available technologies up-to-date and explains the motivation of developing RAFA. A preliminary conceptual RAFA is introduced and its limitations are reported, including the signal loss in high angle channels and light leakage beyond the acceptance angle. A series of novel RAFA design concepts are proposed to overcome the shortcomings above, enhance the angular resolution, and reduce the complexity of the output coupling. 14 new RAFA designs are proposed and described in this chapter in detail. Extensive analyses and simulations are presented to illustrate the choices for design parameters in these 14 designs. In the end, the fabrication process of ACA is explained.

Chapter 3 focuses on the characterization of RAFA and the validation of proposed design concepts, including constant aspect ratio and constant acceptance angle, center channel blockage, channel wall coating, device achromaticity, and channel leakage and cross-talk minimization. The proposed characterization system consists of a broadband QTH source, collimation optics, trans-illuminated turbid samples, RAFA and a spectrometer. The test results will help to choose RAFA design from the proposed device list according to potential applications. Furthermore, a calibration process is established and it allows RAFA to be practised in trial applications at the end of the chapter. The results demonstrate that the RAFA could be useful for quantitative optical scattering analysis. It has the potential to be a practical tool for tissue optical properties measurement and angularly-resolved tissue imaging.

Chapter 4 validates the hypothesis that RAFA might be useful for examining optically absorbing features below the surface of a turbid medium via a depth mapping approach. RAFA consists of a radially-distributed series of micro-machined channels, which converge upon a focal point several millimetres away from the edge of the device. It is designed to measure the angular distribution of light emitted from an object located at the focal point and is capable of selecting ballistic and quasi-ballistic photons at specific angles out of strong background noise due to scattering. As a result, the depth of the object can be measured according to their relative position to the focal point. The chapter presents the results obtained with a focused laser beam, a series of Intralipid™

solutions (0.1 wt% to 1.0 wt%), a 0.5 mm diameter graphite rod (absorber), and a RAFA optically coupled to a line camera. By scanning the position of the rod and comparing the light scattering profiles obtained by the RAFA at each scanning step, the location and the depth of the rod were successfully identified.

Chapter 5 demonstrates RAFA's capability of collecting the angular distribution and the spectroscopic information of photons simultaneously and non-invasively, which allows angle-resolved spectroscopic measurement of a turbid medium. To explore the feasibility of using this device to characterize the optical abnormalities in human tissues, this chapter describes the performance of an angle-resolved RAFA-based spectroscopy system to detect absorption targets embedded within a tissue-mimicking phantom. The body of the phantom is made of 0.1% Intralipid™/agarose gel. The targets are spherical (1.5 mm in radius) and contain 10 μM Indocyanine Green (ICG). The illumination source is a broadband near infrared (NIR) collimated beam. Photons are angularly filtered by the RAFA and spectrally resolved by a pushbroom spectrometer. The experimental results confirm that RAFA preferentially filters photons that carry absorption and scattering information of the embedded targets.

In chapter 6, RAFAs are used to characterize the optical angular transmission properties of a nano-hole array (NHA) in an optically thick gold film. The focal point of the RAFA is coincident with the NHA during experiments. The RAFA demonstrates that it is capable of separating photons over a broad band according to the propagation direction. This technique characterizes the red or blue shift of surface plasmon resonances at different incident angles with only one camera exposure. The angular spectroscopic results are compared well with results from traditional microscopy and Finite Difference Time Domain (FDTD) simulations. RAFA-based angular spectroscopy of NHAs may improve performance for sensing applications that utilize NHAs or other surface plasmon resonance coupling structures.

Chapter 7 describes a novel reflectance optical imaging method, deep-illumination angular domain spectroscopic imaging (DI-ADSI). It is the further development of deep-illumination angular domain imaging (DI-ADI) whose key component is the Angular Filter Array (AFA). The DI-ADSI modality enables multi-spectral imaging of sub-surface features for samples that are too thick for trans-

illumination ADSI approaches. Here, we report on DI-ADSI system development and performance tests carried out with tissue-mimicking phantoms with multiple absorption features embedded below the surface. Multi-spectral images in the range of 666 nm to 888 nm clearly reveal the location of the sub-surface features for background scattering levels up to μ_s = 20 cm^{-1}. The shape of features is recovered for the sample whose background scattering level is μ_s = 6 cm^{-1} with image resolution < 1 mm. Furthermore, the attenuation spectra of each feature are successfully extracted for the purpose of identifying the composition.

Finally, in chapter 8, the summary of accomplishments is presented. The relations between each chapter are reviewed and emphasized. The improvement to the conventional techniques is demonstrated. The final conclusion is drawn based on the project objectives and the scope. Future work in this subject is also proposed.

2. Radial Angular Filter Array (RAFA) design and fabrication

2.1. Background and motivation

Optical instruments for angle-resolved scattering spectroscopy have been recognized as highly useful tools for characterization of surface topography, particle counting, and characterization of biological tissues at both macro and micro (cellular) levels [18, 19, 20, 21, 22, 23, 24, 25, 26, 27, 28, 80, 81, 82, 83, 84, 85]. At macro-scales, angle-resolved light-scattering distributions are conventionally measured by a goniometer, where either the sample or detector is mounted on a rotating arm [19, 20, 23, 21], or by a series of detectors placed at different angles [24, 19]. At micro-scales, instruments have employed approaches like low-coherence interferometry or scanning near-filed optical microscope [25, 26, 78, 79, 80, 81, 27] to acquire high resolution angle-resolved light distributions. However, these methods have been constrained by limited angle selection, limited angular range, lack of hyper-spectral measurement capability, long delays in data acquisition due to angular or wavelength scanning, and complex alignment arrangements [18, 19, 20, 21, 22, 23, 24, 25, 26, 27, 28, 80, 81, 82, 83, 84, 85].

Our objective is to develop a novel angled-resolved spectroscopy technique to overcome the limitations of the existing approaches as described above. The proposed method shall provide real-time angular and spectral distribution of light emitting from a point of interest. In this chapter, the design concept of a device named Radial Angular Filter Array (RAFA) will be presented. Preliminary evaluation results obtained from a turbid medium with various illumination patterns using a laser source (monochromatic), as well as a broadband source for hyperspectral measurements will be reviewed. Based on the results, a series of new designs will be calculated, simulated and discussed. The approach to fabricate the RAFA and the optimized designs will be presented in the end.

2.2. Preliminary conceptual RAFA

2.2.1. Device structure

A conceptual radial angular filter array (RAFA) was first introduced by our group (see [86]). It consisted of micro-machined channels in a silicon substrate and provided a means to measure the angular distribution of scattered light from a sample using a single exposure. Each RAFA channel collected photons emitted from a focal point at a specific angle and only photons traveling within a small acceptance angle relative to the channel direction could pass through. The focal point was located 3.9 mm away from the edge of the device and the micro-channels were positioned at steps of 2.5°. Most channels contained pre-bending, bending and post-bending sections as shown in Fig. 2-1. Angular filtration was primarily performed in the pre-bending sections. In this conceptual device, the pre-bending section was 5 mm in length and the acceptance angle was 1.29°. The cross-sectional size of the micro-channels was 80 μm x 80 μm. Bending and post-bending sections intended to facilitate the light coupling to the detection optics, otherwise it would be difficult for detection optics to collect light outputs at all angles due to the large divergence of the output beam directions. Bending was in arc format and the post bending sections were parallel to each other. By providing channels at a variety of angles, the RAFA collected photons propagating in different directions without scanning either the detector or the sample, enabling easy alignment and fast read-out.
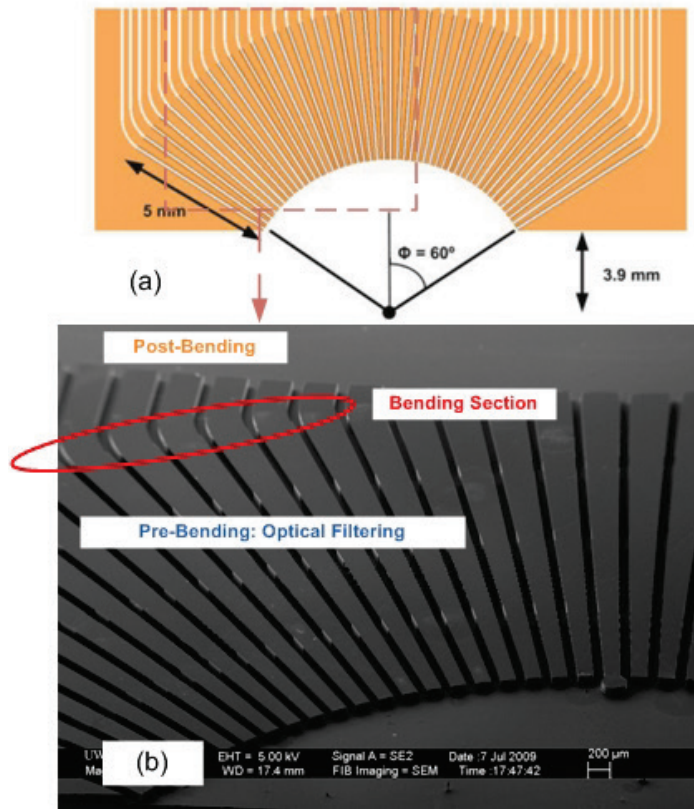
Fig. 2-1 (a) Dimension of the preliminary conceptual RAFA, (b) a zoom in SEM image of the RAFA. Figure adapted from reference [86].

2.2.2. Preliminary results and limitations

In our earlier work, RAFA was employed to measure the angular distribution of light from holographic diffusers (10° and 25°) and a series of Intralipid™ dilutions (0.1% and 0.2% through a 2 cm optical covette). The illumination source was a collimated He-Ne beam. The results demonstrated that the RAFA could discriminate the angular distribution of light emitted from a sample at the focal point of the device. Furthermore, two tests were performed with a collimated beam from a QTH lamp with a 25° diffuser or without the diffuser. Though obtained results were not sufficient to validate that the angular filtration of RAFA was independent of wavelength due to the weak signal at high angle channels and lack of quantitative analysis, these results were not against the assumption that RAFA was achromatic [86].

The work above indicated the potential success of the RAFA concept. However, this device had several drawbacks that limited the full characterization and the performance. The primary issue was the large crosstalk among channels, which was largely determined by the angular filtration capability of the device and the spatial separation of the output apertures. Inter-channel crosstalk was dependent on angular acceptance of each channel, which in turn defined the angle of photons exiting the device. Photons exiting in a narrow angular range were less likely to cross over into the detection path of neighboring channels. Increasing the separation of output apertures was likely to reduce inter-channel crosstalk as well, but at the expense of increasing the size of the device. The reflection of photons inside the channel also increased the inter-channel crosstalk as unwanted photons entering channels outside the acceptance angle tended to pass through, leading to higher inter-channel crosstalk and intensifying the background noise. This RAFA device had high inter-crosstalk as the channel shape, channel wall surface, and output apertures were not optimized. The second issue was the significant non-uniformity in light output between channels aligned with the axis of the device and channels at higher angles. Attenuation by higher angle channels was observed to be much more significant (by up to several magnitudes) than by channels near the central axis of the device. Even with a nearly isotropic source, a collimated He-Ne beam passing through a 2 cm cuvette filled with 0.2% Intralipid™, channel outputs at 30° or above were not visible or just barely detectable. It introduced a dynamic range challenge to the camera and subsequently, the noise in the measured intensity was higher for signals detected through the higher angle channels. The uniform angular sensitivity issue was largely related to the differences in channel shape and effective channel length at different angles.

2.3. RAFA design

2.3.1. Objectives and approach

The primary goal of this work was to develop the RAFA from a design concept into a working prototype capable of quantitative angular discrimination of light. Based on the issues discovered with the earlier RAFA device, our first objective was to perform a series of design improvements, including the design of features to lower inter-channel

crosstalk at the detector, and to reduce the variations of output signal at different angles to within a factor of 10 for an angularly uniform incident beam. Our second objective was to use appropriate ray-tracing models to evaluate the design improvement prior to the actual experiments. The last objective was to define a device list to be fabricated for device characterization according to the new design paradigms.

The first design target was to reduce the crosstalk between channels via new channel structures. Two angular filtration structures were proposed to minimize the background noise and achieve improved angular resolution. Second, two new output coupling structures were studied to reduce the non-uniformity in channel sensitivity across different angles, but preserve simple readout optics. The third design optimization target was to reduce the probability of detector saturation at channels close to the specular direction. With the new designs, we proposed to avoid the near specular direction measurements by blocking some of the center channels and concentrating on higher angle measurements. It was hypothesized that the blockage of the center channels could provide additional benefits related to the reduced signal loss as the length of the channels could be reduced. The fourth design optimization target was to improve the SNR via the enhancement of signal and the suppress of noise due to internal scattering. The improvement was achieved by introducing a reflective coating layer to bending and post-bending section of the channel and etching photon traps into the pre-bending section of the channel wall. In the end, minor design optimizations like focal length was discussed and a device list was generated based on the design optimization targets described above.

2.3.2. Channel structure design

Two different channel design paradigms, constant aspect ratio and constant acceptance angle (Fig. 2-2), were explored to improve the angular resolution of the RAFA and minimize cross talk. When using the term *acceptance angle*, by convention, we refer to the nominal acceptance angle of a channel measured in the plane of the device. With the constant aspect ratio paradigm (Fig. 2-3(a) and (c)), the channel width was kept constant within the pre-bending, bending and post-bending sections (where applicable). The acceptance angle of the channel was defined as the width of the channel at the output aperture in regards to the total length of the channel. When in use,

photons propagating with trajectories outside the acceptance angle were attenuated by the RAFA. With the constant acceptance angle paradigm (Fig. 2-3(b) and (d)), the cross-sectional area of each channel gradually increased from the input side to the output side. The design maintained the same acceptance angle with respect to the focal point, which was in the plane of the device. Constant acceptance angle designs allowed a smaller entrance aperture for each channel and the potential for higher angular resolution than constant aspect ratio designs. However, the cross talk between channels was expected to be greater as the output apertures in the constant acceptance angle designs were larger and the separation between channels was smaller.

Constant Aspect Ratio   **Constant Acceptance Angle**
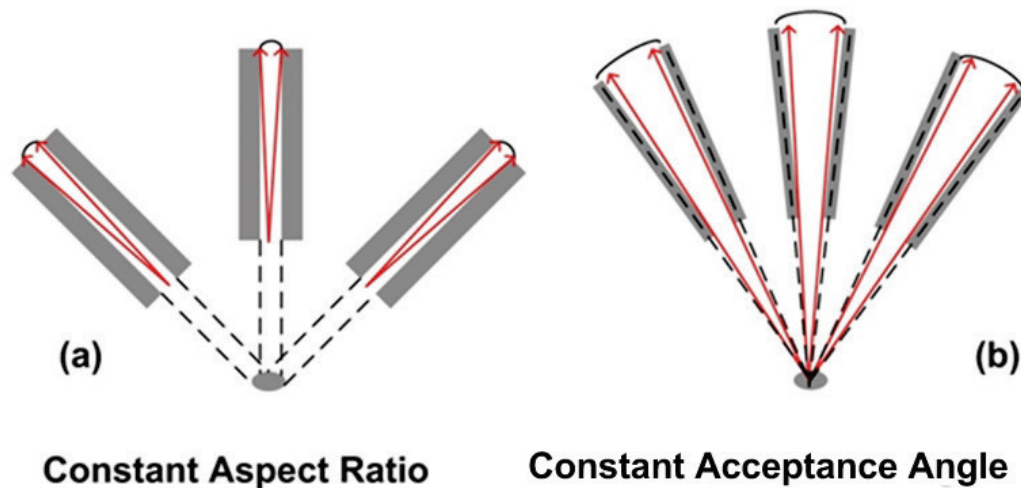
Fig. 2-2 (a) Design concept: constant Aspect Ratio; (b) design concept: constant acceptance angle.

The constant aspect ratio designs had a pre-bending section of 10 mm and the acceptance angle was 0.69º or 0.48º depending on the specific device. The corresponding width of the channel ranged from 80 μm to 120 μm, and the depth was 60 μm. Both width and height were significantly larger than the photon wavelength to minimize diffraction effects. In both designs, the aspect ratio was 83:1, resolution was 2.5º and the device width was 25 mm. The detection angle range of the device presented in Fig. 2-3(a) was [-35º, -7.5º] and [7.5º, 35º] while the range for the device shown in Fig. 2-3(c) was [-30º, 30º]. Fig. 2-3(b) and (d) show two designs with the constant acceptance angle of 1º. For these two designs, the device width was 25 mm, the channel walls were 100 nm in thickness and 60 μm in height, and the angular detection range was [-30º, -1º] and [1º, 30º].
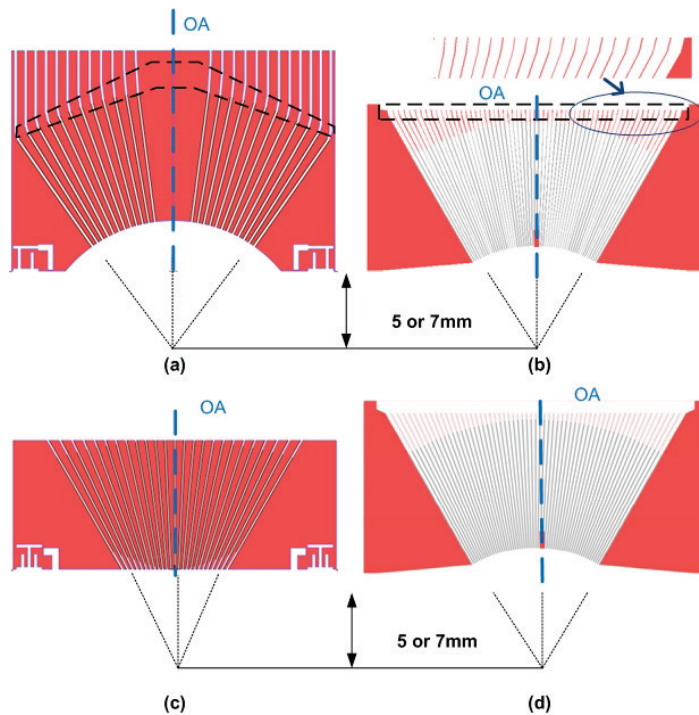
Fig. 2-3 Schematic diagrams of radial angular filter array designs showing (a) a constant aspect ratio design with micro-mirror bending structures; (b) a constant acceptance angle design with micro-mirror bending structures; (c) a constant aspect ratio design lacking bending structures; and (d) a constant acceptance angle design without bending structures. The areas highlighted by the dash lines in (a) and (b) represent the extent of the bending structures. The thick dashed line marked "OA" represents the optical axis for each design. Figure adapted from reference [103].

2.3.3. Output coupling design

Aside from the primary purpose of filtering photons at a series of radial directions (at certain angles relative to the material surface normal), the RAFA must also be designed to guide photons so that the photons could be efficiently coupled to a detection system with minimum loss and good uniformity across channels. To achieve these targets in practical designs, two RAFA output coupling approaches were explored.

The first method was related to a simple straight-through coupling scheme, where photons passed through an RAFA that lacked bending or post-bending structures. Device designs utilizing this straight-through scheme are illustrated in Fig. 2-3(c) and (d), where the lack of additional channel structures after angular filtration preserved the

propagation direction of photons. In this way, the transmission loss after the channels was expected to be minimal since photons within the acceptance angle of each channel would pass through the device without experiencing reflections. However, this method was expected to result in a wide range of RAFA photon exit trajectories (angles), which necessitated a lens to efficiently couple the RAFA to the detector. The inclusion of a lens increased system complexity and alignment difficulty due to the increased number of degrees of freedom.

The second RAFA output coupling method incorporated bending and post-bending structures to redirect the angularly filtered photons in a direction perpendicular to the output edge of the RAFA. In this method, photons from all channels exited the RAFA in the same direction, which was expected to improve and simplify RAFA-detector coupling efficiency and enable the use of an imaging spectrometer. As discovered with an early RAFA device (see Ref. [86]), the introduction of bending structure could potentially degrade the collimation and uniformity of the output beam. Significant channel loss (10 times more than the channels without bending) and large cross-talk were observed with the conceptual device. The multiple reflections happened in the bending curve was believed as the root cause and it was shown in Fig. 2-4(a) and (c). The solution was to change the circular bending into a mirror-like plane reflectance surface (Fig. 2-4(b) and (d) for detail structure). The implementation of this bending structure varied with different channel design paradigms. With constant aspect ratio designs, an aluminum-coated micro-mirror bending structure was incorporated into the RAFA as shown in Fig. 2-3(a) and Fig. 2-6(a-b). The direction of the front surface of the micro-mirror was selected to ensure that all photons within the acceptance angle of the channel were directed by a single reflection to the output of the RAFA. The length of each micro-mirror was selected to ensure that ballistic photons (i.e. with trajectories parallel to the channel) across the entire channel aperture experienced only one reflection. An advantage of this design was the uniform transmission efficiency across all channels. The second advantage of this design related to the improved collimation properties of the light exiting the RAFA in comparison to preliminary designs [86], which simplified optical coupling to the imaging spectrometer. Channels in constant acceptance angle designs were separated only by a thin wall, and the micro-mirrors were designed differently due to the lack of space between neighboring channels. For

example, for the design shown in Fig. 2-3(b), no bending structure was incorporated at low angles, but as the angle increased, an aluminum-coated bending structure was used and the length of the bending structure increased with the angle. However, due to the total length limitation of the device, the bending surface was not long enough to reflect all photons, except those travelling within the high angle channels. The design preserved the high angular resolution of the device and minimized the length of the post-bending sections to reduce the signal loss. However, the design introduced non-uniformity in signal transmission efficiency across the output of the RAFA.
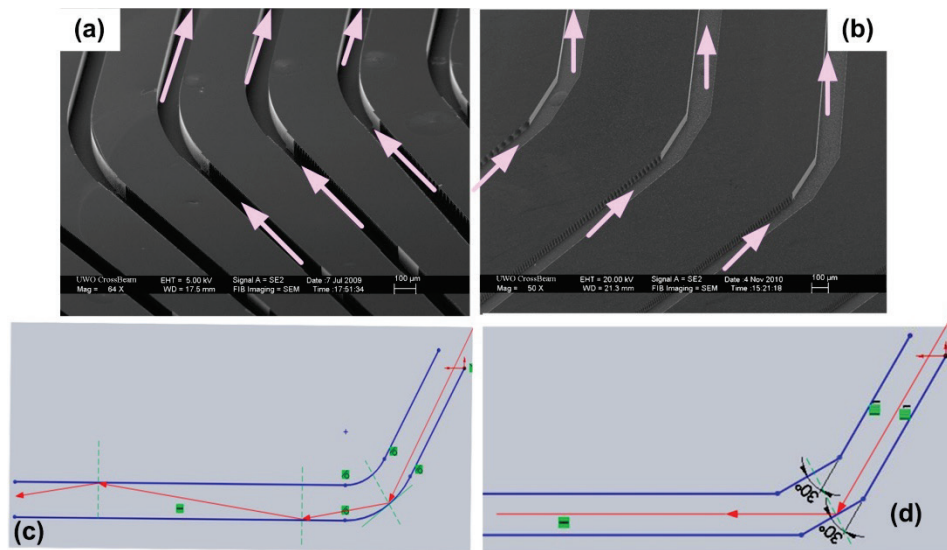
Fig. 2-4 (a) A SEM picture of the circular bending structure in the preliminary prototype; (b) a SEM picture of the mirror bending structure in one of the proposed new designs; (c) a diagram demonstrates that a photon will experience multiple reflections after a circular bending over 30º; (d) in the proposed design, a selected photon is supposed to be only reflected once before it is collected by the detector. Figure adapted from reference [89].

2.3.4. Center channel blockage

For samples where the scattering is weak or is forwarded-directed as in biological tissues, a large proportion of photons are expected to travel along or close to the specular direction (optical axis) of the RAFA. Measured BRDF for a reflected smooth sample are likely to vary by as much as 15 orders of magnitude from the specular direction to side directions[6]. In addition, channels around the specular direction

provided minimal attenuation due to the lack of bending sections and shorter channel lengths as if these channels were bent, the total length of the device would increase dramatically and the post-bending sections in high angle channels would be extended unnecessarily (Fig. 2-5). According to the measurement results with the earlier RAFA device, signals detected from center channels could be a few orders of magnitude higher than signals detected from the output of channels representing higher angles [86]. Both high angle and center channels carried the post-scattering angular distribution information; however, signals from center channels were corrupted by a high proportion of ballistic and quasi-ballistic photons. The center channels tended to saturate the camera easily necessitating short exposures, which resulted in under exposure of pixels representative of high angle channels, (Fig. 2-3(a) and (b)). For these reasons, the structure in the conceptual RAFA tended to exaggerate the non-uniformity in signal strength. To overcome these deficiencies, channels within ± 5° of the optical axis were blocked in constant aspect ratio designs, while channels within ± 1° of the optical axis were blocked in constant acceptance angle designs.

(a)   **(b)**

Bending in a high   Bending in a
angle channel   central channel
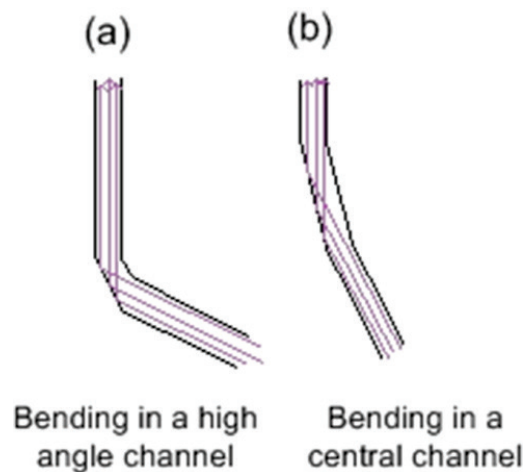
Fig. 2-5 The length of the bending plane in a central channel is longer than that in a side (high angle) change (a) side channel; (b) central channel

2.3.5. Improvement in channel wall

From previous work, it was confirmed that light entering the channels beyond the acceptance angle could act as a source of background bias at the channel output due to intra-channel reflections [86]. Therefore, in all RAFA devices, the channel walls in the pre-bending section were patterned with photon trapping vertical ridges (width of 5 μm, i.e. at least five times the wavelength of photons in the near infrared (NIR)) at a spatial period of 5~20 μm to effectively trap photons with trajectories beyond the acceptance angle (Fig. 2-6(c-d)).

On the other side, the primary goal in bending and post-bending section is to couple the photons propagating along the channel direction to the detectors. Instead of an absorptive channel wall, the channel surface shall have high reflectance. An aluminum coating layer is proposed as shown in Fig. 2-6(a). As a common practice, the roughness of the Aluminum coating needed to be less than 1/4 of the wavelength to minimize the scattering. In the ideal case, the light output at different channels would still maintain the collimation and it could be easily fit into any detector optics.
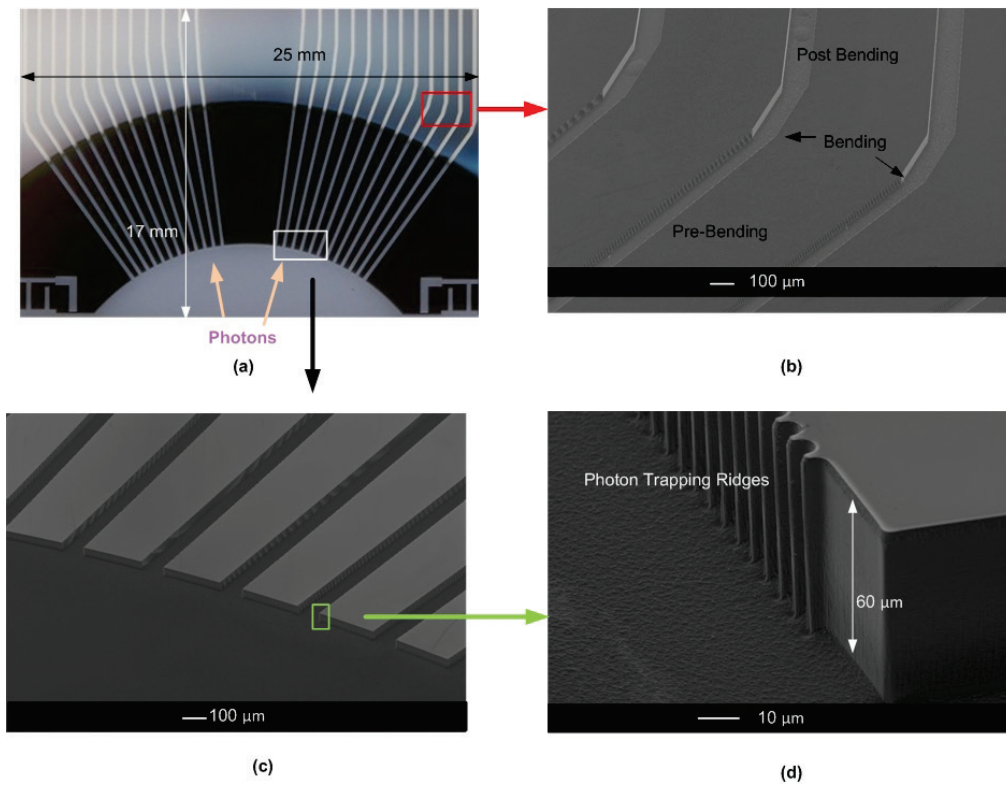
45

2.3.6.   Focal length

Both constant aspect ratio and constant acceptance angle designs are designed to exclusively collect photons scattered from the focal point and towards specific directions while the sample is an isotropic scattering medium. In this case, photons that are not emitted from the focal point will be corrected based on the symmetric analysis of RAFA output around its optical axis. In most designs, a semi-circular shape was introduced at the edge close to the focal point to prevent the channels from overlapping with each other.

The focal point was designed to be either 5 mm or 7 mm away from the edge of the device. The devices with 7 mm focal length were able to provide deeper penetration inside a turbid medium. However, the background noise might be higher in this case because photons needed to travel over a longer distance before they entered the channel and some extra noise was expected to be picked up.

2.3.7.   Ray tracing validation

A ray-tracing model was simulated (Zemax ver. EE, Radiant Zemax LLC., WA) to validate design optimizations in the bending structure related to reduction of inter-channel cross talk. The simulated rectangular channel was bent by 30° in the model, and it had the same cross-section, pre-bending and post-bending sections as the 30° channel in Fig. 2-3(a). A collimated broadband beam (650-950 nm, uniform spectrum, total power of 1 mW) was projected into the channel. The detector was placed perpendicular to the channel direction 1 mm away from the output aperture. The channel wall was coated with aluminum, and the reflectivity of the coating layer was 90%. For photons reflected, the probability of scattering due to surface roughness was 10%. The

expansion of the output beam indicated the severity of the cross talk between neighboring channels.

For the conceptual device (see Ref. [86]), cross talk was evident at the output of adjacent channels even after 1 mm of propagation in the air. The curved bending structure in the device introduced output beam divergence that introduced inter-channel cross talk and degraded the angular resolution of the device significantly. With curved bending structures, the simulation results revealed that photons would be reflected multiple times in the channel leading to a significant loss in collimation quality at the output of the RAFA (Fig. 2-7(a)). For channels bent by 30°, only 14% of the incident power was delivered to the detector and the size of the output beam expanded over 3 times at the detector location (Fig. 2-7(c)). For the new reflective bending structure (Fig. 2-7(b)), the ray-tracing simulation showed that 47% of the incident power was preserved at the channel output, and the collimation of the output beam was dramatically improved. Furthermore, the size of the beam was still roughly the same as the exit aperture at the detector (Fig. 2-7(d)). Therefore, ray tracing simulation confirmed that the design change increased channel transmission efficiency significantly with a sizable reduction in crosstalk.

2.3.8.   *Proposed devices*

14 different devices were proposed and fabricated in this thesis project as shown in Table 2-1. Among these 14 RAFAs, the following design parameters were changed: focal length (5 mm or 7 mm), output coupling method (bending or no bending), constant aspect ratio or constant acceptance angle, high aspect ratio (120:1) or low aspect ratio (83:1), center channel blockage or not. Each RAFA was described in detail in Table 2-2.

Table 2-1   ***Proposed RAFA design matrix***

		Focal Length: 7mm		Focal Length: 5mm	
		bending	no bending	bending	no bending
Constant Aspect	120	Design 1	Design 2	Design 3	Design 4
	83	Design 5	Design 6	Design 7	Design 8
Constant Acceptance Angle (Aspect Ratio ~ 100)	center blocking	Design 9	Design 10		Design 11
	no center blocking	Design 12	Design 13		Design 14
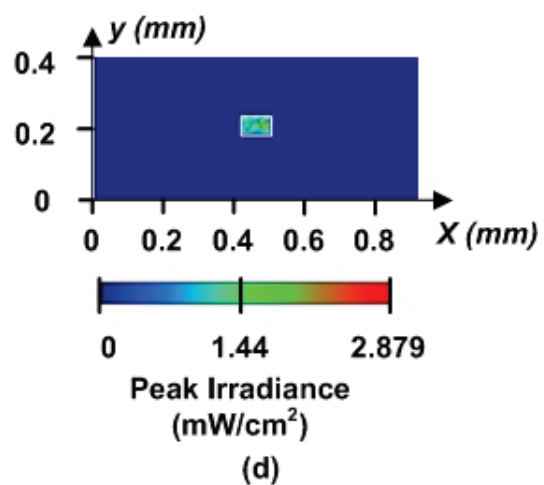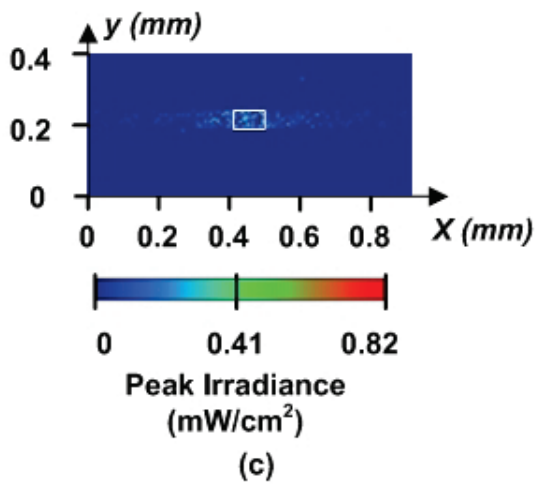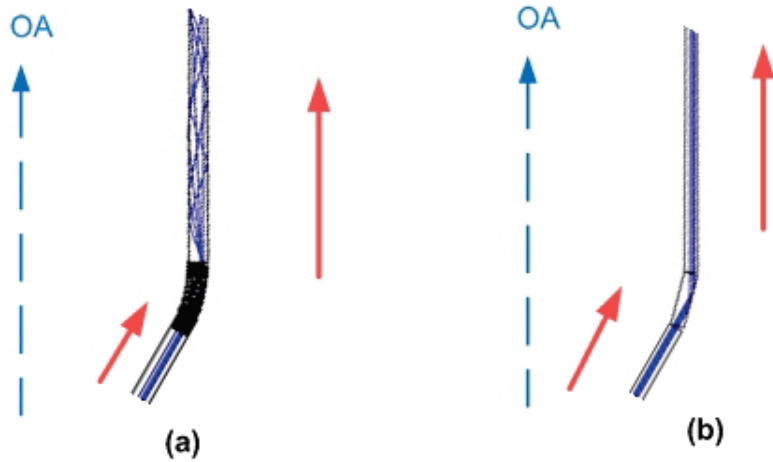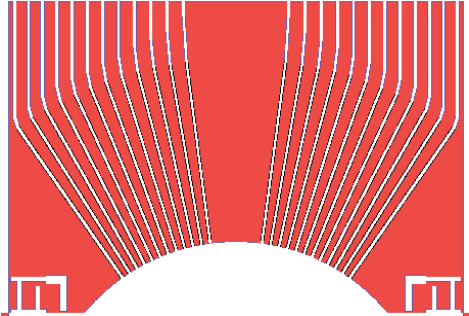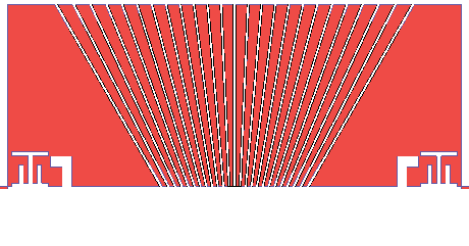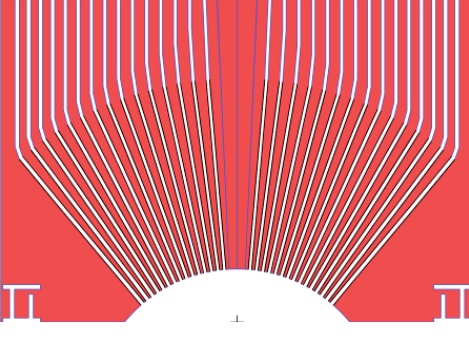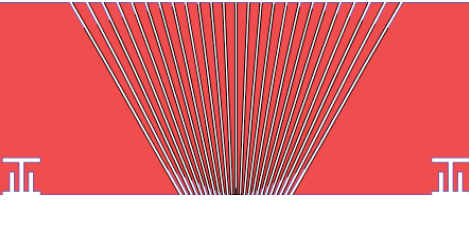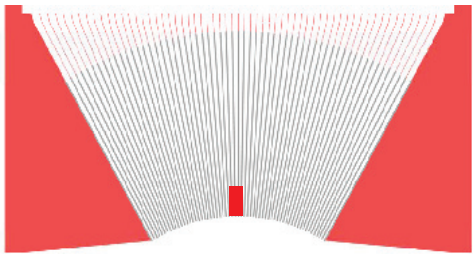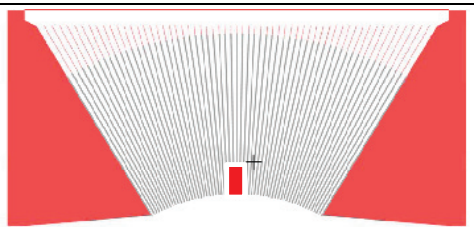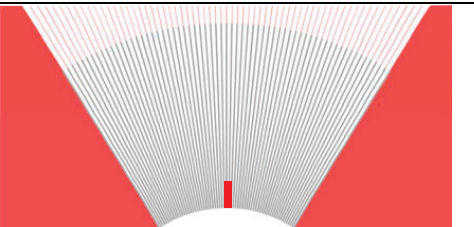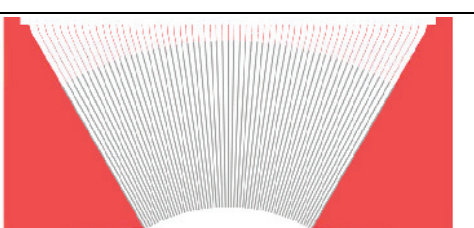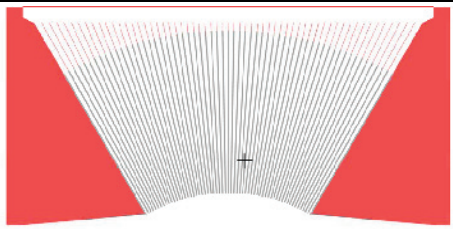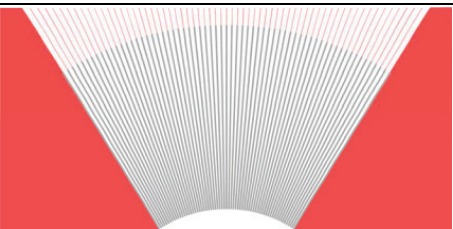
Fig. 2-7 (a) Ray-tracing model for circular bending (30°). (b) Ray-tracing model for a discrete mirrored bending region (30°). Black lines represent the shape of the channel; blue lines are rays and red arrows indicate the direction of photon propagation. Optical axis is marked as a dashed arrow. Cross-sectional output of the RAFA output aperture viewed 1 mm away from the output for the device with circular bending (c), or discrete mirrored bending (d). In panels (c) and (d), the white rectangular demarcates the size of the output channel aperture. Figure adapted from reference [103].

Table 2-2   Proposed RAFA list

#	Diagram	Description
1		Constant Aspect Ratio at 120:1 Focal Point: 7mm away from the edge Bending: mirror bending Detection Angle: $-35^0 \sim -5^0$ and $5^0 \sim 35^0$ Resolution 2.5^0 Device Width: 25 mm Device Length: 17 mm
2		Constant Aspect Ratio at 120:1 Focal Point: 7mm away from the edge Bending: No Bending, Detection Angle: $-30^0 \sim 30^0$ Resolution 2.5^0 Device Width: 25 mm Device Length: 10 mm
3		Constant Aspect Ratio at 120:1 Focal Point: 5mm away from the edge Bending: mirror bending Detection Angle: $-40^0 \sim -5^0$ and $5^0 \sim 35^0$ Resolution 2.5^0 Device Width: 25 mm Device Length: 17 mm
4		Constant Aspect Ratio at 120:1 Focal Point: 5mm away from the edge Bending: No Bending, Detection Angle: $-30^0 \sim 30^0$ Resolution 2.5^0 Device Width: 25 mm Device Length: 10 mm

5		Constant Aspect Ratio at 83:1 Focal Point: 7mm away from the edge Bending: mirror bending Detection Angle: $-35^\circ \sim -7.5^\circ$ and $7.5^\circ \sim 35^\circ$ Resolution 2.5° Device Width: 25 mm Device Length: 17 mm
6.		Constant Aspect Ratio at 83:1 Focal Point: 7mm away from the edge Bending: No Bending, Detection Angle: $-30^\circ \sim 30^\circ$ Resolution 2.5° Device Width: 25 mm Device Length: 10 mm
7.		Constant Aspect Ratio at 83:1 Focal Point: 5mm away from the edge Bending: mirror bending Detection Angle: $-40^\circ \sim -5^\circ$ and $5^\circ \sim 35^\circ$ Resolution 2.5° Device Width: 25 mm Device Length: 17 mm
8		Constant Aspect Ratio at 83:1 Focal Point: 5mm away from the edge Bending: No Bending, Detection Angle: $-30^\circ \sim 30^\circ$ Resolution 2.5° Device Width: 25 mm Device Length: 10 mm

9		Constant Channel Wall Thickness: 100µm Focal Point: 7mm away from the edge Bending: No bending within +/- 8°. Bending was introduced since 8°and the portion of the channel which is bent is gradually increased and the full channel is bent at the +/-30° Blocking: Center two channels are blocked. Detection Angle: $-30°\sim -2°$ and $2°\sim 30°$ Resolution $1°$ Device Width: 25 mm Device Length: 13 mm
10		Constant Channel Wall Thickness: 100µm Focal Point: 7mm away from the edge Bending: No bending Blocking: Center two channels are blocked. Detection Angle: $-30°\sim -2°$ and $2°\sim 30°$ Resolution $1°$ Device Width: 25 mm Device Length: 13 mm
11		Constant Channel Wall Thickness: 100µm Focal Point: 5mm away from the edge Bending: No bending Blocking: Center two channels are blocked. Detection Angle: $-30°\sim -2°$ and $2°\sim 30°$ Resolution $1°$ Device Width: 25 mm Device Length: 13 mm
12		Constant Channel Wall Thickness: 100µm Focal Point: 7mm away from the edge Bending: No bending within +/- 8°. Bending was introduced since 8°and the portion of the channel which is bent is gradually increased and the full channel is bent at the +/-30° Blocking: No Blocking Detection Angle: $-30°\sim -2°$ and $2°\sim 30°$ Resolution $1°$ Device Width: 25 mm Device Length: 13 mm

13		Constant Channel Wall Thickness: 100μm Focal Point: 7mm away from the edge Bending: No bending Blocking: No blocking Detection Angle: $-30^{\circ} \sim -2^{\circ}$ and $2^{\circ} \sim 30^{\circ}$ Resolution 1° Device Width: 25 mm Device Length: 13 mm
14		Constant Channel Wall Thickness: 100μm Focal Point: 5mm away from the edge Bending: No bending Blocking: No Blocking Detection Angle: $-30^{\circ} \sim -2^{\circ}$ and $2^{\circ} \sim 30^{\circ}$ Resolution 1° Device Width: 25 mm Device Length: 13 mm

2.4. Fabrication process

2.4.1.   Mask design

The first step of RAFA fabrication was to design four chrome masks to pattern the silicon dioxide mask layer. The masks were designed by L-Edit Pro V11.1 (Tanner EDA) and fabricated in University of Alberta. The main improvement from the mask used for the conceptual device was to leave a blank area at the channel openings and enclose this area with a boundary pattern as shown in Fig. 2-8. Without the boundary features, the blank area would be covered with Chrome and the dicing process would be extremely difficult.
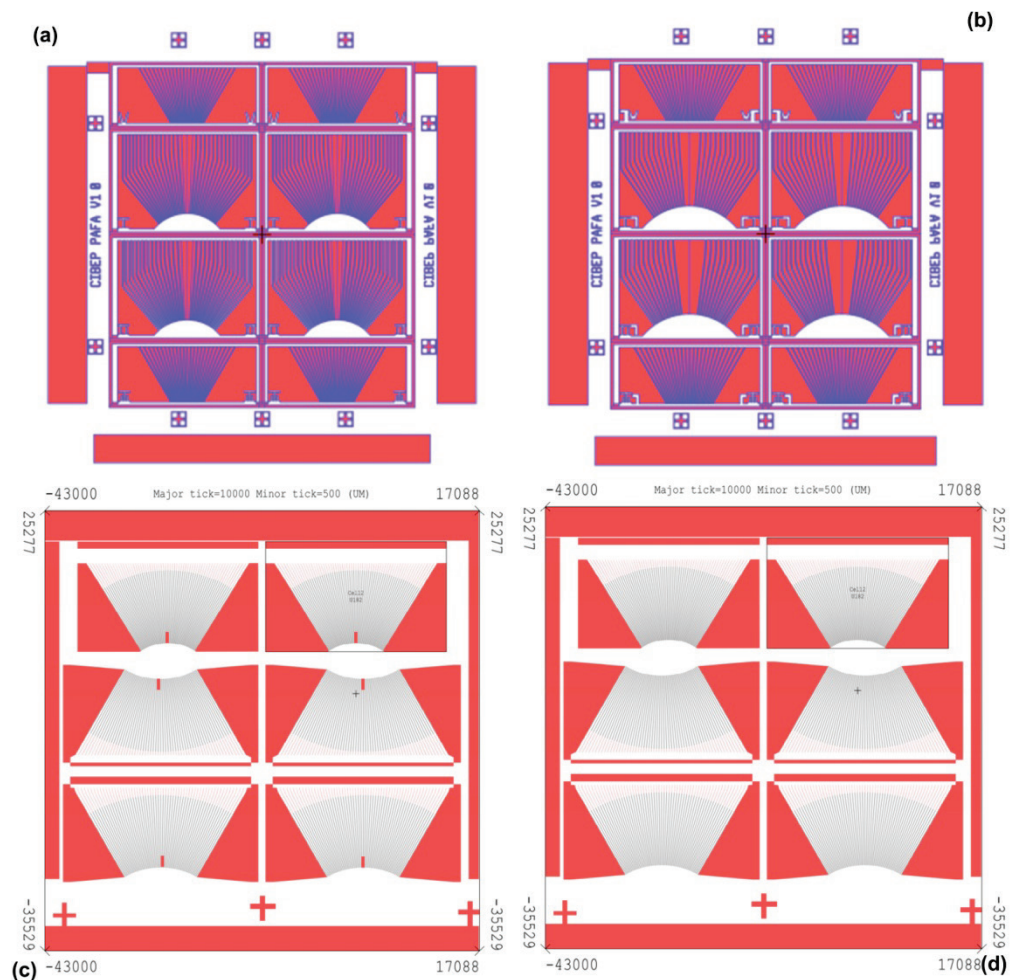
Fig. 2-8 Four chrome masks designed. (a) Constant aspect ratio designs with 5 mm focal length. (b) Constant aspect ratio designs with 7 mm focal length. (c)Constant acceptance angle designs with center channel blockage. (d) Constant acceptance angle designs without center channel blockage.

A steel mask was also designed for the aluminum sputtering process to coat a reflective layer to the bending and post-bending sections of the micro-channels as described in section 2.3.5. The design work was conducted via a software provided by eMachineshop.com and the mask was fabricated by them as well.

53
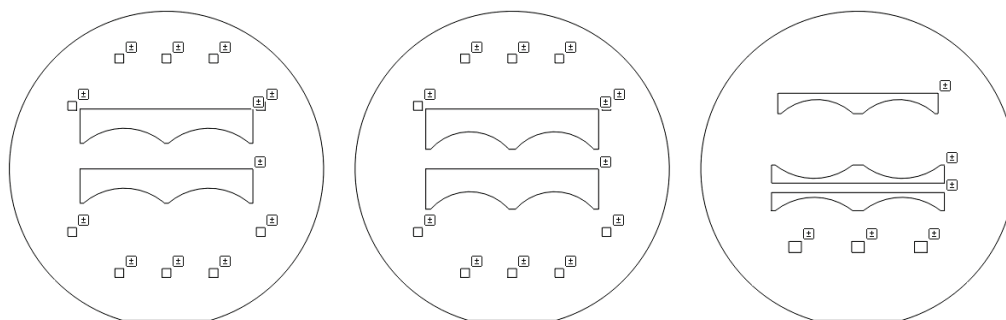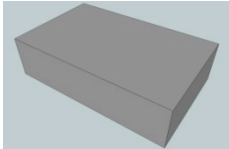
Fig. 2-9 Three steel masks for the aluminum coating process. The left one works with the chrome mask in Fig. 2-8(a). The middle one works with the chrome mask in Fig. 2-8(b). The right one works with the chrome masks in Fig. 2-8(c) and (d).

The mask was made of Steel 4140 hot rolled. Its thickness was 1.143mm. The feature tolerance was 0.25mm and the minimum curvature was 0.25mm.
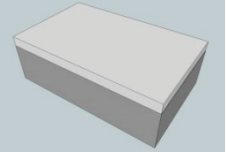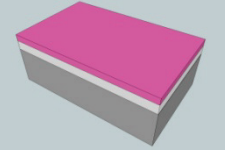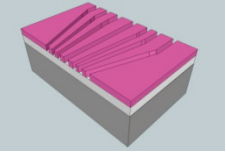
2.4.2. Lithography process
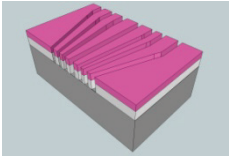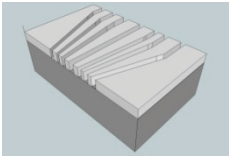
The entire fabrication process includes 40 steps and they are detailed in the table below:
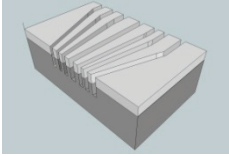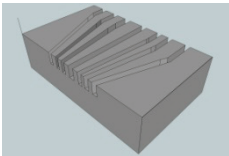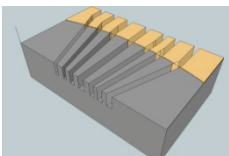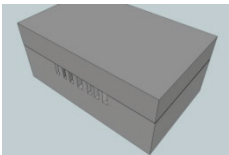
Table 2-3   RAFA fabrication process

Oxidation Preparation	1. Rinse the wafers and wafer boat by Acetone, IPA and DI water gun
	2. Immerse in 1:10 solution of HF + H_2O at 25 °C for 30 seconds to remove the native oxide *Notes:* ■ *1500 ml DI H_2O and 150 ml HF. The volume is sufficient to cover 8 wafers in dippers in a 2L plastic beaker. Major flats up.*
	3. Rinse the wafer with DI water for 2 mins

	4. RCA-1 Organic Clean, 1:1:5 solution of 30% NH_4OH (Ammonium Hydroxide) +50% H_2O_2 (Hydrogen Peroxide) + H_2O (water) (1250ml DI water, 250ml NH_4OH and 250ml H_2O_2) at 75 °C for 10 minutes
	
	Notes
	
	   ■ *Temperature should be controlled at under 80°C, not too much NH_4OH*
	   ■ *The volume should be sufficient to cover 8 wafers in dippers in 2000 mL glass beaker, major flats up.*
	   ■ *Hydrate wafers in DI water before placing in RCA-1. Heat water first then add NH_4OH and then H_2O_2. Stabilize temperature. Remove wafers from DI water and place them in RCA-1 and begin timing while the temp is in range*

	5. Rinse the wafer with DI water for 3 mins
	6. Oxide stripe: immerse in 1:50 solution of HF + H_2O at 25 °C for 30 seconds
	7. Rinse the wafer with DI water for 2 mins

	8. RCA-2 Ionic Clean, 1:1:6 solution of 38% HCl + 50% H_2O_2 + H_2O at 75 °C (1050ml DI water, 175 ml HCl and 175ml H_2O_2) for 10 mins
	   Notes
	
	   ■ *Heat water first. Add HCl and then H_2O_2. Note that the addition of HCl may cause solution temperature to rise significantly. Stabilize temperature before proceeding the next step*
	   ■ *Begin timing while the temp is in range*

	9. Rinse the wafer with DI water for 3 mins

	10 (Optional). Oxide stripe: immerse in 1:50 solution of HF + H$_2$O at 25 °C for 30 seconds
	11 (Optional). Rinse the wafer with DI water for 2 mins
	12. Spin and blow dry the wafer with nitrogen. *Notes* ■ *Spin at max RPM until dry (false colors disappear). Check for water on back. Repeat spin and/or blow dry it with dry N2*
Wet Oxidation	13. Grow thermal Silicon Oxide to 750 nm. 130 mins at 1100°C wet oxidation for 780 nm *Notes* ■ *Load 4 wafers in one boat and don't overload it due to weight concern* ■ *The final thickness was slightly thicker than 750nm, the measured maximum thickness is around 830nm*
Photoresist	14. Pre-bake at 100ºC for 20 min in the oven. Then cool to room temperature before spin photoresist.
	15. Spin Photoresist (Shipley SPR2). 4000 RPM for 30 seconds *Notes* ■ *While place the wafer on the plate, use an additional tweezers to help to hold the wafer and prevent it from dropping* ■ *Run a trial spin to make sure that the sample is centered properly before drop photoresist on the wafer* ■ *Sufficient photoresist should be applied to flood the entire surface before spinning.*
	16. Soft bake at 100ºC for 20 min in the oven
	17. Place the sample and the mask in the aligner. Near UV exposure 15 seconds
	18. Use MF319 to develop for 60-65 seconds

Pattern	19. Rinse with DI water for 3 min
	20. Do not spin, blow dry with N_2 and bake briefly in soft bake oven if necessary.
	21. Inspection
Wet Etching	22. Hard bake at 120ºC for 20 min in the oven
	23. Wet etch the SiO_2 with buffered HF (BOE, HF:NH4F 1:8 for ~100 nm/min at the room temperature). The etching time for 750 nm SiO_2 layer is around 9.5 minutes, minimum 8.5 minutes. *Notes:* ■ *Determine the end point by eye according to whether the dewetting occurs*
	24. Rinse with running DI water for 10 min
Strip Photoresist	25. Inspect under microscope and measure the height of the channels with the profilometer to confirm the completion of etching. *Notes* ■ *ENSC cleanroom profiometer operating procedure: Start the program AS5 → Select catalog → Select SCNZTH1000 and press enter → Change to Z~θ mode → Use up/down arrow buttons to lower the stylus → Find the structure → Press the start button and start the scan → Level the obtained image → Print the screen and exit → Restart the program to reposition*
	26. Strip the photoresist by soaking the wafer in Acetone until the resist is dissolved. Soak in fresh Acetone for a further 1~2 min.
	27. Rinse with running DI water for 3 min

	28. Spin dry or blow dry with N_2
Deep RIE	29. SF_6 at 330 sccm for 7 sec
	30. C_4F_8 at 120 sccm for 2.5 sec
	31. Run at 20ºC with etch rate of 80μm/16min. Plasma power 1800W and substrate power 120W
Strip Mask SiO₂	32 Strip the SiO_2 with BOE as described in step 23. The end point is determined by the occurrence of the dewetting.
	33. Rinse with running DI water for 10 min
	34. Spin dry or blow dry with N_2
Sputter Aluminum Coating	35. Load the wafer and the steel mask. Align them manually.
	36. Pre-sputtering: RF: 300W, time: 20 min, rotation, Argon 15 cc/min, pressure 1E-2 mbar *Notes* ■ *Target is 99.99% pore Aluminum layer* ■ *Equipment: Kurt J. Lesker Company, Clairto, PA*
	37. Sputtering: same conditions as Step 36 but last for 90 min. Target thickness 1 μm.
Device Assemble	38. Dice the patterned wafer.
	39. Dice a raw wafer with the same geometry as the patterned wafer. It functions as the capping layer
	40. Insert both device and the cap into the slit of the sample holder and clamp them together with plastic screws.

2.4.3. Device assembly

A cradle was employed to clamp a polished silicon cover piece onto the surface of the patterned silicon substrate to enclose the RAFA. The slot aperture at the incident side was 200 μm and the position was designed to match the RAFA channel aperture (Fig. 2-10 (a)). There were two plastic screws to clamp both cover piece and the substrate piece together. The alignment between RAFA and the slot aperture could be adjusted via tightening or loosening one of these two screws (Fig. 2-10 (a) and (b)). A sample measurement system was presented in Fig. 2-10 (c) where the cradle was mounted to a 6 degree-of-freedom sample holder. It could adjust *x, y, z, roll, pitch* and *yaw* to ensure the optical axis of the RAFA was aligned with the collimated incident laser beam.
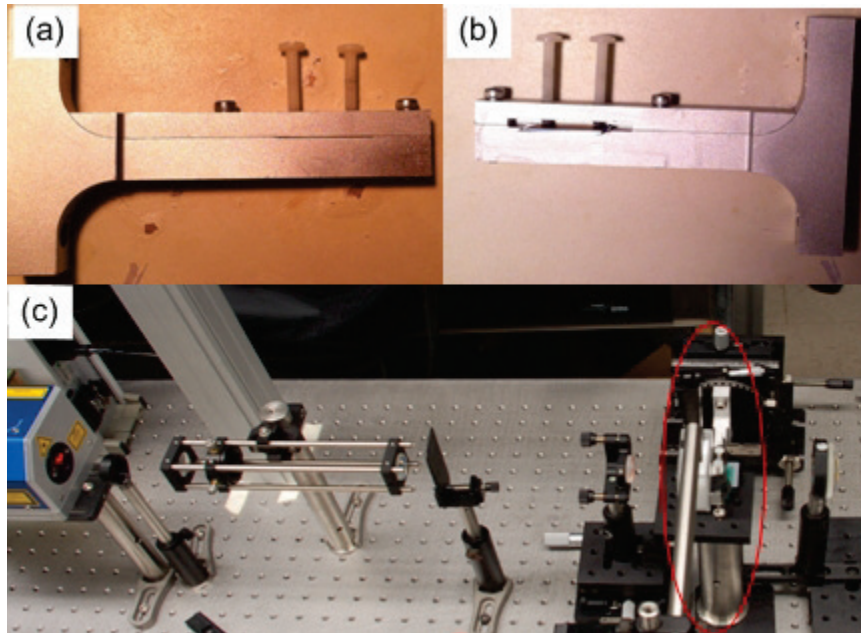
Fig. 2-10 (a) Front view of the cradle, (b) back view of the cradle, (c) the cradle was mounted onto a 6 degree-of-freedom sample holder in the experiment setup to ensure that the OA of RAFA is aligned to the direction of the collimated incident beam.

3. Characterization of Radial Angular Filter Array

3.1. Objective

The primary goal of this chapter was to characterize the proposed new device designs, in particular, to examine the inter-channel cross talk, channel leakage, and channel achromaticity to validate the design improvements. The second goal was to calibrate the device and demonstrate the usefulness of the RAFA as a device suitable for obtaining angle-resolved hyperspectral measures of light scattered from a turbid sample.

Our approach was to develop a setup to characterize the new RAFA devices first. Then, a RAFA calibration procedure was established with a focused uniform broadband beam. The characterization results were used to assess whether the fabricated devices satisfied the design targets. Finally, the RAFA device design with the best performance was integrated into a hyperspectral imaging system to perform angularly-resolved spectroscopy analysis of turbid media with or without spectrally absorptive contents .

3.2. Characterization system

3.2.1. Device characterization

The optical and SEM images of RAFA design 1 in Table 2-2 were presented in Fig. 3-1. Fig. 3-1(a) was a plan-view of RAFA and illustrated that this RAFA included a bending section within each channel, which re-directed light perpendicular to output edge of the RAFA to simplify camera coupling. This image also demonstrated that the bending section and post-bending section were coated with a thin aluminum layer as shown in a light white color. Fig. 3-1(b) highlighted the channel walls in the pre-bending

sections which were patterned with vertical ridges (width of 5 µm) at a spatial period of 10 µm to trap light travelling in a direction outside of the acceptance angle. The channel height of the RAFA was measured in Fig. 3-1(c) and it was ~ 60 µm. The surface roughness of the coating layer was evaluated in Fig. 3-1(d). It was less than the 200 nm, about a quarter of the interested wavelength of light (NIR), which ensured reflections were similar to an ideal mirror-reflection.
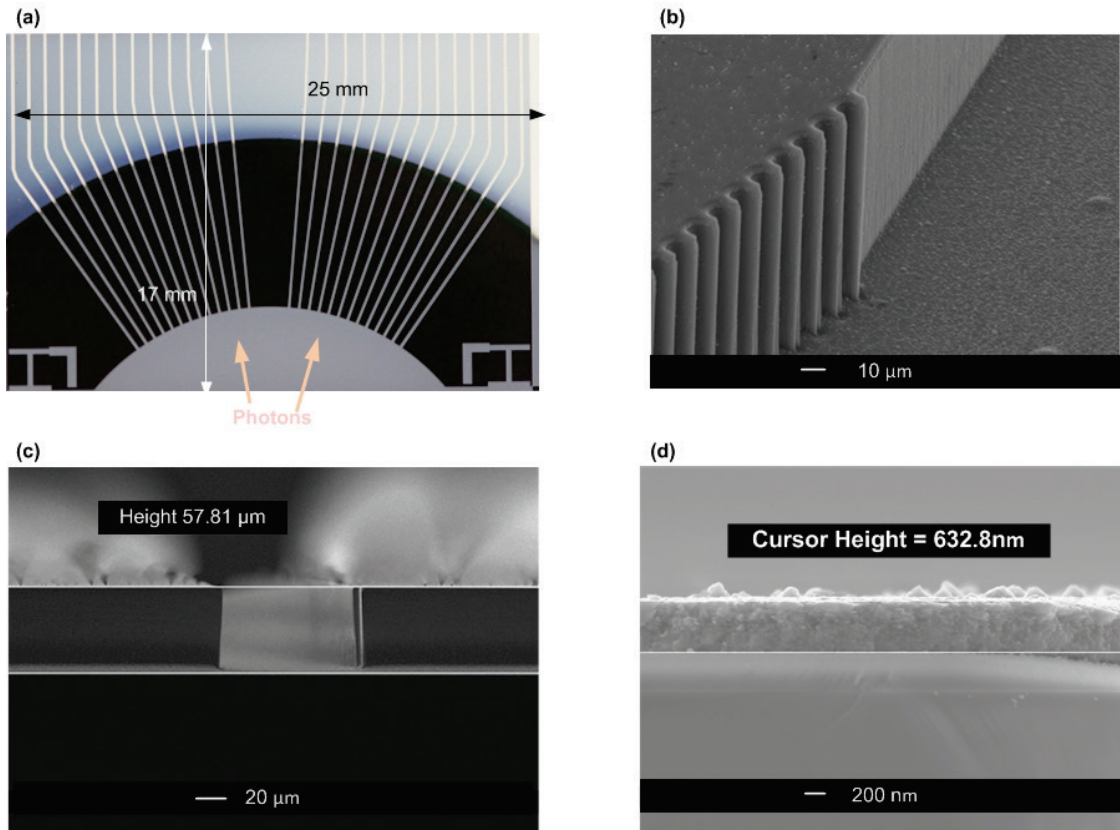
Fig. 3-1 (a) A plan-view of the RAFA (the top piece was removed). Lighter area was coated aluminum. (b) A magnified view of a channel sidewall at the junction between the pre-bending section and bending section. (c) A cross-section image showing the height of the channel. (d) A side view of the coating layer at the bending section. Figure adapted from reference [127].

3.2.2. *Optical measurement system*

The RAFA characterization setup consisted of a broadband light source, a diffuser, near infrared filters, collimation optics, a focusing lens, one RAFA and a spectrometer (Fig. 3). Specifically, the output of quartz tungsten halogen (QTH) lamp (Oriel, Series Q Lamp Housing, 100 W) was spectrally filtered by a high pass filter (645 nm, part no. 65.1365, Rolyn Optics Co., Covina, CA) then a near infrared short pass filter (950 nm, 950FL07-50S, LOT-Oriel GmbH, Germany). The beam was homogenized by a 15° holographic diffuser and focused at a pinhole (1 mm in diameter). The light from the pinhole was collimated by a NIR doublet spherical lens (ACH-NIR 25×50, Edmond Optics, Barrington, NJ), then refocused by an achromatic objective lens (20×, NA=0.45; Nikon, 93150). A slice of the beam was collected by the RAFA held by a 6 degree-of-freedom jig (built from multiple components, Thorlabs, NJ) that enabled the alignment and mapping of the RAFA focal point to the focus of the beam and RAFA output to the slit of the spectrometer, the placement of the RAFA at the center of the circular beam, and the adjustment of the distance between the RAFA and the spectrometer. The output of the RAFA was directly coupled into the slit of an imaging spectrometer (CCD sensor: C10151-S10141-1109, Hamamatsu Photonics K.K. Japan, 2048 × 506 active pixels, 12 µm×12 µm pixel size, 650 nm – 950 nm; spectrometer assembled by P&P Optica Inc., Kitchener, Canada). It is a pushbroom imaging spectrometer. The long axis of its pixel array is aligned to the direction of the input slit and the spatial signal is recorded in rows. With RAFA, the spatial signals carry the angular information. The spectroscopic information is mapped vertically to the slit and recorded in columns. This allows multispectral analysis of a line image without scanning the wavelength. The acceptance angle of the spectrometer at the slit was approximately 9° (F/3). The slit was 25 mm horizontally and 1 mm high. The spectral resolution of the CCD sensor was 0.05 nm (wavelength) / µm (spatial distance). The spectral resolution of the measurement system was defined by the height of RAFA channel (60 µm) and was approximately 3 nm. With this setup, both the angular and spectral distributions of light at the focal point of the RAFA could be captured without mechanical scanning or rotation. The readout time for each image was less than 3 seconds.

3.2.3. RAFA calibration

The angular distribution of transmitted light was typically presented as the Bidirectional Transmission Distribution Function (BTDF) as discussed in section 1.2.1. Neither the NIR output spectrum from the QTH lamp, nor the quantum efficiency of the spectrometer across the NIR was uniform. This setup specific variation was defined as the setup signature. Furthermore, like other optical devices, each RAFA introduced device specific variation to the measurement results, which was defined as the device signature. With the calibration setup as shown in Fig. 3, each channel of the RAFA received the same incident light intensity and a reference $BTDF_0(\theta_{s0},\lambda)$ was estimated with:

$$BTDF_0\left(\theta_{s0},\lambda\right) \cong \frac{P_{s0}\left(\lambda\right)}{P_{i0}\left(\lambda\right) \cdot \cos\theta_{s0} \cdot \Omega_{s0}} \quad , \tag{3.1}$$

where $P_{i0}(\lambda)$, $P_{s0}(\lambda)$, Ω_{s0}, and θ_{s0} represent the values associated with the reference measurement. The setup and device signature are intrinsic to $BTDF_0(\theta_{s0}, \lambda)$, which can be used to correct experimental measurements with the same device. Equation (3.1) can be re-written as:

$$\frac{P_{s0}(\lambda)}{BTDF_0(\theta_{s0},\lambda)} = P_{i0}\left(\lambda\right) \cdot \cos\theta_{s0} \cdot \Omega_{s0} = A_0(\theta_{s0},\lambda) \quad , \tag{3.2}$$

where $A_0(\theta_{s0}, \lambda)$ represents the RAFA device and setup signature. Since $P_i(\lambda)$, Ω_s, and θ_s were kept the same between at the reference measurement and during subsequent measurements, $BTDF(\theta_s, \lambda)$ was then computed for each device using

$$BTDF\left(\theta_s,\lambda\right) \cong \frac{P_s(\lambda)}{P_i\left(\lambda\right) \cdot \cos\theta_s \cdot \Omega_s} = \frac{P_s\left(\lambda\right)}{A_0\left(\theta_{s0},\lambda\right)} \quad . \tag{3.3}$$

Equation (3.3) states that the $BTDF(\theta_s, \lambda)$ of a specimen can be obtained by normalizing the measured intensity at each channel output by $A_0(\theta_{s0}, \lambda)$.

3.2.4. Setup for Intralipid^{TM} experiments

Once the RAFA was calibrated, it was used to measure the light scattering due to a series of Intralipid^{TM} dilutions. Intralipid^{TM} has been used as a tissue simulating

phantom medium, whose scattering coefficient is about two orders of magnitude higher than the absorption coefficient in NIR. The optical scattering within Intralipid[TM] is expected to be forward-oriented with g around 0.75 [87, 88]. Intralipid[TM] dilutions (0.05 wt%, 0.1 wt%, 0.5 wt% and 2.0 wt%) were diluted from 20 wt% stock Intralipid[TM] (Fresenius, Kabi AB, Uppsala, Sweden) with distilled-deionized water. For a given experiment, the setup was similar to the apparatus shown in Fig. 3-2. However, the 20× objective lens was removed. An iris and a 5 mm optical path length cuvette was placed in front of the RAFA, and the focal point of the RAFA was aligned to and within the cuvette. The diameter of the collimated incident beam was adjusted by the iris (from 3 mm to 10 mm). The adjusted beam then illuminated the cuvette loaded with the Intralipid® dilution, where the bulk scattering occurred.
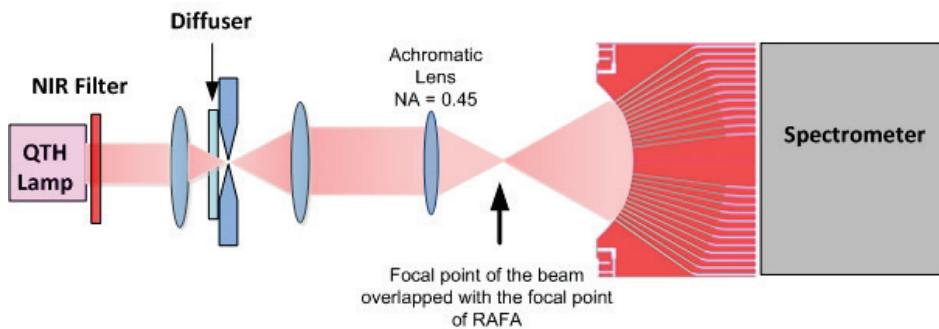
Fig. 3-2 Experimental setup for calibrating a RAFA. The achromatic lens was replaced by an iris and 5 mm cuvette in the Intralipid[TM] experiment. Elements in the diagram are not to scale. Figure adapted from reference [103].

3.3. Characterization results

3.3.1. Output coupling

The RAFA output coupling measurement focused on evaluating the design that offered the minimum RAFA/detector coupling loss. It was performed with uniform incident light at all RAFA input angles. The output of the RAFAs that included bending structures was fully captured by the spectrometer as the output beam angle of the RAFA was compatible with the input acceptance angle (± 9°) of the spectrometer. However, the characterizations of the RAFAs that lacked bending structures were limited to lower

angle measurements since the high angle channel outputs were outside the acceptance angle of the spectrometer. Fig. 3-3(a-d) show the RAFA output light intensity profiles captured with the spectrometer for RAFAs described in Fig. 2-3(a-d), respectively. Signals from all channels were captured for designs (Design 5 and 9 in Table 2-2 and shown in Fig. 2-3(a) and (b)) (see Fig. 3-3(a) and (b)), but only signals from central channels were observed for designs (Design 6 and 10 in Table 2-2 and shown in Fig. 2-3(c) and (d)) (see Fig. 3-3(c) and (d)), which indicated that the setup could only fully characterize RAFAs that contained bending structures. Fig. 3-3(a) and (b) also revealed that the channel signals with these two designs were of the similar magnitude across the entire profile, which was significantly better than the earlier device (see Ref. [86]), where the variation in signal intensity across the channels due to the device signature was several orders of magnitude.
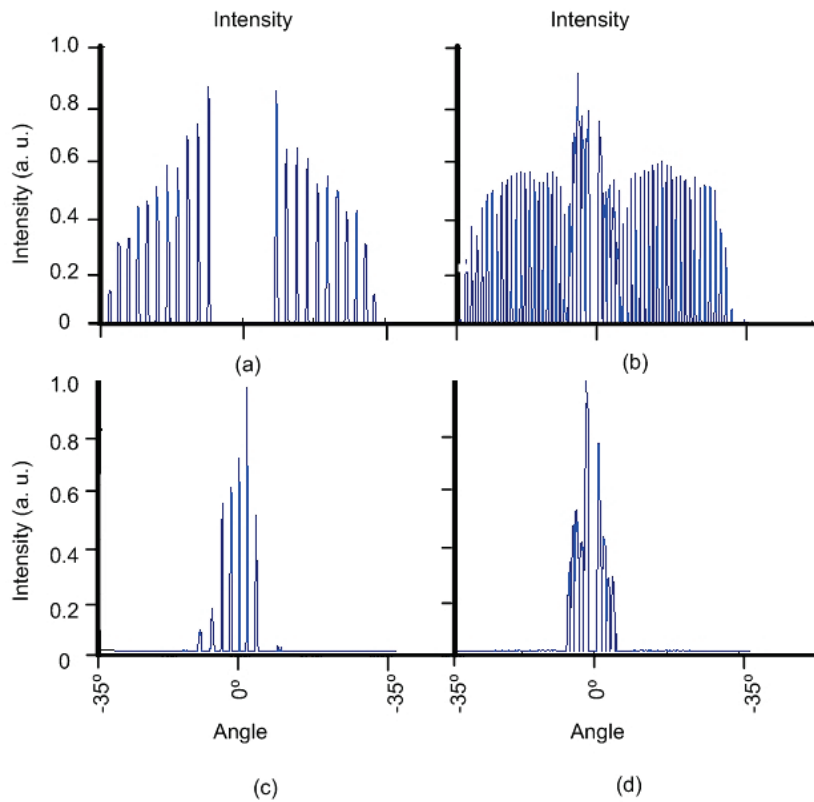
Fig. 3-3 Light scattering profiles of an angularly uniform incident beam measured with RAFA devices. Panels (a-d) correspond to RAFA designs shown in Fig. 2-3(a-d), respectively [103].

3.3.2. Crosstalk measurement

Inter-channel crosstalk was evaluated with ray-tracing simulation in section 2.3.7 and further validated by experimental measurements. The experiment was performed with RAFA channels of 30° angle with the similar dimension as the channel inside the conceptual RAFA in Ref. [86]. The result showed that <1% and 20% of the incident power was preserved by the curved and the micro-mirror bending structures, respectively. It was consistent with the ray-tracing results and confirmed that the design change proposed in section 2.3.3 increased channel transmission efficiency and reduced crosstalk to a satisfactory level. It was noted that the measured signals were weaker than the simulated results. The cause might have been due to a lower than expected channel surface reflectivity.

For the original device with the curved bending structure (see Ref. [86]), crosstalk was evident at the output of adjacent channels even after 1 mm of propagation in the air. The improvement in the output beam collimation was validated by an RAFA with a constant aspect ratio of 120:1 (Design 1 in Table 2-2). Uniform incident beams were projected to the RAFA at all angles. Fig. 3-4(a-c) showed the measured intensity profiles at different distances away from the channel output. The measurements clearly demonstrated that the crosstalk between output channels was negligible when the spectrometer input was 1 mm away from the channel output (Fig. 3-4(a)). When the spectrometer was placed 6 mm away from the output of the RAFA, background noise due to crosstalk between output channels became noticeable as shown in Fig. 3-4(b). The output signal was degraded substantially by inter-channel cross talk when the spectrometer was 11 mm from the output of the RAFA (Fig. 3-4(c)).
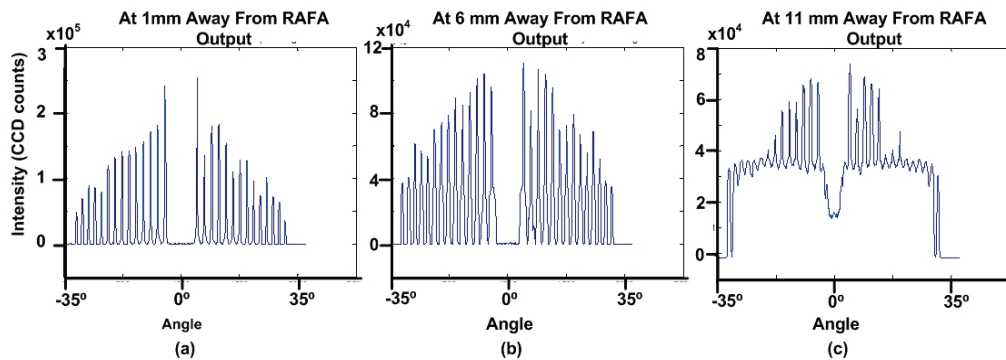
Fig. 3-4 The measured intensity profile for with an angularly uniform incident beam with one RAFA (constant aspect ratio of 120:1) (a) at 1 mm away from the device output (b) at 6 mm away from the device output and (c) at 11 mm away from the device output. Data represents cumulative camera counts for 10 images. Figure adapted from reference [103].

One important goal of crosstalk measurement was to compare the difference between constant aspect ratio designs and constant acceptance angle designs. In this project, the evaluation was conducted with a series of Intralipid[TM] samples from low to high scattering level as described in section 3.2.4. The test results with design 1 and design 9 in Table 2-2 were presented in Fig. 3-5 and Fig. 3-6, respectively. Design 1 represented constant aspect ratio designs and design 9 represented constant acceptance angle designs. They had the same focal length and overall device dimension. The optical scattering profiles for the specimens with 0.1 wt%, 0.5 wt% and 1 wt% Intralipid™ were captured and the device signature was accounted for. The profile of lights existing 0.1 wt% Intralipid™ sample could not be considered Lambertian and the measured intensity in center channels was higher than that in the side channels due bulk scattering in the forward direction [87, 88]. As the sample concentration increased, the scattered light profiles approached Lambertian profiles. The measured results indicated that once the concentration of the Intralipid™ was higher than 0.5 wt%, the specimen could be considered as a near Lambertian scattering source.

Higher signal non-uniformity was observed in Fig. 3-6 than Fig. 3-5, particularly in channels close to the specular direction. With design 9, channels within ± 6º had no bending structure and they had output angles within the numerical aperture of the imaging spectrometer. In addition, the signal loss in these channels was significantly less than that in other channels due to the lack of bending. The leaked photons in these

near specular channels might also within the numerical aperture of the imaging spectrometer. Design 9 was a constant acceptance angle design and its channel separation at the output was smaller than that in constant acceptance angle designs. All of these above contributed to high background noise at the micro-channels with outputs near the optical axis of the RAFA. Due to the strong background in the center channels, the device output was beyond the dynamic range of the detector in some cases, causing saturation in the center. Reduction of the total exposure time to limit signal at the center channels resulted in the signals from the high angle channels becoming undetectable (see Fig. 3-6(b) and Fig. 3-6(c)). Channels between ± 6º and ± 10º were in the transition between bending and no bending. The background signal reduced dramatically during this transition. The large change in the background tended to obscure measurement of scattering variations due to the material properties. The measured scattering profiles (corrected for the device signature) were usually corrupted by abnormal micro-channel output measurements as shown in Fig. 3-6(d) and (e) . The corrected scattering profiles for the 0.5 wt% and 1.0 wt% Intralipid™ samples were expected to be constant. However, measurements obtained from the center channels were lower than those from the side channels (Fig. 3-6(e) and (g)), which was primarily an artifact of the large channel leakage in the center. Blocking of the center channels had minimal effect as only channel ± 1º of the specular direction were blocked. All the above issues were not significant in Fig. 3-5. It was primarily due to the consistency in bending structure, the collimation to the output signal from post bending structure and the efficient center channel blockage (between -5° and 5°) which prevented most leaked photons from center channels from entering the imaging spectrometer.
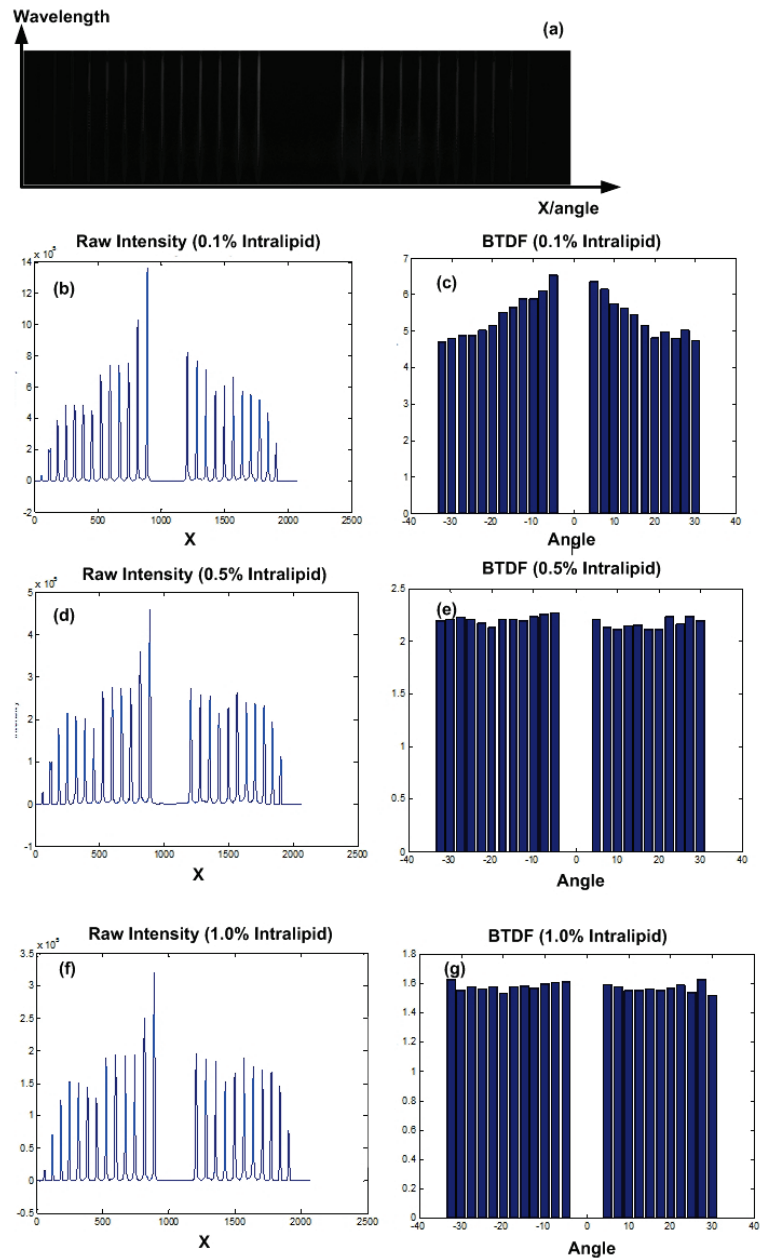
Fig. 3-5 Test results of design 1 in Table 2-2. (a) Output from spectrometer for a 2.0% Intralipid™ sample to obtain the device response. (b) Summation of pixels in each row to obtain the intensity profile independent of wavelength for a 0.1 wt% Intralipid™ sample. (c) Computed scattering profile of 0.1 wt% Intralipid™. (f) Intensity profile for a 0.5 wt% Intralipid™ sample. (g) Computed scattering profile of 0.5 wt% Intralipid™. (g) Intensity profile for a 1.0 wt% Intralipid™ sample. (i) Computed scattering profile of 1.0 wt% Intralipid™. Figure adapted from reference [89].

Overall, our results demonstrated that cross talk at the RAFA output was much more severe for constant acceptance angle designs compared to constant aspect ratio designs, which corroborated discussion presented in previous work (see Ref. [89]). Based on these findings and the earlier work, we chose to focus optimization and characterization efforts on constant aspect ratio designs.

3.3.3. Channel leakage

Channel leakage was measured for design 5 in Table 2-2 (shown in Fig. 2-3(a)). The apparatus described in Fig. 3-2 was used to obtain the measurements; however, the lens was removed. A collimated beam with a spectrum covering 720-770 nm was projected onto the input of the RAFA. The size of the beam was adjusted to ensure the coverage of all channel input openings. The light output ($P(\theta_c)$) of each channel with angle θ_c was recorded. For the test RAFA, the center channel was blocked; therefore, the experiment was repeated with an RAFA that had a single channel in the center along the specular direction. The single channel RAFA was designed to have the same aspect ratio, depth and photon trapping ridges as the test RAFA. The single channel RAFA was fabricated together with the other RAFAs, following the same process. The measured light output $P(0)$ from the single channel RAFA was treated as the reference intensity along the specular direction. The leakage represented by $L(\theta_c)$ of each channel was defined as:

$$L(\theta_c) = -\log_{10} \frac{P(\theta_c)}{P(0)} \quad . \tag{3.4}$$

(a)

Raw Intensity (0.1% Intralipid)

(b)

BTDF (0.1% Intralipid)

(c)

Raw Intensity (0.5% Intralipid)

(d)

BTDF (0.5% Intralipid)

(e)

Raw Intensity (1.0% Intralipid)

(f)

BTDF (1.0% Intralipid)

(g)
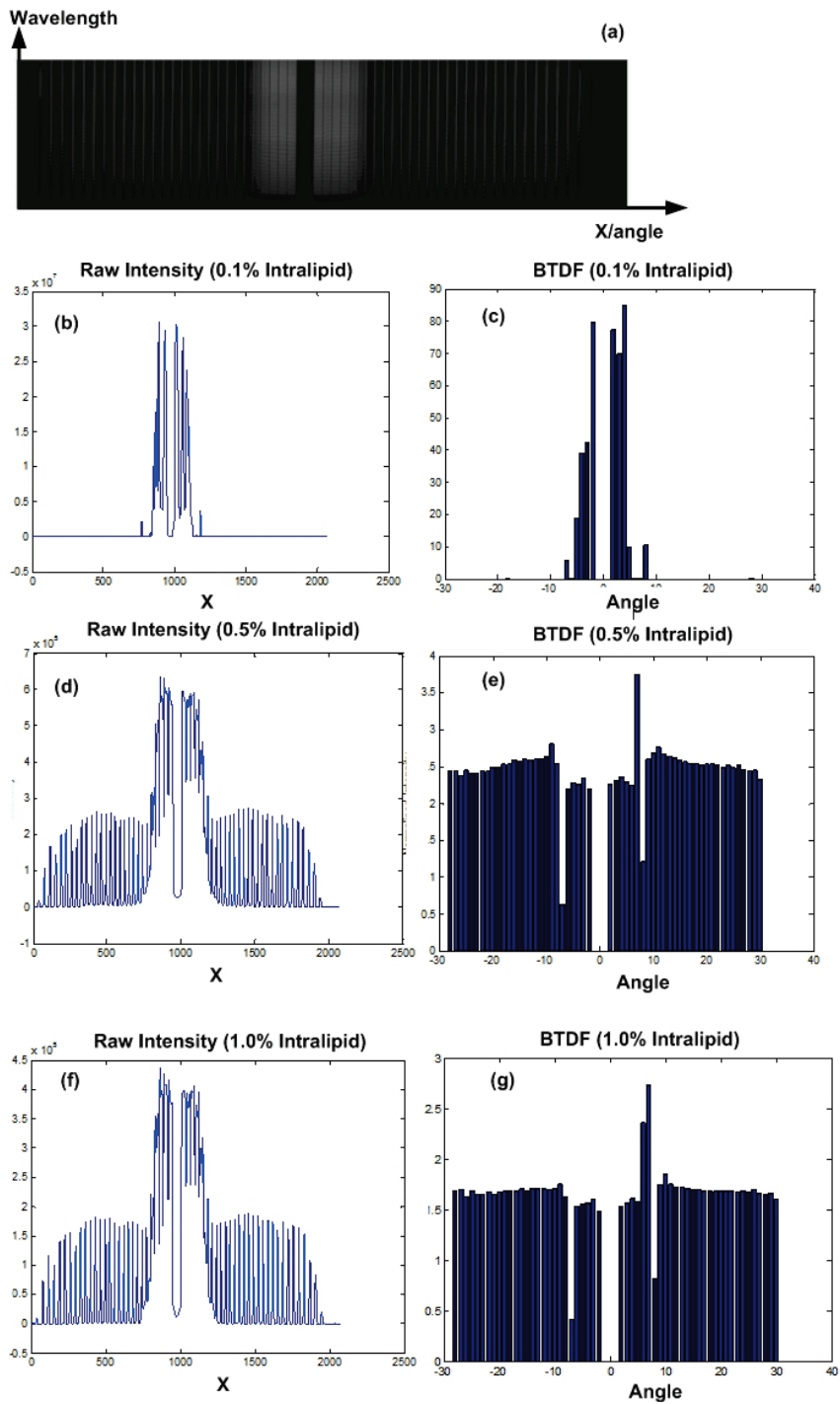
Fig. 3-6 The test results for design 9 in Table 2-2. (a) Output from spectrometer for a 2.0 wt% Intralipid™ sample to obtain the device response. (b) Summation of pixels in each row to obtain the intensity profile independent of wavelength for a 0.1 wt% Intralipid™ sample. (c) Computed scattering profile of 0.1 wt% Intralipid™. (f) Intensity profile for a 0.5 wt% Intralipid™ sample. (g) Computed scattering profile of 0.5 wt% Intralipid™. (g) Intensity profile for a 1.0 wt% Intralipid™ sample. (i) Computed scattering profile of 1.0 wt% Intralipid™. Figure adapted from reference [89].

The measurement results are presented in Table 1. The leakage for channels with $|\theta_c| > 27.5°$ was not presented due to low signal. In general, the test RAFA demonstrated low channel leakage for all θ_c when adequate signal was present. For channels with $|\theta_c| = 7.5°$, the leakage signal was $< 10^{-4}$ of the incident light in the specular direction, and $\leqslant 10^{-5}$ for channels satisfying $17.5° \leqslant |\theta_c| \leqslant 27.5°$.

Table 3-1   Leakage measurement results for RAFA design 5 in Table 2-2 (shown in Fig. 2-3(a)) [103]

θ_c (°)	-27.5	-25.0	-22.5	-20.0	-17.5	-15.0	-12.5	-10.0	-7.5
L	5.4	5.4	5.1	5.0	5.0	4.8	4.7	4.4	4.1
θ_c (°)	27.5	25.0	22.5	20.0	17.5	15.0	12.5	10.0	7.5
L	5.5	5.5	5.4	5.2	5.0	5.1	4.8	4.7	4.2

ᵃThe upper row represents measurement results from channels located on the left side of the specular direction from -27.5° to -7.5° while the bottom row represents measurement results from channels located on the right side (7.5° to 27.5°).

3.3.4.   Achromaticity of RAFA

The RAFA was expected to have achromatic transmission characteristics due to the size of each channel aperture being significantly larger than the wavelength of visible and NIR light. The achromatic property of design 5 in Table 2-2 (shown in Fig. 2-3(a)) was investigated by a reference measurement with a focused broadband beam (see apparatus in Fig. 3-2). The light output of the RAFA was captured by the spectrometer, then interpolated and mapped into a 2D map (Fig. 3-7). Since the numerical aperture of the achromatic lens was 0.45, the analysis was restricted to channels with $|\theta_c| \leqslant 22.5°$. The angular resolution of the measurement prior to interpolation was 2.5°. During data processing, the signal intensities for every 12 nm were added together to reduce

periodic noise inherent to the imaging spectrometer (due to etaloning). The resultant spectral resolution and angular resolution of the final 2D map were interpolated to 1.2 nm and 0.25°, respectively. The data at each angle was normalized as a function of wavelength to the median value (Fig. 3-7(a)). The normalized 2D map revealed that the spectral response due to the setup/device signatures was similar for the angles tested. The data for each wavelength was normalized as a function of angle to the median value (Fig. 3-7(b)). The resultant 2D map showed that the angular response was consistent across the different spectral bands to within ±10% of the mean. Therefore, the transmission properties of the RAFA did not depend greatly on wavelength.
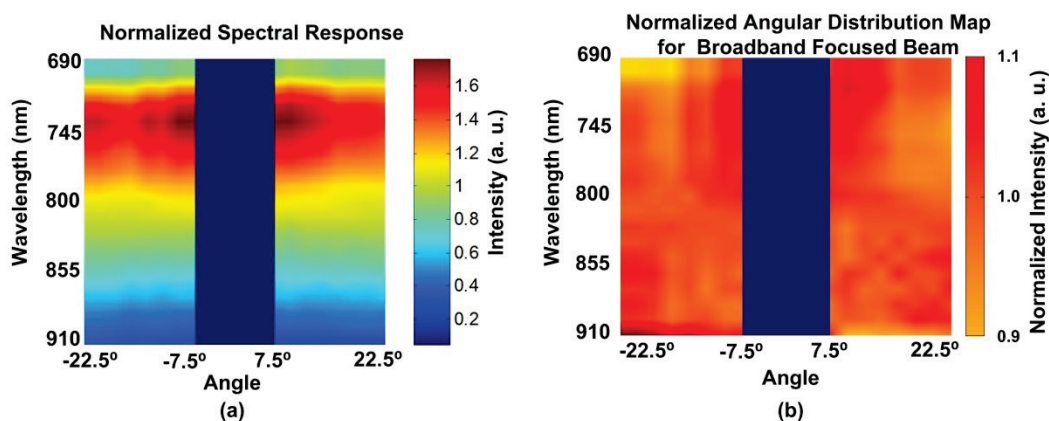
Fig. 3-7 (a) Measured light intensity after normalization to the median intensity across the spectral range at each angle. (b) Light intensity after normalization of data shown in panel (a) to the median intensity across the angular range at each wavelength. Figure adapted from reference [103].

3.4. Trial applications

3.4.1. Use of an RAFA for angle-resolved spectroscopy of a turbid medium

Characterization of Intralipid^{TM} samples prepared in Section 3.3.2 was performed with the selected RAFA design (design 5 in Table 2-2) . Measurement results for 0.05 wt%, 0.1 wt%, 0.5 wt% and 2.0 wt% Intralipid^{TM} dilutions at each channel were corrected for the setup and device signatures and plotted in Fig. 3-8(a-d). To improve interpretation, the light output of each channel was normalized as a function of angle to

73

the peak intensity value at each wavelength. The normalized results were assembled into a 2D intensity map (wavelength versus angle) (Fig. 3-8(e-h)). The 2D map had the same spatial and spectral resolutions as described in Section 3.2.2 and 3.2.4. A slight asymmetry was observed between the left and right halves of the spectral map. The cause of the asymmetry was not fully determined; however, it could be due to a slight rotation of the sample surface with respect to the RAFA or the presence of defects in the RAFA channels.

The results were evaluated from four perspectives: location of the intensity peak, intensity versus angle, intensity versus Intralipid^{TM} concentration and intensity versus wavelength. First, the peak values in the angle-resolved intensity spectra were located at the longest wavelength and at angles of ±7.5° (Fig. 3-8(a-d)) for all Intralipid^{TM} dilutions. This result was consistent with the fact that scattering was lower at longer wavelengths. Second, the intensity distribution across all angles was more uniform as the concentration of Intralipid^{TM} increased. The intensity ratio between the output from the high angle channels and the central channels (±7.5°) increased with the concentration of Intralipid^{TM} (see Fig. 3-8(a) to (d)). With 2.0 wt% Intralipid^{TM}, the ratio was nearly 1, indicating that the intensity variation between different RAFA channels was negligible when the scattering was high. The finding was also observed in Fig. 3-8(e-h), where the angle-resolved intensity spectrum was least uniform for the sample with 0.05 wt% Intralipid^{TM}, but was nearly flat for the sample with 2.0 wt% Intralipid^{TM}. Third, it was noticed that the intensity at the output of high angle channels increased when the Intralipid^{TM} dilution was increased from 0.1 wt% to 0.5 wt% and decreased afterwards. Such biphasic behavior was not observed for channels close to the center (e.g. ±7.5°), where the intensity dropped as the concentration of Intralipid^{TM} increased. The primary reason for this phenomenon was due to the multiple effects of the scattering. At a higher scattering level, more photons would be delivered to high angle channels via scattering, causing the intensity reduction for central channels, but an intensity increase for higher angle channels. At the same time, fewer photons overall would survive the transit through the cuvette as the concentration of Intralipid^{TM} increased. The net effect of the above two effects could explain the biphasic intensity versus Intralipid^{TM} concentration relationship for high angle channels and the consistent drop in intensity with increasing Intralipid^{TM} concentration for channels more closely aligned with the optical axis. Last, it

was noticed that the spectra were somewhat U-shaped for Intralipid[TM] at lower concentrations. As the concentration increased, the U-shaped spectra evolved into a monotonic shape that increased from short to long wavelengths. The spectra were nearly flat for the 2.0 wt% Intralipid[TM] dilution. The shape transition in the intensity spectra could have resulted from the interaction of two processes. First, as described in Ref. [78], scattering decreases at longer wavelengths, particularly when the Intralipid[TM] concentration is low. This results in an intensity increase for all channels from short to long wavelength. Second, as described above, fewer photons overall would be scattered into higher angle channels at longer wavelengths, causing the intensity to drop. These two effects are illustrated in Fig. 3-9(a) and (b). The combination of them could potentially explain the intensity versus wavelength relationship observed in Fig. 3-8(a-d).
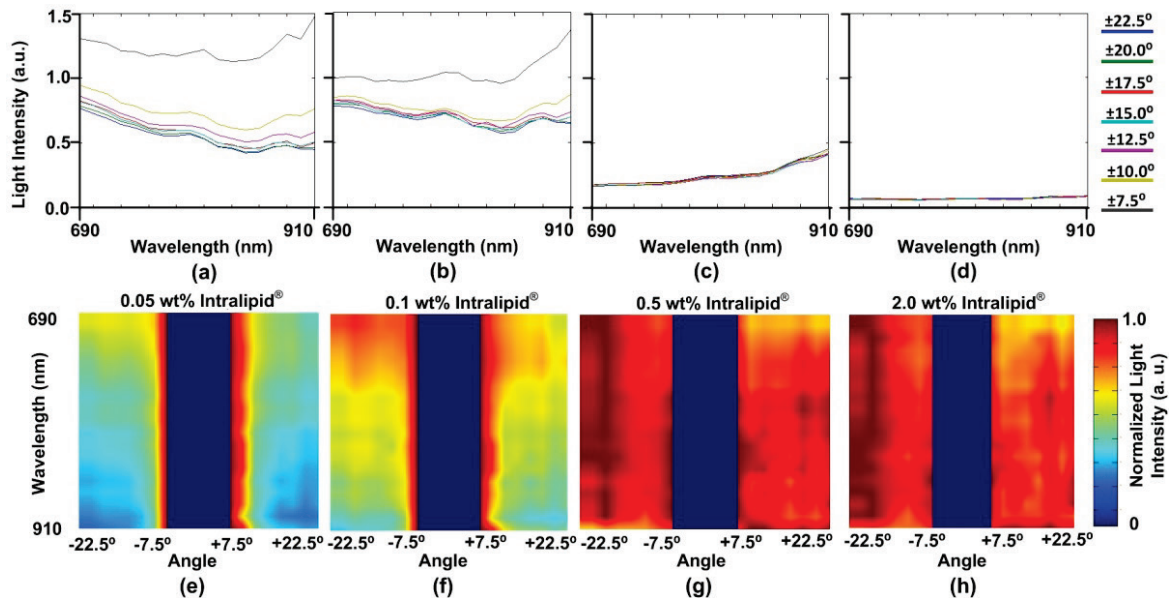
Fig. 3-8 (a-d) Measured channel signals at each angle across the spectral range of 690 nm to 910 nm for 0.05 wt%, 0.1 wt%, 0.5 wt% and 2.0 wt% Intralipid[TM] dilutions, respectively. (e-h) Angle-resolved spectral maps of intensity for wavelength range of 690 nm to 910 nm, and an angle range of -22.5° and +22.5° corresponding to panels (a-d), respectively. Intensity is displayed in arbitrary units. Figure adapted from reference [103].

75
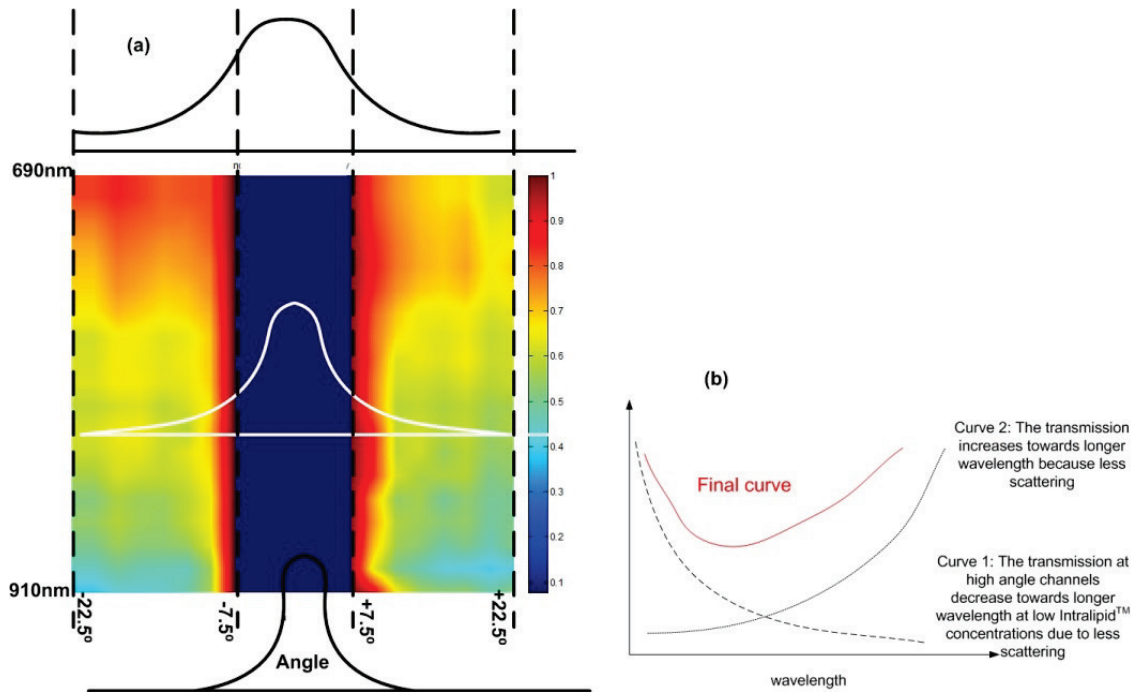
Fig. 3-9 (a) Light intensity at high angle channels dropped when the photon wavelength increased with 0.1% IntralipidTM. (b) Measured IntralipidTM total attenuation spectrum was generated from two competitive processes

3.4.2. Use of an RAFA for angle-resolved spectroscopy of an spectrally-absorptive turbid medium

The characterized RAFA was also employed to measure the angular spectra of mixtures of Intralipid[TM] (0.05 wt%, 0.1 wt% or 0.5 wt%) and Indocyanine Green (ICG) (I2633-25MG, Sigma Chemical Co., St Louis, MO) mixture. Mixtures were prepared by dissolving ICG in dd-H2O and then mixing with an Intralipid[TM] solution to achieve a concentration of 5 µM ICG. The absorption spectra of ICG and the total light attenuation spectra of Intralipid[TM] at different concentrations are presented in Fig. 3-10(a) and (b), respectively. The ICG spectra were calculated from the literature data [90, 91] while the later was obtained experimentally via measuring light transmitted through a 1 cm cuvette filled with Intralipid[TM] dilution in different concentrations) [73]. Please note that the majority of the measured attenuation was due to scattering.
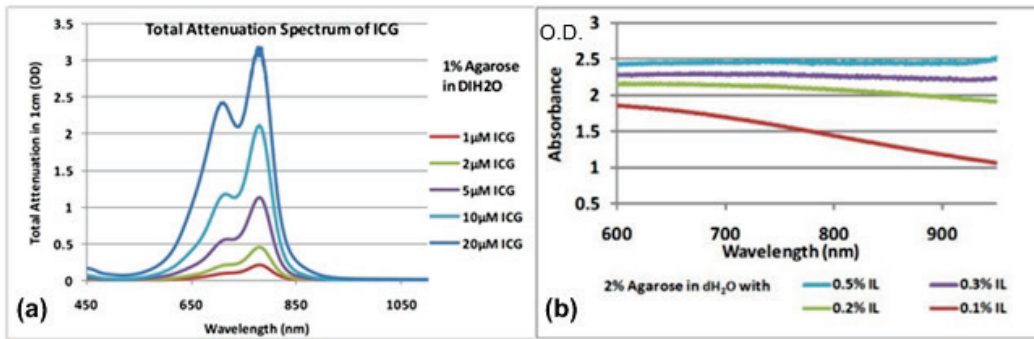
Fig. 3-10 (a) Total attenuation spectrum of ICG at different concentrations [88, 90]. (b) Measured total attenuation spectra of Intralipid^{TM} in different concentrations.

Measurement results for 0.05 wt%, 0.1 wt% and 0.5 wt% Intralipid^{TM} with 5 μM ICG solutions were presented in Fig. 3-11(a-c) respectively.   A strong absorption band was visible in all three figures and the location of the band matched with the absorption curve as shown in Fig. 3-10(a).   The total light attenuation spectrum was calculated by adding signals at all angles between ±7.5^0 and ±22.5^0 together and shown in Fig. 3-11(d-f). The differences between these three curves and the sum of all curves in each graph in Fig. 3-9 (a-c) were calculated with data presented in Fig. 3-10(b) to derive the inversion of absorption spectrum of ICG. The results were presented in Fig. 3-11(g-i) for 0.05 wt%, 0.1 wt% and 0.5 wt% Intralipid^{TM} samples, respectively. All three curves were similar as expected, indicating the good repeatability of the measurement, and they were consistent with the corresponding curve in Fig. 3-10(a).
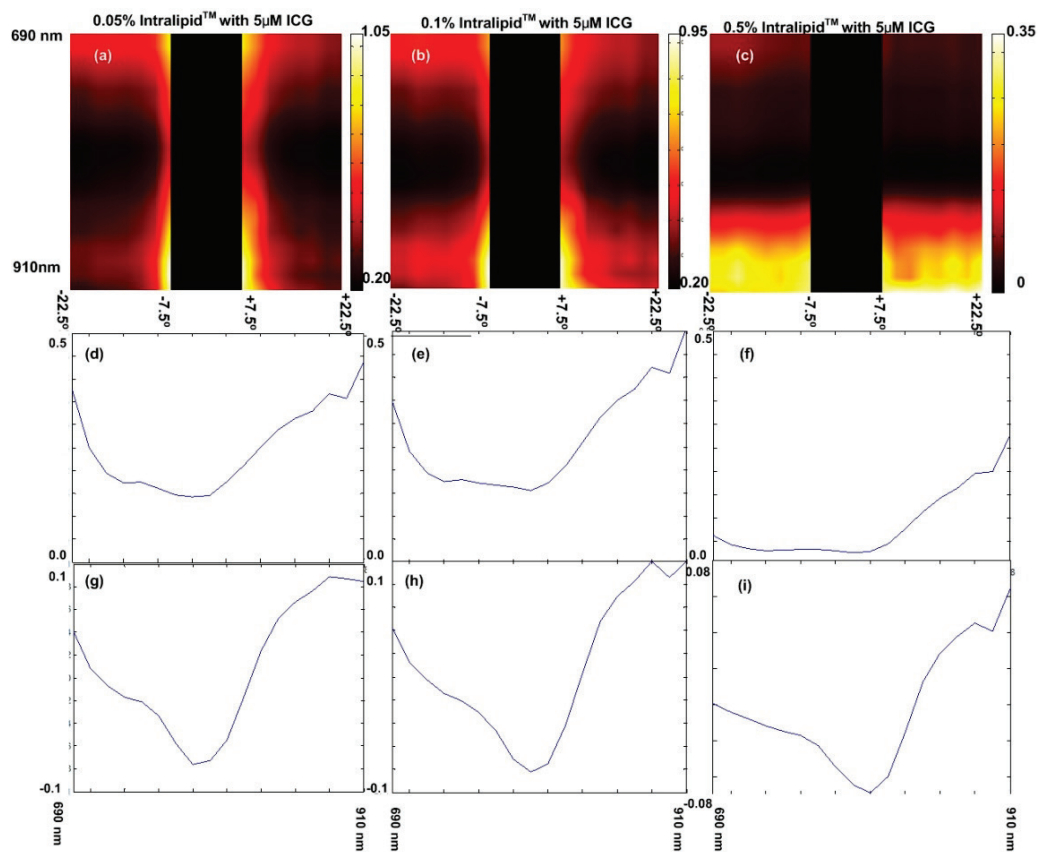
Fig. 3-11 (a-c) Measured BTDF across the spectrum between 690 nm and 910 nm for 0.05 wt%, 0.1 wt% and 0.5 wt% Intralipid^{TM} and 5 µM ICG solutions, respectively. (d-f) Calculated total light attenuation spectrum for the above three samples. (g-i) Calculated the inversion of ICG absorption spectrum.

3.5. Conclusion

Two design concepts, constant aspect ratio and constant acceptance angle, and two output coupling strategies, bending and no bending, were explored in this work to solve the issues associated with a previous RAFA design (as presented in Ref. [86]). The new RAFA designs included features such as improved bending structures, lower acceptance angles, and center channel blockage. The RAFAs were characterized by hyperspectral optical imaging and compared. Constant aspect ratio designs with mirror-bending structure and central channel blockage proved to have the best performance compared to other competing designs. With the best performing design, signal output

intensity range at different angles was reduced from a few of orders of magnitude (compared to the previous RAFA design) to within one order of magnitude while an angularly uniform input beam was measured. Simulations and experiments revealed that the output light distribution was well-collimated even 6 mm from the output of the device, which indicated that the inter-channel cross talk was minimal for the design. Please note that the characterization results for designs with a focal length of 5 mm were not presented in this chapter because their performance was identical to that of designs with a focal length of 7 mm and the later was easier to be implemented.

The RAFA was used to measure a series of Intralipid^{TM} dilutions and a series of mixed solutions between Intralipid^{TM} and ICG., and the results were consistent with the optical scatter properties of the Intralipid^{TM} and ICG. The measurements supported the idea that the optimized RAFA design was well-suited to real-time angle-resolved spectroscopic measurements of turbid media.

The results from this study guided us towards a device that had an angular detection range larger than ±20° and a resolution better than 5°. It had similar performance to what most goniometer-based systems offer; however, the RAFA device eliminated rotational scanning and the use of more than one detector. Furthermore, the single shot acquisition of the angular response was limited only by the exposure time of the camera. In addition, the RAFA offered a competitive advantage over low-coherence interferometry systems by enabling multispectral and hyperspectral measurements with simple instrumentation.

4. Use of a Radial Angular Filter Array to estimate the position of an optically attenuating object within a turbid medium

4.1. Background

The use of light in the optical regime, rather than x-rays or ultrasound, to characterize irregularities in human skin or organs enables spectroscopic measurement that can potentially improve diagnostic capabilities. However, unlike x-ray and ultrasound, pure optical imaging modalities typically provide poor depth discrimination beyond 0.5-1 mm. The high level of scatter in tissue represents a major challenge to overcome. A number of techniques have been devised to obtain depth-resolved optical images. At the macro-scale, approaches typically involve rotationally scanning either the sample or the detector and determining the depth of objects via reconstruction-based algorithms. For example, angular domain optical projection tomography with a parallel angular filter array has been shown capable of resolving absorbing and fluorescent features embedded inside turbid samples at the centimetre scale [68, 92].

At the micro-scale, different gating schemes have been proposed to separate photons emitted from targets from the noise due to scatter. Coherence gating, spatial gating and, time gating are three approaches. Coherence-gated imaging techniques discriminate against scattered light which tends to decorrelate with respect to ballistic light. Only objects at which the optical path difference between the reference beam and imaging beam is less than the coherence length are imaged [93, 94, 95, 96]. Confocal and two photons microscopies are examples of spatial gating techniques. The key feature is their ability to acquire in-focus images from selected depths via one or more apertures or translation of the specimen [97, 98]. Time-gating has been widely implemented with reflection geometry and backscattered photons. The depth information is typically reconstructed according to the time-of-flight as it directly relates to the length

of the optical path [99, 100, 101, 102]. Various techniques have been combined together to achieve better performance [93, 94].

Each of these techniques has certain advantages and disadvantages, which usually makes one technique preferred over another for a given application. For this work, we sought to extend the angular domain imaging approach by devising a technique to extract depth information without rotation of the sample or detector. Our approach was to utilize the focusing capability of a radial angular filter array to preferentially observe a specific point below the surface of a turbid medium.

4.2. Objective

The primary goal of this work was to develop a technique to measure the position, particularly depth, of an absorbing target inside a turbid medium utilizing an RAFA and a focused illumination beam. The second goal was to validate the technique by measuring the output of the RAFA for the target inside the scattering medium at a series of known locations. The third goal was to characterize the performance of the RAFA measurements across a range of background scattering levels.

4.3. Method

4.3.1. Selected RAFA design

RAFA employed had a channel acceptance angle of 0.23º, an angular resolution of 2.5º, a device width of 25 mm and a device length of 17 mm. The channel height was 60 µm. The focal point was 7 mm from the edge of the RAFA and in the plane of the device. The range of detection angles was limited to ±5º to ±35º (Fig. 3-1(a) and (c)). The center channel was blocked to reduce the dynamic range requirement of the detector, shorten the device length, and minimize the signal noise. A detailed analysis of this blocking feature has been described in previous work [103].

4.3.2. Experiment setup

Fig. 4-1 presents the top-view of the RAFA-based depth measurement system. The output of the laser (780 nm, PicoTA, Toptica Photonics AG, Munich, Germany) was focused at a pinhole, collimated by a lens ($f = 50$ mm, Edmund Optics, NJ), and spatially modulated by a slit into a line. The line of illumination was in the same plane as the RAFA. The beam then passed a neutral density filter ($OD = 0.6$, NT46-220, Edmund Optics) then was focused within an Intralipid™ solution contained in a 2 cm cuvette. The RAFA was placed on a 6 degree-of-freedom jig (Multi-Axis Platform, Thorlabs, NJ) at the exit of the cuvette. The focal point of the RAFA was 4.50 mm from the edge of the cuvette exit surface and it overlapped with the focal point of the illumination laser beam. Once photons passed through the RAFA, they were coupled into a line camera (TCE 1304; 8 µm x 200 µm pixel size; 3648 pixels; Mightex Systems, Toronto, ON) via two lenses ($f = 75$ mm, Edmund Optics). The integration time ranged from 1 second and 6.5 seconds depending on the conditions.
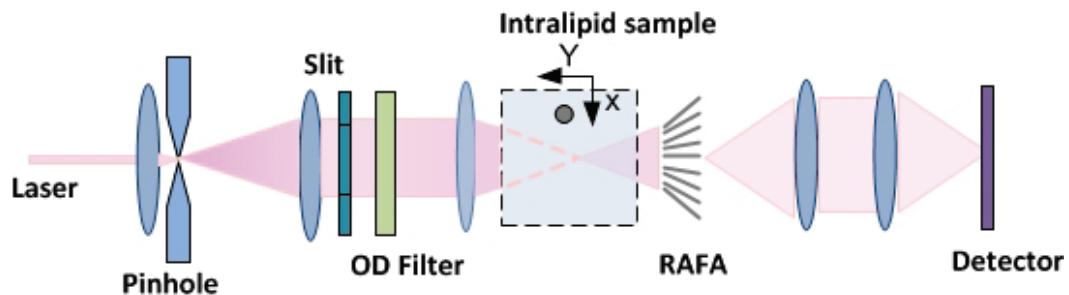
Fig. 4-1 Top-view of the RAFA-based apparatus for resolving the depth of embedded targets in a turbid medium. Figure adapted from reference [127].

4.3.3. Preparation of turbid media and their optical properties

Three Intralipid™ samples, 0.1 wt%, 0.3 wt% and 1.0 wt% were made by diluting the stock 20 wt% Intralipid™ with distilled-deionized water. The estimated reduced scattering coefficient for the 0.1 wt% solution was between 2 - 4 cm^{-1} and increased proportionally with concentration. The absorption coefficient for 10 wt% Intralipid™ diution was less than 0.001 cm^{-1} at 780 nm [48, 104]. Therefore, the attenuation of light in Intralipid™ solutions at 780 nm was expected to be primarily due to scattering.

Solutions with concentrations of 0.1 wt%, 0.3 wt% and 1.0 wt% were also tested with a 1 cm cuvette and a spectrophotometer (DU 640, Beckman). The results indicated that the reduced scattering coefficients at 780 nm were 3.5 cm^{-1}, 5.3 cm^{-1} and 6.0 cm^{-1}, respectively, which was consistent with the literature data presented above [73].

4.3.4.   Depth mapping

The first step of data processing was to normalize the raw measurement results to the background where the absorber was not present. The depth of the absorptive feature inside the turbid medium was extracted using a simple mapping algorithm as described conceptually in Fig. 4-2. The algorithm is used to obtain the depth of the feature via its transverse position x and the channel at which the target shadow appears.

As shown in Fig. 4-2, the mapping algorithm was developed based on the assumption that the RAFA was able to effectively select ballistic or quasi-ballistic photons at specific angles. In this case, the impact of the light absorber could be evaluated based on the ray optics. While the target was at the focal point, the entire RAFA would be in its shadow (Fig. 4-2(a)). If it was at the same *x* position as the focal point but at different depths (Fig. 4-2(b) and (c)), only some channels in the center would be covered by the shadow. While the target was at a location whose transverse position was different from the focal point (Fig. 4-2(d – g)), only the channel at a specific angle, *θ*, would be dark. Combined with its x position, the actual depth of the target inside the turbid medium could be determined by *θ* in this case.

Hee et al (1993) estimated that for reasonable powers of tissue irradiation in the infrared, the unscattered ballistic component could propagate through approximately 4 mm (2 mm tissue depth for reflection geometries) [105]. In our experiments, the focal point of RAFA was placed at 4.5 mm, slightly deeper than 4 mm, When the Intralipid^{TM} dilutions had similar optical properties as human tissues, the effective detection range would be constrained to a triangular area formed by the focal point and the overall aperture of the RAFA. The effective area of the setup was 14.2 mm^2, calculated from the RAFA angular detection range and the location of the focal point. In this effective detection range, each location could be uniquely represented by the transverse position, *x*, and the angle, *θ*, of the shadow.

In order to get the x position of the absorptive target, a parallel angular filter array could be employed as shown in our previous work [68]. An alternative method is to scan the Intralipid™ dilution including the target until the shadow of the target is observed at the center of the RAFA output. The position of the target could then be deduced by knowledge of the location of the RAFA focal point within the medium.
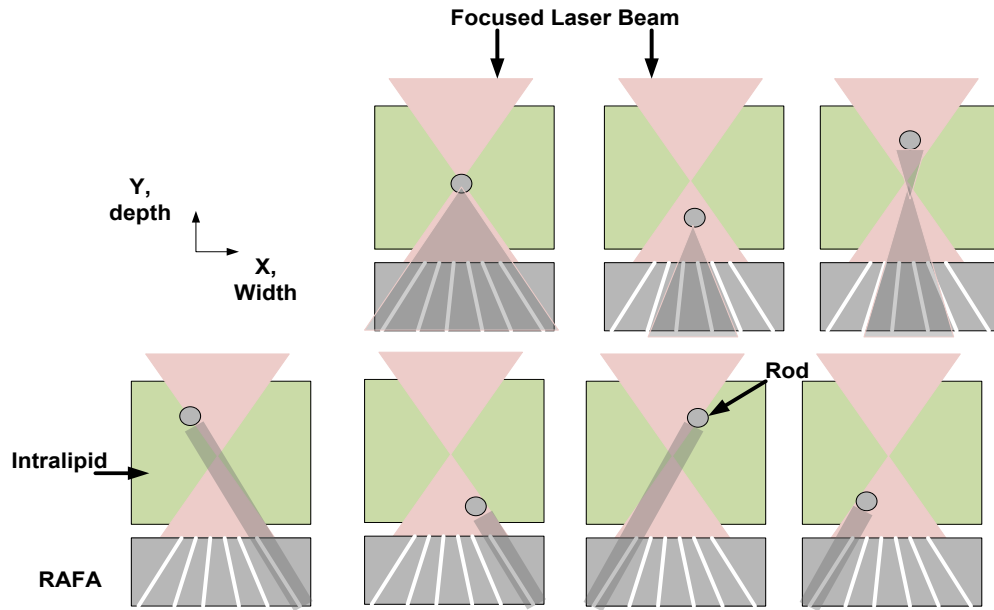
Fig. 4-2 Conceptual overview of the method for detecting the position of an absorber in a turbid medium using a RAFA. Figure adapted from reference [127]. The series of panels (a-g) show the relationship between the output of the channels (as shown with bright and shadowed channels) due to the absorbing rod and the rod position for different situations.

4.3.5. Measurement system validation

To validate the measurement system, a graphite rod of 0.5 mm in diameter was placed into the Intralipid™ dilution as the absorber. Its position was controlled by high precision linear stages (ILS250PP, Newport, CA) and the rod could be scanned in the transverse direction x and longitudinal direction y with a scanning step as small as 0.01 mm (Fig. 4-1). For our experiments we used scanning step sizes in the *x* and *y* directions of 0.2 mm and 0.25 mm, and the total scanning distance was 4.8 mm and 6.25 mm, respectively. The RAFA-measured rod depth was compared to the actual value to obtain the accuracy.

4.4. Results and discussion

The angular light distribution at each scanning step was collected and the ensemble was assembled into a data cube as presented in Fig. 4-3. In the data cube, the *x* axis represented the transverse direction and *y* axis represented the scanning direction in depth (longitudinal direction). The *z* axis represented the angle, *θ*. Fig. 4-3 shows a pair of 2D intensity maps specific to the output of a channel at either -22.5° (i.e. left of the focal point; Fig. 4-3(a)) or 22.5° (i.e. right of the focal point; Fig. 4-3). In both cases, a line shadow was observed as hypothesized from inspection of Fig. 4-2(f) and (d). The fidelity of the shadow suggested that light captured by the RAFA was mainly ballistic and quasi-ballistic and ray optic rules were applicable. In addition, the shadow became darker and the boundary was sharper as the rod approached the front surface of the cuvette. The effect was due to the combination of the following two reasons: i) at the location which was close to the channel entrance, the circumferential distance represented by the angle of acceptance was smaller than at larger distances from the RAFA. Therefore, close objects are darker than far objects due to less light passing either side of the object; ii) Lower noise was expected due to less scattering as the distance between the rod and RAFA was reduced.

According to Fig. 4-2, the crossing point of all line shadows should be the focal point of RAFA. This was validated in Fig. 4-4 in which the center lines of the shadows of all angles were drawn for 0.1 wt% Intralipid^{TM}. All lines, except one due to the experimental error, converged upon the same point as hypothesized. The coordinate of this point was (3.6, 4.5), which matched the actual location of the focal point. Furthermore, at the left side of the focal point, shadow center lines were aligned in sequence, from -35° to +35°, as hypothesized based on inspection of Fig. 4-2(d-g). This phenomenon confirmed that the RAFA could successfully pick up the ballistic and quasi-ballistic photons out of the scattered ones and the selected photons followed geometrical optics rules. As a result, a 1:1 correlation between the target depth and [*x, θ*] values was established within the effective detection area of the RAFA. In addition, the size of the measured focal point was around 0.4 mm in width and 0.4 mm in depth. The height was around 60 μm, consistent with the height of the RAFA channels. In short, the focal point was estimated to be 0.0096 mm^3 in volume. As the rod moved deeper inside the

Intralipid^{TM} solution, the overall scattering increased and the alignment of shadow center lines started to corrupt at locations deeper than the focal point and the mapping relationship began to breakdown.

(a)   (b)
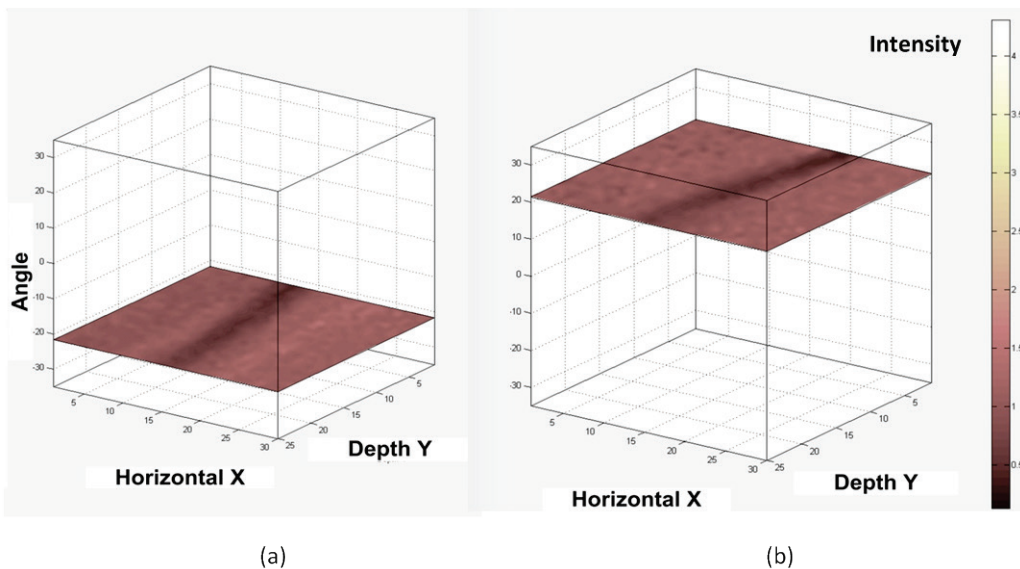
Fig. 4-3 (a) Measured 2D intensity map at -22.5°. (b) Measured 2D intensity 2D at + 22.5°. Figure adapted from reference [127].

The same analysis was performed with 0.3 wt% Intralipid^{TM} dilution as shown in Fig. 4-5. The focal point estimated with RAFA measurements had the same coordinate value as determined for the 0.1 wt% Intralipid^{TM} dilution, which also compared well with the actual value known from the position of the linear slides. The 2D shadow center line map was also consistent with the concepts shown in Fig. 4-2. However, the corruption of the shadow center line map occurred closer to the surface compared to the map obtained with the 0.1 wt% Intralipid^{TM} dilution. With 1.0 wt%, the corruption occurred at a depth of 1 mm and beyond (Fig. 4-6). In this case, the focal point could not be resolved. The depth detection limits for Intralipid^{TM} at 0.1 wt%, 0.3 wt%, and 1.0 wt% were 6 mm, 3.75 mm, and 1 mm, respectively.
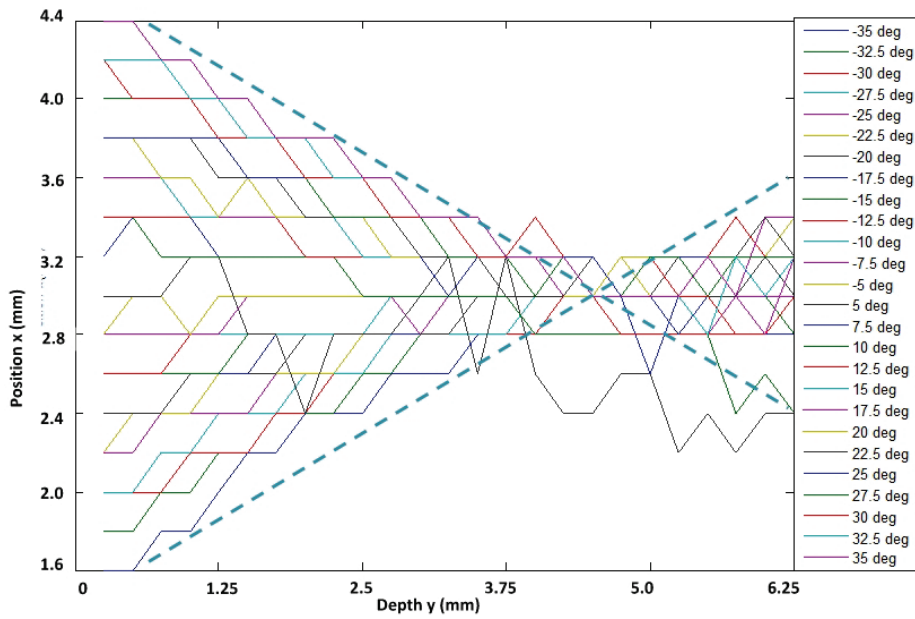
Fig. 4-4 2D shadow center line map for 0.1 wt% Intralipid^{TM}. Figure adapted from reference [127].
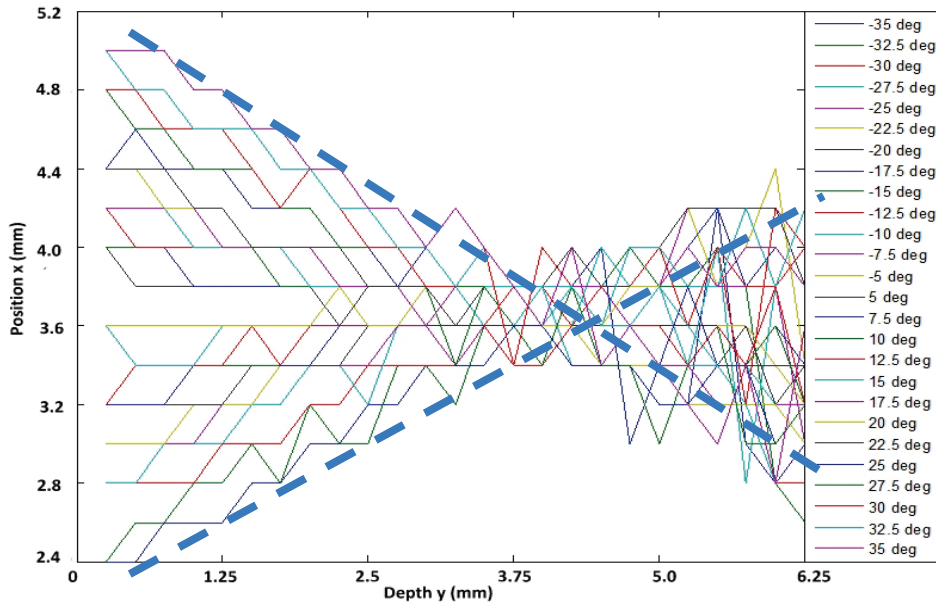
Fig. 4-5 2D shadow center line map for 0.3 wt% Intralipid^{TM}. Figure adapted from reference [127].
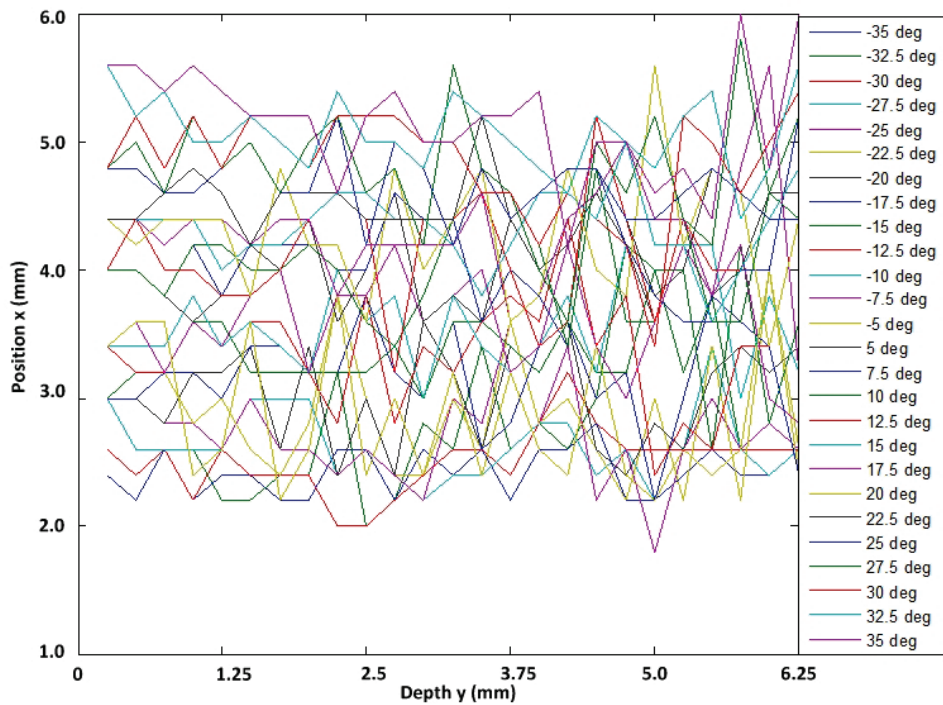
Fig. 4-6 2D shadow center line map for 1.0 wt% Intralipid^{TM}. Figure adapted from reference [127].

4.5. Conclusion

We described a method to measure the depth of absorptive features inside a turbid medium with a RAFA. This approach was validated by scanning a graphite rod in Intralipid^{TM} dilutions at different Intralipid^{TM} concentrations with a focused illumination beam. At each scan step the light distribution at the output of the RAFA was measured. We mapped the shadow due to the existence of the rod and compared them with the shadow expected based on a conceptual model. The measured coordinate of rod at the focal point of the device was similar to the actual value. The depth detection limits for different Intralipid^{TM} concentrations were also measured and found to decrease with increasing scatter. This experiment also revealed the effective size of the focal point of RAFA. Although the system was designed to work with a focused laser beam, it is expected to work with a collimated broadband beam, which could simplify the experimental setup and enable spectral analysis.

5. Angle-resolved spectroscopy: a tissue-mimicking phantom study

5.1. Angle-resolved spectroscopy

Angle-resolved spectroscopy is an optical sensing technique that is capable of discriminating the angular-dependent spectral information of a target at or near the surface of a sample. The resultant data can be presented as a two-dimensional map, which reveals the spectral absorption properties of a target along the wavelength axis and the scattering properties along the angle axis. The combination of these two measures is useful for detection of micro-topographic irregularities of a surface and may have applications in cancer detection.

As stated in section 1.2.2 and 1.2.3, a goniometer-based setup is commonly used for macro-scale angle-resolved spectroscopic analysis, in which either the sample or the spectrometer is rotationally scanned to collect information over a range of angles [17, 19, 20]. In order to reduce the read-out time due to scanning, multiple detector heads at different angles have been employed. However, the setup becomes more complex and bulky. With micro-scale applications, low coherence interferometry combined with light-scattering spectroscopy has been successfully implemented to characterize tissue morphology. As an example, an endoscope with a drum lens and fiber optic bundle could separate photons at different angles into different fibers to generate the scattering profile for targets close to the tissue surface [81, 106]. Researchers have also tried to capture angle-resolved spectroscopic data via scanning the area around the illumination beam to measure diffusively back-scattered photons [83, 84].

5.2. Objective

The goal of the work was to evaluate whether an RAFA-based hyperspectral system could capture angle-resolved spectroscopic information of objects embedded inside turbid samples, particularly biological samples. Our approach was to conduct angularly-resolved spectroscopic measurements using an RAFA with a collimated broad band illumination beam and a spectral imager for targets embedded in a tissue-mimicking phantom. Spherical targets were constructed from Indocyanine Green (ICG) and embedded at three depths within an optically scattering gel (containing Intralipid^{TM}).

5.3. Method

5.3.1. Preparation of tissue mimicking phantoms

The tissue-mimicking phantom contained homogenous spherical targets at three different depths. The targets were fabricated by casting a mixture of ICG, Intralipid™ and agarose into a plastic mold and were subsequently embedded into a background gel material, formed from a mixture of Intralipid™ and agarose. The first step to prepare targets was to dissolve agarose (A-6013, Sigma Chemical Co., St Louis, MO) powder into a phosphate-buffered saline (PBS) solution. Indocyanine Green (I2633-25MG, Sigma Chemical Co., St Louis, MO) and Intralipid™ were then added to achieve a final concentration of 10 µM and 0.1 wt%, respectively and the final concentration of agarose was 1.0 wt%. The solution was then maintained at 50°C in a water bath to prevent the solidification to a gel (32-40^{0}C) before injection into the mold. Once ready, the mixture was injected into the mold using a 25AWG needle. After the targets hardened, a separately prepared background mixture of 2.0 wt% agarose and 0.1 wt% Intralipid™ was poured into the phantom mold around the targets to create the body of the phantom. The phantom was left to harden at room temperature. The overflow of the gel was trimmed prior to removing the phantom from the mold.

The structure of the phantom is presented in Fig. 5-1. The radius of each sphere-shaped target was 1.5 mm. Each phantom contained 3 groups of targets with 2 targets in each group. The distances from the front surface of the targets in different groups to

the surface of the phantom at which light exited were 1 mm, 2 mm, and 3 mm, respectively.
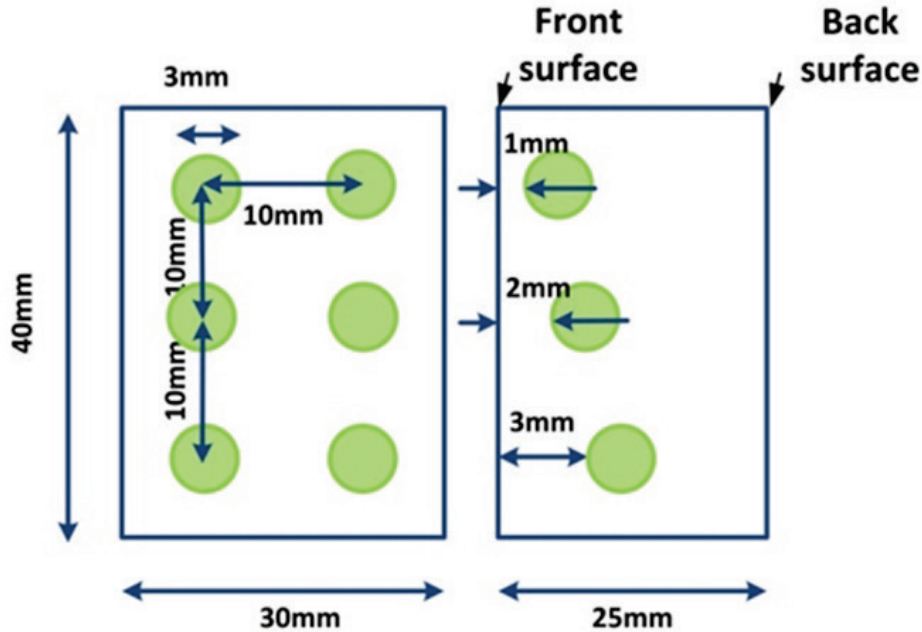
Fig. 5-1 Front and side views of the phantom showing the location of the targets relative to the surface. Figure adapted from reference [44]

5.3.2. Optical properties of tissue mimicking phantoms

The Intralipid™/agarose gel offers similar absorption and scattering properties as human skin. The attenuation of light in the phantom in near infrared (NIR) band was expected to be primarily due to scattering [42, 107, 108, 109]. The absorption coefficient of Intralipid™ was estimated to be on the order of $10^{-4} \sim 10^{-5}$ cm^{-1} (between 600 nm and 950 nm) [48, 104]. Using the same reference sources, the equivalent reduced scattering coefficient of 0.1 wt% Intralipid™ was calculated to be on the order of 1~6 cm^{-1} [48, 104]. Thus, the total attenuation of a gel with 0.1 wt% Intralipid™ and 1.0 wt% agarose was confirmed to be dominated by scattering. Intralipid™ solutions with 1 cm optical path were also measured with a spectrophotometer (Beckman DU 640). The results indicated that the reduced scattering coefficients between 600 nm and 900 nm were approximately 2.0 ~ 5.0 cm^{-1}, consistent with calculated and published values above [73]. Secondly, the scattering in human skin was forward-oriented and it was in agreement

91

with that in IntralipidTM phantom. For Intralipid™, it has been reported that the weighted scattering phase function (g) is 0.75 ± 0.18 [48, 104] .

The total attenuation of 10 µM ICG in 1% agarose gel after 1 cm optical path was measured as well. The peak absorption was observed at ~ 780 nm and strong absorption was observed between 650 nm and 820 nm. At the peak, the total attenuation coefficient was about 4.6 cm^{-1} [73]. This result was consistent with the literature data as shown in [90]. The total light attenuation due to the targets embedded within the phantom was expected to be a combination of attenuation due to the ICG and Intralipid™.

5.3.3.   Selected RAFA design

The RAFA had a channel acceptance angle of 0.46º, angular resolution of 2.5º, device width of 25 mm, and device length of 17 mm. The focal point was 7 mm away from the edge of the device. The detection angle was -35º ~ -7.5º and 7.5º ~ 35º. The center channel was blocked for multiple reasons, including reducing the dynamic range requirement of the detector, shortening the device length and minimizing the signal noise. These reasons have been detailed in [89, 103]. A bending section in each channel re-directed the propagation of photons toward a direction normal to the output edge of the device. The channel walls in the pre-bending section were patterned with vertical ridges to effectively trap photons travelling beyond the acceptance angle (Fig. 3-1(b)). The bending section and post-bending section were coated with a thin aluminum layer (500 - 600 nm) (Fig. 3-1(d)).

5.3.4.   Experiment setup

Fig. 5-2 presents the top-view of the hyperspectral analysis system. The output of a quartz tungsten halogen lamp (Oriel, Series Q Lamp Housing, 100W) was spectrally filtered by a high pass filter (645 nm, part no. 65.1365, Rolyn Optics Co., Covina, CA) then a near infrared short pass filter (950nm, 950FL07-50S, LOT-Oriel GmbH, Germany). After that, the beam was focused at a pinhole. A holographic diffuser was used to homogenize light reaching the pinhole. The light from the pinhole was collimated by a NIR doublet spherical lens (ACH-NIR 25×50, Edmund Optics) with a focal length of 50

mm. The beam passed through the Intralipid^{TM} phantom and reached the RAFA held by a 6 degree-of-freedom jig (Multi-Axis Platform, Thorlabs, NJ). The focal point of the RAFA set to 5 mm inside the phantom as measured from the phantom surface closest to the RAFA. The relationship between the focal point and the locations of targets were shown in Fig. 5-3. The phantom was positioned on a high precision control stage (ILS250PP, Newport, CA). During each experiment, the stage was shifted along the longitude axis of the phantom and five measurements were taken at 5 mm intervals. The output of the RAFA was directly coupled into the optics of an imaging spectrometer (P&P Optica Inc., Kitchener, Canada; imaging sensor: C10151-S10141-1109, Hamamatsu Photonics K.K. Japan), which was introduced in Section 3.2.2. The corresponding spectral resolution was also 3 nm and the integration time ranged from 1 to 3 seconds.
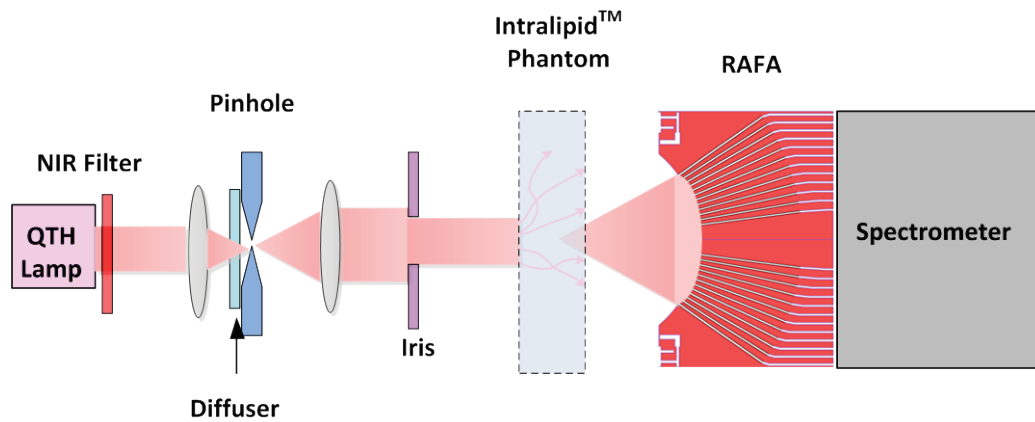
Fig. 5-2 Top-view of the apparatus for RAFA phantom study setup. Figure adapted from reference. Figure adapted from reference [128].
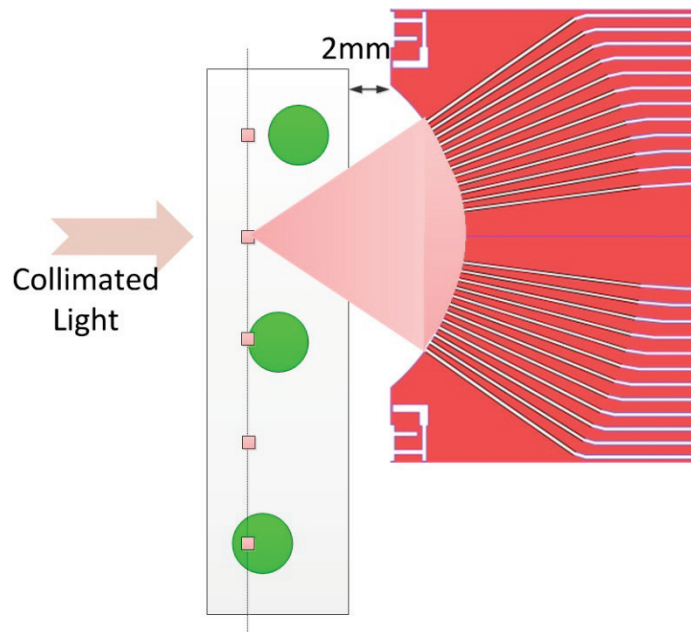
Fig. 5-3 The focal point location of RAFA in the experiment. Figure adapted from reference. Figure adapted from reference [128].

5.4. Results and discussion

5.4.1. Measured angle-resolved spectroscopy

Raw angle-resolved spectroscopic data for five measurement points were calibrated according to the device and setup signatures as explained in [89, 103]. Fig. 5-4(a) and (b) shows the calibrated results at two locations where no features were present. In these two images, the light intensity increased gradually from 690 nm to 895 nm at each angle. The pattern of response was consistent with the fact that the absorption gradually decreased from short wavelengths to longer wavelengths (Fig. 3-10). Further analysis was performed in Fig. 5-4(c-d), in which the intensities across all angles at each wavelength were normalized to the peak value at each wavelength. The results were consistent with the hypothesis that scattering decreased from short wavelengths to the long wavelengths. In addition, differences between Fig. 5-4(a)/(c) and (b)/(d) were not measureable, which indicated that the body of the phantom was homogenous.
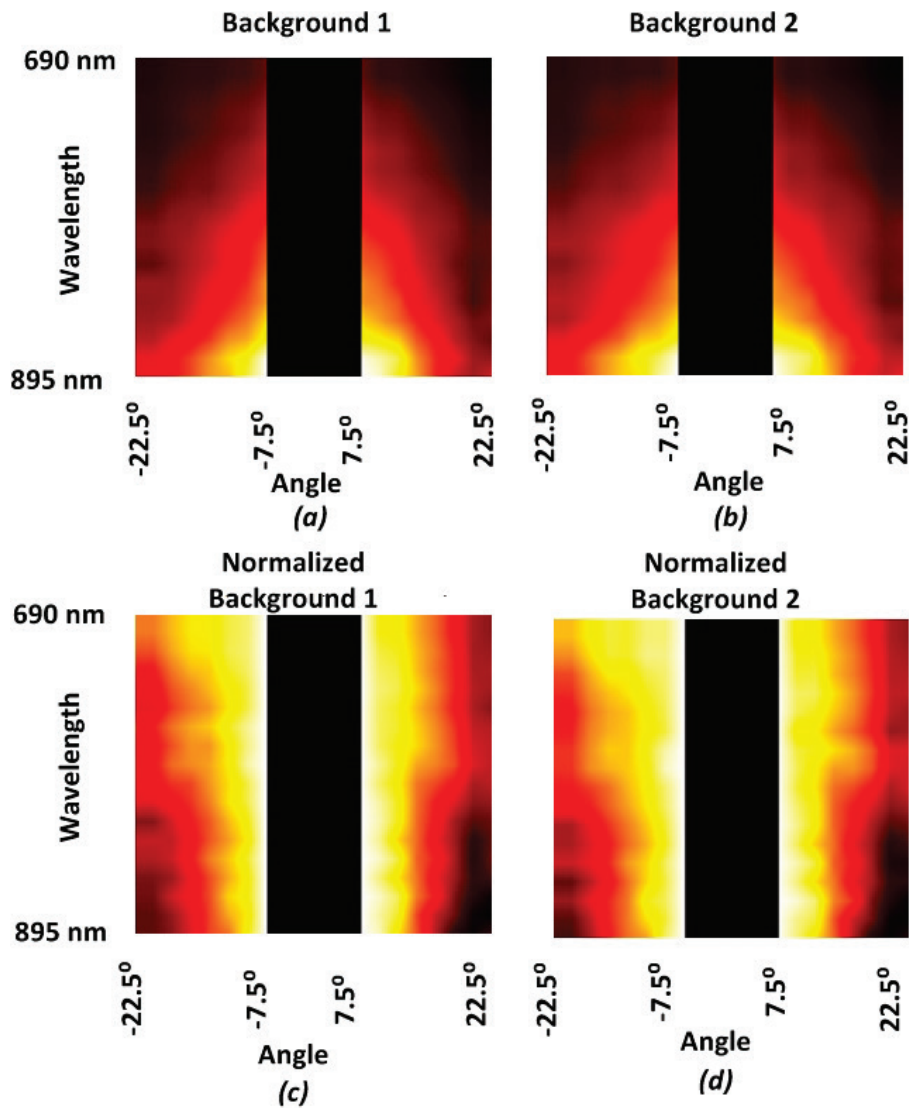
Fig. 5-4 (a) Angle-resolved spectroscopic measurements of background between the 1 mm and 2 mm deep targets. (b) Angle-resolved spectroscopic measurements of background between the 2 mm and 3 mm deep targets. (c) Normalized angle-resolved spectroscopic measurements from (a). (d) Normalized angle-resolved spectroscopic measurements from (b). Figure adapted from reference [128].

Angle-resolved spectroscopic data of targets at different depths were obtained by subtracting background information from the raw data. Fig. 5-5(a-c) presented results at 3 mm depth, 2 mm depth and 1 mm depth, respectively. An absorption band was clearly visible in all three cases, particular in the last two and the location of the band matched well with the absorption peak of ICG (Fig. 3-10). The normalization process used to

95

generate Fig. 5-4(c-d) was conducted to result in data in Fig. 5-5(d-f). The normalized scattering profiles at all three locations (Fig. 5-5(d-f)) were similar to that of the phantom background. This result was expected as the target had the same Intralipid^{TM} concentration as the background and the ICG was expected to only affect the absorption property. Analysis above demonstrated that the angle-resolved spectroscopy obtained from a RAFA based measurement system could successfully measure the scattering properties of a turbid sample even if the sample contained absorptive features.
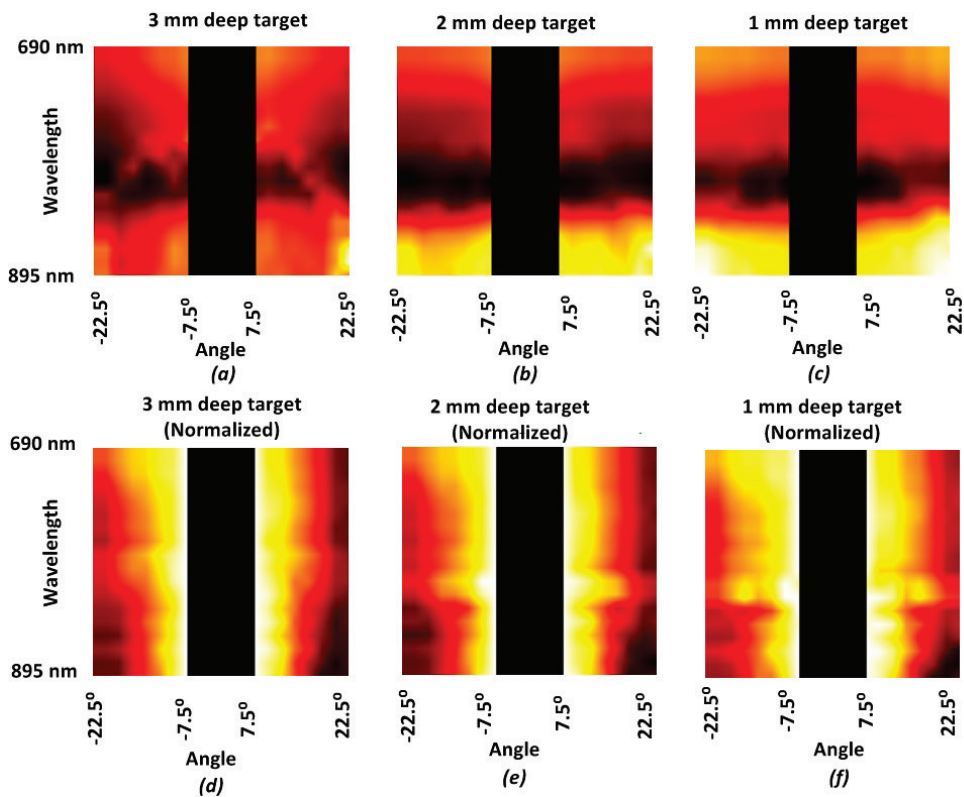
***Fig. 5-5 (a) Measured angle-resolved spectroscopy for target at 3 mm depth. (b)
Measured angle-resolved spectroscopy for target at 2 mm depth. (c)
Measured angle-resolved spectroscopy for target at 1 mm depth. (d)
Normalized angle-resolved spectroscopy for target at 3 mm depth.
(e) Normalized angle-resolved spectroscopy for target at 2 mm
depth. (f) Normalized angle-resolved spectroscopy for target at 1
mm depth. Figure adapted from reference [128].***

5.4.2.   Absorption spectra analysis

Besides measuring the scattering properties of a heterogeneous turbid sample, the other goal to develop RAFA based angle-resolved spectroscopy system was to extract the absorptive information of the targets inside a turbid medium. Fig. 5-5(a-c) indicated that the proposed characterization system was able to capture ICG absorption spectrum. However, it was unclear why the absorption of 3 mm deep targets was less significant than the other two and whether the shape of the curve was consistent with the data presented in [88, 90].

According to section 5.3.2, the scattering in the Intralipid^{TM} phantom was forward-oriented. Chapter 4 of this thesis presented that RAFA was able to collect the photons passing through the focal point primarily. Thus, it was reasonable to assume that the photons intended to be collected were those who travelled along the incident collimation direction first and then scattered at the RAFA focal point. In this case, the ratio between the absorptive optical paths (inside the ICG targets) and the non-absorptive optical paths (outside the ICG targets) would determine the shape of the measured spectra. Furthermore, noise would be introduced along the optical path after the scattering event outside the ICG target. Fig. 5-6(a-c) explained the relative position between the RAFA focal point and the spherical targets at different depths. Fig. 5-6(d-f) presented the obtained normalized total light intensities at RAFA output and the intensities at 10 degree channel and 20 degree channel for all three locations, respectively. The normalization in Fig. 5-6(d-f) was performed in two steps. At the first step, the background light intensity obtained from the area without the target was subtracted from the measurement results. Then the values were normalized in regards to the minimum value of that channel (Fig. 5-6(e-f)) or all channels (Fig. 5-6(d)).

Fig. 5-6(d-f) revealed that the absorption of 3 mm deep targets was less distinct than the other two. Higher background noise variations were believed as the root cause since the optical path starting from the focal point, where the scattering occurred, but outside the 3 mm deep target was longer than the other two cases (Fig. 5-6(a-c)). On the other side, the measured absorptive spectra of 1 mm and 2 mm targets were consistent with the expected ICG absorptive spectrum as shown in Fig. 3-10(a). Furthermore, the results obtained from the center channel (10 degree) (Fig. 5-6(f)) were better than those from the side channel (20 degree) (Fig. 5-6(e)) or the averaged results (Fig. 5-6(d)). The primary reason was that the ratio between the absorptive and non-absorptive optical paths of the photons entering the center channel was larger than that of the photons entering the side channels (Fig. 5-6(a-c)). Above all, results presented in Fig. 5-6 confirmed that RAFA based angle-resolved spectroscopy system was able to identify an absorptive target inside a turbid medium via angular spectroscopic analysis.

98
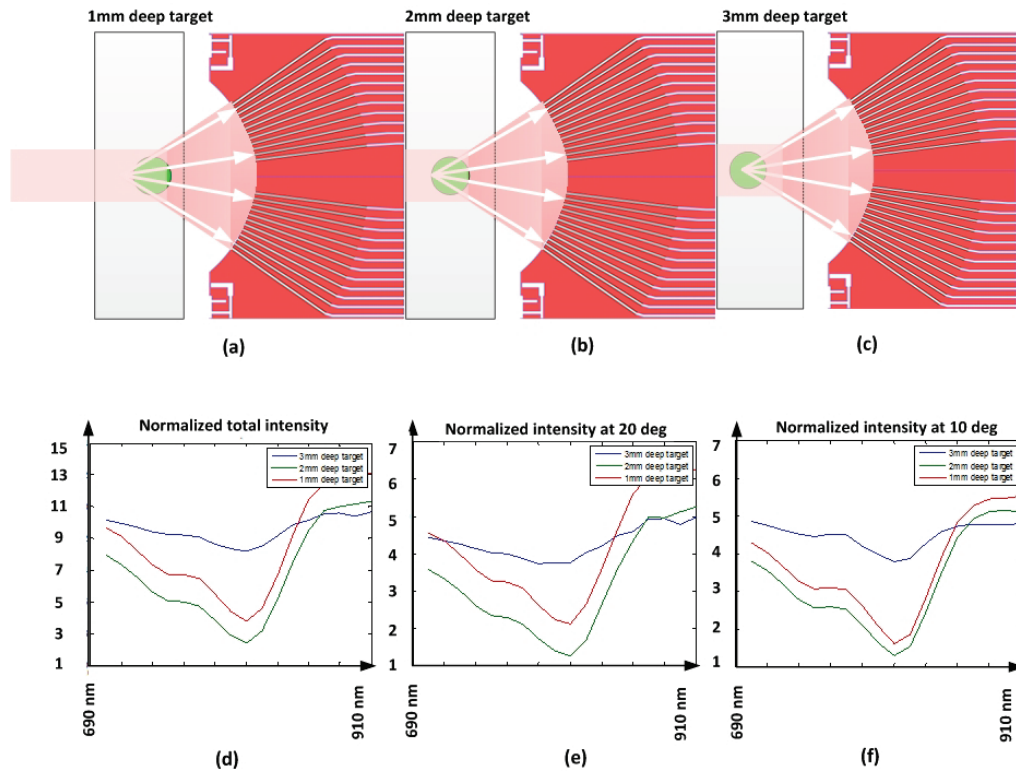
Fig. 5-6 (a -c) Diagrams describe the relative position between the focal point of RAFA and spherical targets at 1 mm, 2 mm and 3 mm depth, respectively. (d) Normalized total intensity of RAFA channel outputs of 1 mm, 2 mm and 3 mm deep targets from 690 nm to 910 nm. (e) Normalized intensity of 20 deg RAFA channel outputs of 1 mm, 2 mm and 3 mm deep targets from 690 nm to 910 nm. (f) Normalized intensity of 10 deg RAFA channel outputs of 1 mm, 2 mm and 3 mm deep targets from 690 nm to 910 nm. Figure adapted from reference [128].

5.5. Conclusion

This chapter confirmed that angle-resolved spectroscopy of a tissue-mimicking phantom and the absorptive features embedded could be performed with an RAFA-based hyperspectral system. The setup did not require mechanical scanning to resolve angular information, was easy to align, and utilized an integration time of less than 3 seconds. Hyperspectral analysis revealed that this approach could successfully identify the scattering and absorption properties of the embedded targets inside the phantom at the same time. The focal point of the RAFA was 5 mm deep inside a 0.1% wt Intralipid^{TM} phantom and the obtained angle-resolved spectroscopy with a collimated illumination beam was affected by the depth of the embedded target. Future work could examine the detection depth at higher Intralipid^{TM} concentrations and explore the spatial resolution and angular resolution of the technique.

6. Use of radial angular filter array to estimate the far-field angular transmission intensity of a nano-hole array

6.1. Background and objective

6.1.1. Review of RAFA applications

From chapter 3 to 5, RAFAs were implemented to characterize a series of turbid media, including detecting the variations in scattering level, verifying the existence of an embedded absorber via angular spectroscopic analysis and identifying its physical location. A typical RAFA has a dimension of 2.0 x 2.5 cm with an angular coverage over 60° and it was proved to be able to simplify the conventional goniometer setup or multi-detector array setup for macro-scale angle-resolved scattering measurement [19, 78] as it did not require to rotate either the sample or the detector, and only use one set of an RAFA and a detector. In micro-scale, RAFA expected to provide an alternative solution to approaches like low-coherence interferometry and scanning near-field optical microscope (SNOM) [25, 26, 78, 111]. It could potentially increase the angular coverage, provide hyper-spectral analysis capability, and improve the data acquisition speed.

The next step in RAFA development focused on further characterizing the RAFA based angular spectral measurement system with samples that have higher spectral variations compared to turbid samples used in previous projects, improving RAFA design to reduce the variations in signal loss between channels at different angles and exploring new applications like understanding the relationship between tissue/cell structures and light scattering from tissue [110], surface topography analysis, particle counting, defects detection and machine vision.

6.1.2. Nano-Hole Array (NHA)

RAFA could potentially help to characterize the optical excitation of surface plasmons (SPs) as it supports both spectral and angular measurements simultaneously. The unique optical properties of sub-wavelength plasmonic structures have opened up new possibilities for creating and enhancing many photonic applications such as surface enhanced Raman spectroscopy (SERS) and Surface Plasmon Resonance (SPR) sensing [112, 113, 114]. Devices like SPR sensors employ several different methods of optical excitation of SPs, including attenuated total reflection (prism coupling) and diffraction on periodic metallic gratings (grating coupling) [115, 116]. Particularly, at the surface of a sub-wavelength hole array in a metallic film, light within a narrow spectral range can couple with SPs, giving rise to Extraordinary Optical Transmission (EOT) [117, 118, 119]. The EOT properties are highly dependent on the near-surface dielectric constant and have motivated the development of nano-hole arrays (NHAs) for molecular sensing and spectroscopic applications [120, 121].

The EOT is dependent on the geometry, composition, and excitation angle (the incident angle of the illumination beam) of the NHA [119, 121, 122]. It has been reported that far-field angular transmission intensity maps provide discrimination of EOT spectral features across illumination angles [117, 118, 119, 121, 123, 124]. NHA-based sensing systems that utilize such intensity maps could exploit both the angular and spectral information and therefore offer superior performance to conventional sensing systems where only spectral information is used. The existing measurement techniques for obtaining angular transmission intensity maps employ angular scanning of the NHA, the incident beam, or the detector [123, 124, 125]. The presence of a scanning process considerably slows the data acquisition speed. For real-time NHA-based sensing applications, a method capable of measuring transmission over a range of angles simultaneously is required. The integration of RAFA with NHAs will facilitate the development of portable Surface Plasmon Resonance (SPR) sensing devices.

6.1.3. Objective

This chapter presents a real-time method for measuring the far-field angular transmission intensity map of a NHA with RAFA. It demonstrated the capability of RAFA

based angular-spectroscopic measurement system to characterize devices with high spectral variations across a wide angular range. The results were further compared to conventional measurements obtained with a microscope setup and to simulations obtained with a Finite Difference Time Domain (FDTD) method. The comparison results would validate the potential to develop a RAFA and NHA based real-time angular-spectroscopic characterization device.

6.2. Experiment setup

6.2.1. Nano hole array preparation

A NHA (Fig. 6-1) was fabricated via electron beam lithography in a 100-nm optically thick gold film on a Pyrex substrate (see [126]). The 2D array covered an area of 50 μm by 50 μm. It consisted of a matrix of round holes, where the hole diameter was 287 ± 20 nm, and the spatial period between holes was 440 ± 20 nm. During fabrication, a 3-nm thin conductive layer of titanium was deposited on the Pyrex substrate for electron beam writing and a 10-nm thin titanium layer was deposited to facilitate adhesion of the gold layer. In the vicinity of the holes, the titanium layers were etched to improve transmission [126].
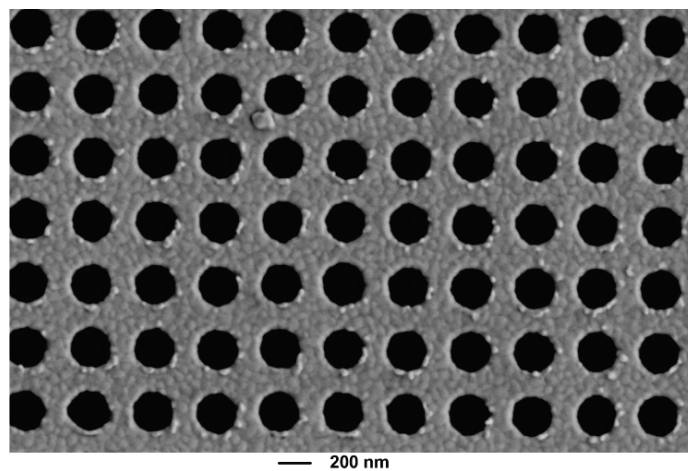
Fig. 6-1 NHA studied in the project

6.2.2. RAFA selection

Details of the RAFA design and fabrication steps have been presented in chapter 2 and 3. Two RAFA devices were used in the experiments and they were design 5 and 6 in Table 2-2. Each RAFA had a constant micro-channel aspect ratio and a focal length of 7 mm. The first device had an acceptance angle of ~0.68°. The corresponding width and height of each channel was 120 µm and 60 µm, respectively. Both the width and height were significantly larger than the wavelength of light to minimize diffraction effects. The angular resolution was 2.5°, and the device width was 25 mm. The detection angle range was [-35° ~ -7.5°] and [7.5° ~ 35°]. A second RAFA with the same acceptance angle, dimensions and focal length was used to cover the detection angles within ±7.5°. Used in sequence, the two RAFAs provided greater angular coverage than either RAFA alone.

6.2.3. Microscope setup

The NHA sample was characterized by a reference microscope setup (Fig. 6-2(a)) as described in ref [126]. Briefly, an inverted microscope (Nikon, TE300) was connected to a photometer (PTI, D104), monochromator (600 nm ~ 900 nm, PTI, 101), and photomultiplier tube detector (PTI, 710). Unpolarized white light from a 100W QTH lamp (Oriel, Series Q, 100W) was focused on to the sample from the air-gold side using the bright-field condenser lens ($f = 60\ mm$). A ring aperture was placed in front of the condenser lens and resulted in a cone of light with an angle dictated by the ring diameter projected onto the sample (Fig. 6-2(a)). The cone angles were 0°, 2.4°, 4.8°, and 11.8°. The transmitted light was collected by a 20x objective ($NA=0.45$; Nikon, 93150). For each NHA, optical transmission spectra were collected from the region containing the NHA (sample) and a hole-free region (background). The background and lamp properties were accounted for by subtracting the background spectrum from the sample spectrum and then dividing the result by the measured white light spectrum (collected with the Pyrex substrate in front of the objective).

6.2.4. RAFA setup

The RAFA setup is shown in Fig. 6-2(b). Specifically, white light from the same QTH 100W lamp was spectrally filtered by a pair of filters: a high pass filter (645 nm, #65.1365, Rolyn Optics), and a near infrared short wave pass filter (950nm, # 950FL07-50S, LOT-Oriel GmbH). The beam was then homogenized and collimated via the same optics described in Ref [1]. Subsequently, the beam was focused by the same objective lens employed in the microscope setup onto the NHA. Transmitted light was collected by the RAFA held by a 6 degree-of-freedom jig (Multi-Axis Platform, Thorlabs) that enabled the focal point of the RAFA to be positioned on the back surface of the NHA, and alignment of the RAFA with the beam direction and the slit of the imaging spectrometer (P&P Optica Inc., CCD sensor from Hamamatsu Photonics: C10151-S10141-1109, 2048 × 506 active pixels, 650 nm - 950 nm, 12 μm×12 μm pixel size, 0.6 nm spectral resolution). The effective spectral resolution of the imaging spectrometer was limited by the dispersion due to the height of the RAFA micro-channels. The calculated spectral resolution was ~ 3 nm (Section 3.2.2). With this setup, the zero order transmission spectrum for each incident angle could be captured by the corresponding channel in RAFA. As the result, both the angular and spectral distributions of light at the focal point of the RAFA could be characterized without mechanical scanning or rotation. The camera readout time was ~ 3 seconds. In a manner similar to the microscope measurements, the background, lamp signature, and RAFA device signature were removed by subtracting the sample spectrum from the background spectrum at each angle.
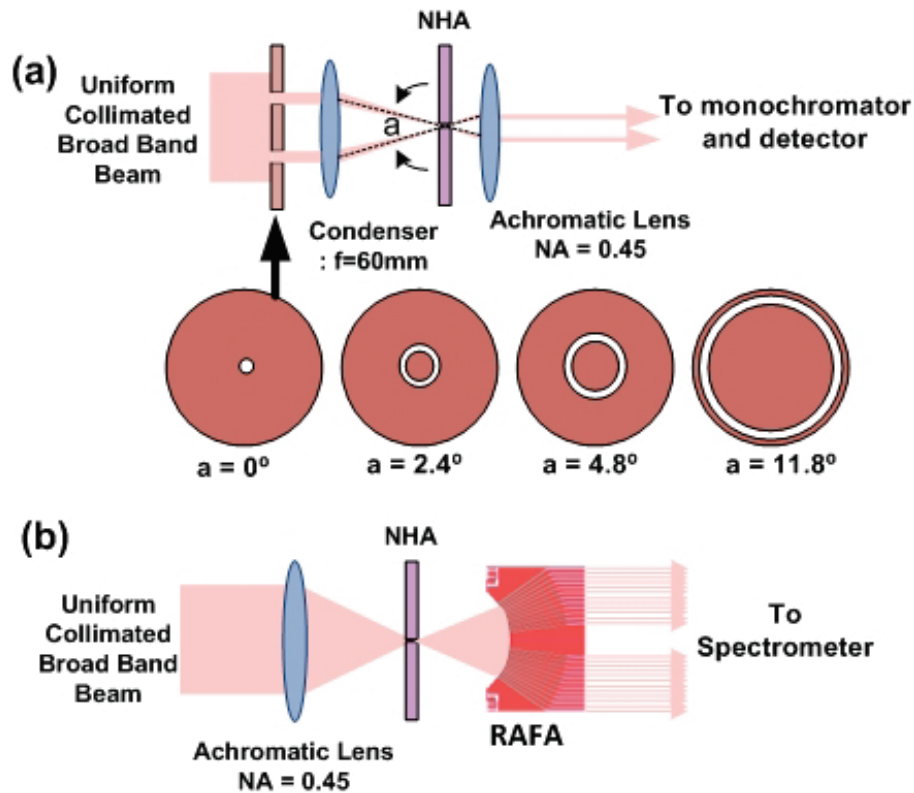
Fig. 6-2 (a) Microscope setup; (b) RAFA setup

6.2.5.   FDTD simulations

A simulation of the NHA optical transmission was used to validate the measured results. Simulations were performed with a FDTD package from Lumerical Inc. In the simulation, a plane wave was projected to a single hole with Bloch wave boundary conditions as defined by the NHA geometry along the *x*- and *y*-axes and a perfectly matched layer boundary condition along the z-axis. The impact of incident angle to SP excitation modes was computed and compared with the RAFA measurement results.

6.3. Results and discussions

6.3.1.   Microscope setup results versus RAFA setup results

The light output of the RAFA was captured by the spectrometer first, then interpolated and mapped into a 2D graph (angle versus wavelength). A filter utilizing a

Fast Fourier Transform was performed afterwards to minimize the etaloning effect due to the spectrometer (see Ref [73]). The far field angular intensity map of the NHA was shown in Fig. 6-3 and the results from the microscope measurements had been overlaid on top of the intensity map (Fig. 6-3(a)). The RAFA result (background) was symmetric due to the uniformity of the illumination beam across all excitation angles. Four Surface Plasmon Polariton (SPP) excitation modes related to Pyrex-gold side of the NHA were observed, among which SPP (-1,0), (0, ±1) and (-1, 1) shifted towards red, and SPP (+1,0) shifted towards blue as the absolute value of the RAFA output angle increased. The microscope-based measurements revealed spectral peaks and valleys at each incident angle that were consistent with the RAFA-based measurements (Fig. 6-3(a)). The spectra measured by both setups were further compared side by side in Fig. 6-3(b-e). Spectral curves were consistent with each other, where the maximum offset between curves was only 5 nm. The offset might have arisen from a slight alignment error or a spectral skew due to the etaloning effect in the spectrometer. The consistency in measured transmission intensities between the RAFA setup and conventional microscope setup suggested that the proposed RAFA based angular spectral measurement system was able to correctly characterize angular dispersion diagram of the NHA. In addition, the RAFA setup was also able to measure the transmitted light at each radiation angle while the microscope setup could not. The obtained results proved that the zero order transmission spectrum captured by each RAFA channel at the same incident angle with an angularly uniform illumination beam was the same as the spectrum of the total transmitted light in microscope setup while the NHA was illuminated only at the corresponding incident angle. This result confirmed that the high order transmission signals of our NHA was minimum as the number of repetitive nano-hole arrays was sufficiently large.
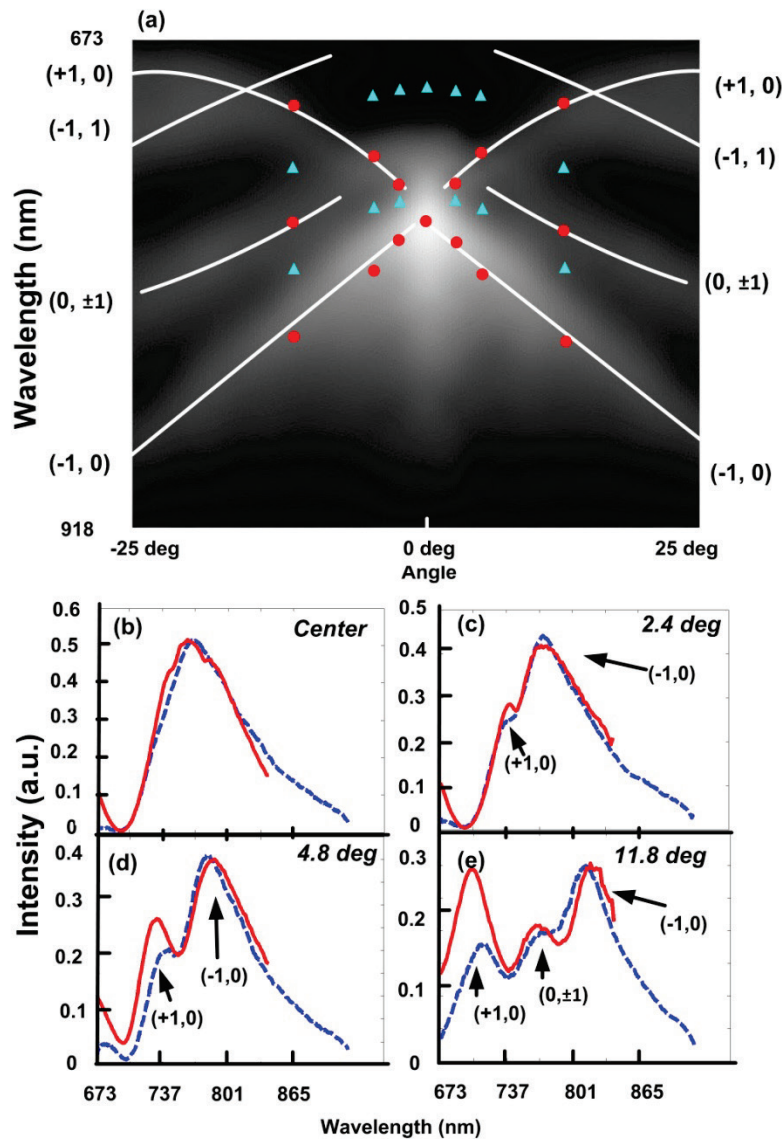
Fig. 6-3 (a) Far-field angular transmission intensity map of a NHA. Circles and triangles highlight resonance peaks and valleys detected with the microscope, respectively. (b-e) SP spectra from RAFA (dash line) and microscope (solid line) setups at 0^0 (normal to NHA surface), 2.4^0, 4.8^0 and 11.8^0 incident angles, respectively.

6.3.2. FDTD simulation results versus RAFA setup results

The measured transmission spectra from 0^0 to 22.5^0 were compared with the FDTD simulation results in Fig. 4. Both measured and simulation results showed only one resonance peak at 0^0 between 700 nm and 800 nm and the Wood's anomalies were

nearby 700 nm. As the incident angle increased, the resonance peak was split into (-1, 0) and (1, 0) peaks. The (-1, 0) peak shifted towards red, and (1,0) peak shifted towards blue in both cases. In addition, resonance peaks for (0, ±1) appeared at 12.5^0 and beyond, and they shifted towards red in both simulation and experiment (Fig. 4(a) and (b)). The only difference between the measurement and simulation results was the size of the red and blue shifts. The simulation results showed larger shifts, particularly at high angles. Although the cause of the discrepancy between simulation and experimental results remained unclear, imperfections within the NHA such as surface roughness were likely responsible [21, 27].
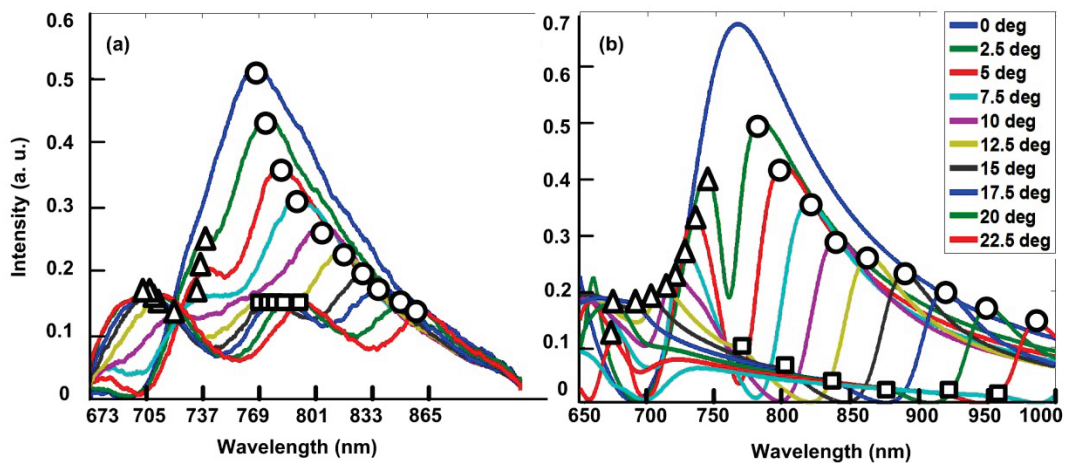
Fig. 6-4 Angular far-field transmission spectra (a) measured with the RAFA device, and (b) simulated by FDTD. The circular, triangular and square dots represent the peak of (-1, 0), (+1, 0) and (0, ±1) modes. respectively.

6.3.3.   RAFA-NHA based SPR sensing device

Fig. 6-3 and Fig. 6-4 demonstrated that RAFA-NHA based SPR sensing devices could perform analysis with both angular and spectral signals. RAFA is equivalent to an optical element that offers a high NA (0.57 in this project), remains achromaticity in a wide spectral range (from visible to infrared lights), and outputs collimated beams. The separation of the output beams could also be adjusted via changing the light guide channel length or pattern inside RAFA to fit the spectrometer [103]. In addition, RAFA based on system could eliminate the impact of scattering (Ref [127, 128]), allowing it to work while NHA is immersed into a turbid medium. It will facilitate NHA based SPR biosensing in case that the transmitted signals will be corrupted due to scattering in the

neighboring area of NHA. As the result, RAFA shall be superior to the existing devices that either only utilize the light near the normal direction of the NHA or use one objective lens to collected light transmitted through NHA when a scanning element is not feasible due to the limitation in device size and the requirement of real-time measurement [129, 130, 131].

6.4. Conclusion

In this study, the far-field angular transmission intensity map of a NHA was determined by a conventional microscope setup, a RAFA setup, and FDTD simulations. The RAFA setup captured the entire intensity map correctly with one or two exposures while the microscope setup was only able to provide a subset of the RAFA setup results after four measurements. The simplicity and measurement speed of RAFA-based angular spectroscopy may impact surface plasmon resonance sensing applications in both transmission and reflective modes with NHA or other devices where simultaneous discrimination of light transmission or reflectance by angle and color could improve performance [112, 120, 121, 122, 132].

7. Multispectral deep illumination angular domain spectroscopic imaging

7.1. Background

7.1.1. *Reflective methods for in-vivo optical imaging*

Section 1.3.1 reviewed the state-of-art of Optical Tomography modalities, particularly the reflective non-invasive *in-vivo* optical imaging methods as they could overcome impracticalities related to transmission-based optical imaging. OCT, CM, Two-photon Excitation Microscopy, Speckle Imaging, PAM and DOT are popular reflective OT imaging modalities. They were evaluated and compared in section 1.3.1 and Table 1-3, which suggested that the spatial resolution, depth detection and contrast mechanism determined the applications of these imaging modalities. Specifically, there was a need to have a reflective-based optical imaging technology that utilized endogenous contrast mechanism as PAM and could fill the gap between the imaging modalities with the higher resolution and shallower depth detection (OCT, CM) versus imaging modalities with greater depth detection and poorer resolution (DOT).

7.1.2. *The state-of-art of DI-ADI*

Angular domain imaging (ADI) detects optical contrast from targets embedded in a turbid medium via trajectory filtration of light. The key component of ADI is the angular filter array (AFA), which consists of an array of parallel micro-channels. Section 1.3.5 and 1.3.6 reviewed the recent progress of ADI and ADSI. In trans-illumination ADI, the AFA selects image-bearing photons that travel within the acceptance angle of the device and rejects image-degrading scattered photons. Angular filtration greatly improves the resolution and contrast of the resultant images [66, 67, 68, 69, 70, 71, 72, 73]. Angular domain imaging has been tested in various configurations, including trans-illumination with multi- and hyper-spectral analysis [66, 67, 69, 73], fluorescence [70], computed

tomography [68], and deep-illumination (DI-ADI), which is a reflection-based configuration [50].

In early work with DI-ADI, a laser was used to illuminate sub-surface objects from behind using the inherent scatter within the turbid medium [50]. Images were acquired by step-scanning the sample across the AFA and stacking the 1D line profiles captured at the AFA output at each step. For typical AFA geometries and scan protocols, images with sub-mm resolution covering a field of view of several square centimeters have been acquired [50]. Similar to DOT, DI-ADI results in an image characteristic of diffuse photons that are representative of the absorption and scattering properties of the sample. However, unlike DOT, the image-forming photons in DI-ADI travel back to the surface along trajectories falling within the acceptance angle of each AFA micro-channel. An absorber or a scatter will show up as a shadow in the obtained image as the imaging-forming photons will be either absorbed or scattered beyond the acceptance angle and filtered out by the AFA. This added feature of DI-ADI eliminates the need for computationally intensive image reconstruction approaches and improves image resolution for near surface objects in comparison to DOT.

7.1.3.   *Objectives*

The first objective of this work was to extend angular spectroscopic analysis into imaging field by incorporating multispectral capability into DI-ADI resulting in a new ADI modality called deep-illumination angular domain spectroscopic imaging (DI-ADSI). The second objective was to measure the performance of DI-ADSI using tissue-mimicking phantoms characteristic of human skin. The third objective was to test the effect of improved illumination and image post-processing techniques on DI-ADSI performance.

7.2. Methods

7.2.1.   *Tissue-mimicking phantoms*

A series of tissue-mimicking phantoms were employed in this project to overcome reproducibility issues with milk-based scattering media in previous

experiments [50]. Samples were fabricated using procedures developed in Ref [73] and section 5.3.1. Briefly, each phantom was cast in a plastic mold using mixtures of Indocyanine Green (ICG; I2633-25MG, Sigma Chemical Co., St Louis, MO)), Intralipid® (20%, Fresenius, Kabi AB, Uppsala, Sweden) and agarose (A-6013, Sigma Chemical Co.). The mold produced 6 homogenous targets 3 mm in diameter embedded in a background gel material. The background gel was formed from a mixture of Intralipid® and agarose. The targets were organized into 2 columns and 3 rows. Depths with respect to the front surface of the phantom were arranged by row and were 1 mm, 2 mm and 3 mm (Fig. 5-1 and Fig. 7-1(a)).

Targets were prepared by first dissolving agarose powder in a phosphate-buffered saline (PBS) solution at an elevated temperature. The target concentration of agarose was 1.0 wt%. The solution was allowed to cool to at least 56°C before the addition of ICG and Intralipid^{TM} and maintained at 50°C in a water bath to prevent hardening to a gel (hardening typically occurred in the range of 32 to 40°C) before injection into the mold. The location and the size of the targets were known due to precise knowledge of the mold geometry in combination with precise knowledge of the camera pixel size and the location of the phantom edges within the field of view of the camera. Indocyanine Green was added to achieve a final concentration of 20 µM. Intralipid^{TM} concentration ranged from 0.7 wt% to 2.0 wt% for the different phantom targets. The mixture was finally transferred into the mold using a 25AWG needle to form 6 spherical targets. Once the targets hardened (at room temperature), a separately prepared background mixture containing 2.0 wt% agarose in PBS and the same concentration of Intralipid^{TM} as used for the targets was poured into the phantom mold to create the body of the phantom around the targets. The phantom was left to harden at room temperature and was removed from the mold prior to imaging.

The absorption coefficient (μ_a) and scattering coefficient (μ_s) of Intralipid^{TM} have been shown to be close to the absorption and scattering coefficients of biological tissues [48, 49, 104]. Intralipid^{TM} has a scattering asymmetry factor (g) of 0.75 ± 0.18 and a μ_s of 362 cm^{-1} for 10 wt% that is proportional to concentration [48, 49, 104]. The absorption coefficient of 10 wt% Intralipid^{TM} has been shown to be on the order of 10^{-1} - 10^{-2} cm^{-1} (between 600 nm and 950 nm) [48, 104]. Therefore, the attenuation of light by a gel composed of Intralipid^{TM} and agarose is primarily due to scattering. Using the same

112

reference sources, the equivalent reduced scattering coefficient (μ'_s) for Intralipid[TM] was computed to be 6 cm^{-1} and 20 cm^{-1} at a concentration of 0.7 wt% and 2.0 wt%, respectively.   Using a spectrophotometer (DU 640, Beckman, Brea, CA), the total attenuation of a 1 cm thick cuvette filled with 0.5 wt% Intralipid[TM] and 2.0 wt% agarose was measured as 2.5 OD. Assuming that the light loss was primarily due to the optical scatter, the spectrophotometer result suggested that the reduced scattering coefficient was approximately 8.1 cm^{-1} for 0.7 wt% Intralipid[TM], consistent with the estimated value from published sources [48, 104, 107].

The total attenuation of ICG in 1.0 wt% agarose solution after a 1 cm optical path was measured previously [73]. Light absorption was observed to be significant between 650 nm and 820 nm with an attenuation coefficient of 7.0 cm^{-1} at 780 nm for a 20 μM ICG solution. The spectra were similar to data presented in [90], where the reported absorption coefficient for 20 μM ICG in water was ~ 2 cm^{-1} at the peak.

7.2.2.   Experiment setup

Fig. 7-1(b) and (c) illustrate the DI-ADSI system. It consisted of a broadband light source (Quartz Tungsten Halogen lamp 50 W; Oriel, Stratford, CT), a near infrared bandpass filter, which was the combination of a longpass filter (645 nm, Part # 65.1365, Rolyn Optics Co., Covina, CA) and a shortpass filter (950 nm, 950FL07-50S, LOT-Oriel GmbH, Germany), a high speed random access monochromator (Delta Ram V; PTI, Birmingham, NJ), two line illuminators, a high-precision sample control stage (ILS250PP; Newport, Irvine, CA), an AFA (described below), and a line camera (TCE 1304; 8 μm x 200μm pixel size; 3648 pixels; Mightex Systems, Toronto, ON). The system was assembled using cage components (Thorlabs; Newton, NJ). In operation, the output beam of the QTH lamp was filtered by the near infrared filter selecting light in the band between 645 nm and 950 nm. The high speed random access monochromator then selected light in a specific band with the full width at half maximum (FWHM) of 30 nm. The beam at the output of the high speed random access monochromator was coupled into a bifurcated fiber optic line illuminator (QDF type; NA 0.55; Dolan-Jenner; Boxborough, MA). Each line of illumination was focused onto the front surface of the tissue-mimicking phantom via an achromatic lens (*f = 75 mm*, 650~1050 nm, 2 inch diameter). The depth of the focal point was adjustable, ranging from the phantom front

surface to 4.5 mm below the phantom front surface. The projection angles were 45 and -45 degrees with respect to the direction normal to the front surface of the phantom. The distance between the centers of two incident beams at the phantom front surface was 11 mm disregarding the depth of the focal point. The phantom was placed on the high precision stage. During the experiment, the stage was shifted along the *y*-axis at 0.2 mm/step.

The AFA has been described in detail elsewhere [73]. Briefly, the AFA had 200 parallel channels, where the length of each channel was 10 mm and the maximum acceptance angle of each channel was 0.23°. The aperture of each channel was 80 µm by 80 µm and the inter-channel wall thickness was 20 µm. The AFA channel periodicity was 100 µm. The length of the AFA in x-direction was 2.5 cm. The AFA was placed in the center of the apparatus between the two illumination arms and 5.5 mm away from the front surface of the phantom. Since the long axis of each AFA channel was normal to the phantom surface, the AFA only accepted back-illuminated photons, which were emitted in a direction perpendicular to the phantom surface.

Photons that managed to exit the AFA were captured by an optics system (1 inch cage) and were focused onto the CCD line camera. The camera was sensitive over the wavelength range from 350 nm to 1000 nm and its exposure time was adjustable.
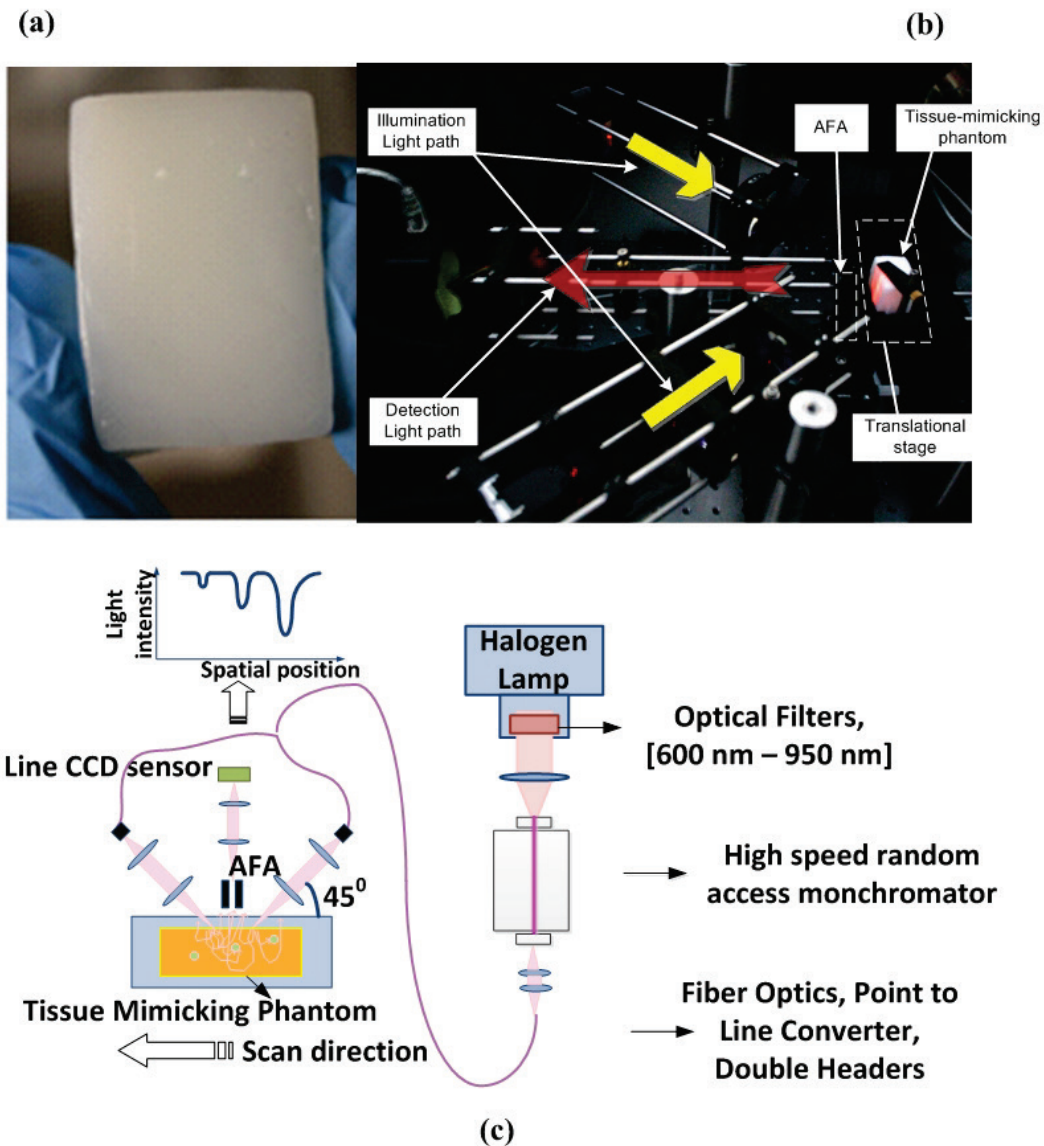
Fig. 7-1 (a) The appearance of tissue mimicking-phantom (front surface, 0.7 wt% Intralipid^{TM} as the phantom body). (b) Experimental setup for DI-ADSI. (c) Diagram of DI-ADSI setup

7.2.3. Image capture and restoration

A line image was captured by the CCD at each step and a 2D image was assembled from the ensemble of 145 line images resulting in a *y*-axis resolution of 0.2 mm. The same procedure was performed at 7 illumination wavelengths of 666 nm, 696 nm, 730 nm, 770 nm, 806 nm, 846 nm and 888 nm. The pixel intensity values in the 2D image were scaled to a normalized dynamic range according to the exposure time. The

vertical dark and bright pattern in Fig. 7-2 due to the channel spatial periodicity was removed by the summation of the pixel data representative of each channel output. This process was equivalent to compressing the image along the *x*-axis. The image was then processed by a Sobel operator to identify the boundary of phantom [133]. The positions of the boundaries (as shown in Fig. 7-2) were then utilized to crop the areas outside the phantom from the image. A statistical approach was used to remove pixels representative of defective channels (e.g. physically blocked) in the cropped image. A defective channel was defined as

$$I_{column\_mean} < I_{image\_min} + 0.85 \times (I_{image\_mean} - I_{image\_min}) \ ,$$

(7.1)

and

$$\delta_{column} < 0.6 \times \delta_{image} \ ,$$

(7.2)

where I_{column_mean} and δ_{column} refer to the mean intensity value, and the intensity standard deviation of the defective channel across all rows, respectively, and I_{image_mean}, I_{image_min} and δ_{image} refer to the mean intensity value, minimum, and the intensity standard deviation of all the pixels in the image. Once identified, the defective channel was removed by interpolation based on neighboring columns. The last step of image restoration was to remove the non-uniformity in the image due to the variations associated with the illumination beam and AFA channels. It was achieved by normalizing the data along each row according to the mean value of rows where no feature was present.
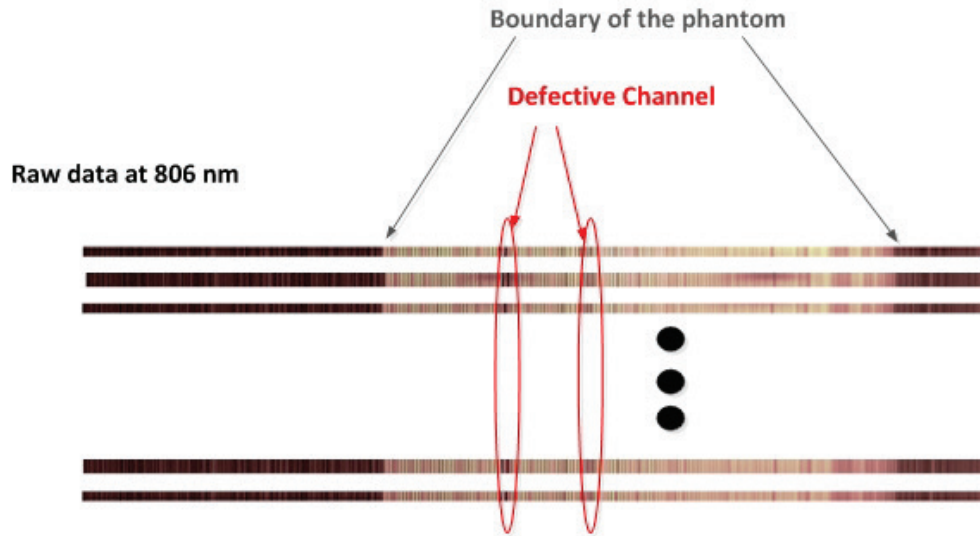
Fig. 7-2 Raw measurement data at 806 nm of a tissue-mimicking phantom composed of 0.7 wt% Intralipid^{TM}, agarose gel, and ICG-containing targets.

7.2.4.   Segmentation

Further image processing was used to extract the shape of detected features. The first step was to perform histogram equalization, which effectively increased the image contrast when the SNR was weak. Since 6 potential features were identified after image restoration, the entire image was divided into 6 (3 x 2) regions and each region contained one candidate feature. Histogram equalization was performed locally within each region. This procedure was necessary to account for the large differences in image contrast between shallow targets and deep targets. A modified Otsu segmentation algorithm [133] was applied to the histogram equalized image to group pixels into two classes: zero (0) for target, and one (1) for background. Segmentation was conducted locally as well using the same region division as used in the histogram equalization process.   Since the tissue-mimicking phantom contained absorptive features, a modification to the standard Otsu segmentation program was developed, which skewed the threshold intensity between two classes towards zero. The revised threshold was $I'_{median} - 1.5 * \delta'_{image}$, where I'_{median} and δ'_{image} represented the median pixel intensity value and the standard deviation of the histogram equalized image, respectively.

7.2.5. Point Spread Function (PSF) analysis

The PSF was estimated to approximate the spatial resolution of the DI-ADSI images. The PSF was estimated by deconvolution of the binary image obtained at 806 nm with a binary image of the expected shape of the features (reference image). The deconvolution was performed with a regularized filter [134] for each target region separately. The method was validated by recovery of the original image after convolving the reference image with the obtained PSF in 2D. The measured FWHM of the center peak of the PSF provided an estimate of image spatial resolution.

7.3. Results and discussion

7.3.1. Raw images and impact of dual beam illumination

A sample raw DI-ADSI result obtained at 806 nm from a 0.7 wt% Intralipid® phantom is presented in Fig. 7-2. The periodic bright and dark patterns corresponded to the channel apertures and walls, respectively. The cross-talk between channels was weak as the output from each channel was clearly separated by an intervening shadow due to the intervening channel wall. Signals related to defective channels were corrected during the image restoration process. Special attention was paid to the variations in background illumination in the raw image as the primary objective of introducing dual beam illumination was to minimize such variations. The measured results showed that the variations in background dropped from 40~50% of the dynamic range found in the previous work [50] to 15% in the present work. The increased uniformity in image brightness due to dual beam illumination aided image restoration, resulted in better image segmentation, and provided more consistent contrast changes for targets at the same depth (see Fig. 7-3(a-g)).
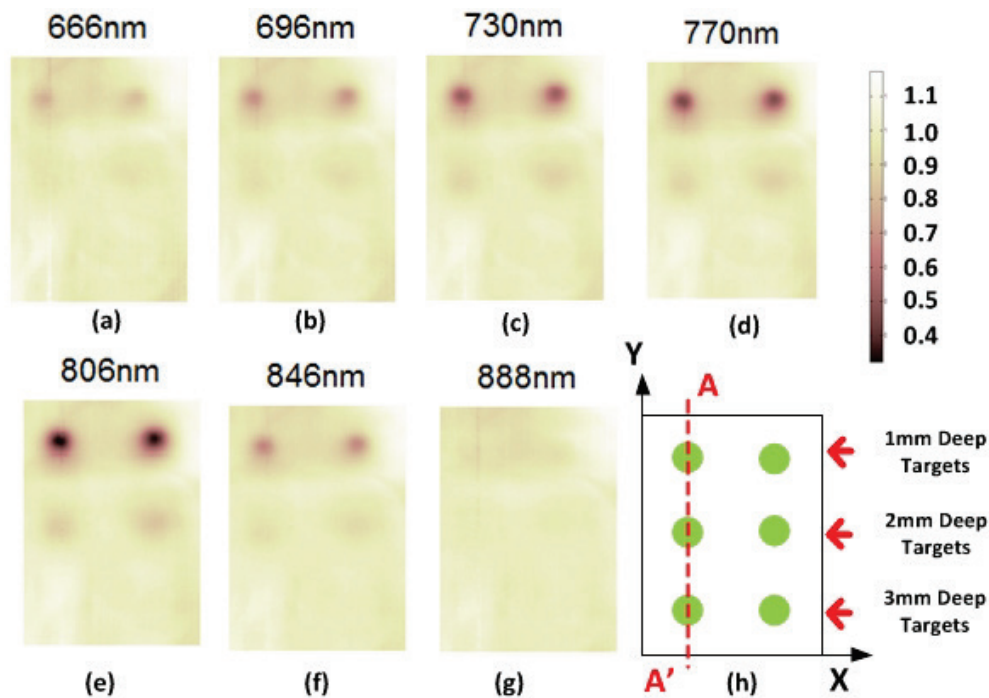
Fig. 7-3 Multi-spectral analysis of a tissue-mimicking phantom presented in Fig. 7-1(a). The illumination beam was focused on the phantom surface. (a-g) Image restoration results for multi-spectral images. The color scale represents transmission intensity in arbitrary units. (h) Schematic of the phantom, indicating axes and relative depths of targets.

7.3.2.   Image restoration results at different wavelengths

Fig. 7-3(a-g) show images at 7 different wavelengths recovered from a 0.7 wt% Intralipid™ phantom. The images revealed that the effect of defective channels was successfully removed with the approach presented in section 7.2.3. Consistent with the absorption spectra of 20 μM ICG, targets were detectable from 666 nm to 846 nm, most distinct at 770 nm and 806 nm, but undetectable at 888 nm. The light intensity along the line A-A' in Fig. 7-3(h) was analyzed and the results are shown in Fig. 7-4(a). Absorptive features were confirmed at the expected locations of the 1 mm, 2 mm and 3 mm deep targets. To estimate the material composition of the detected features, multi-spectral analysis was conducted and the absorptive spectral curves are presented in Fig. 7-4(b). The spectra represent optical density and are compared with a measured 20 μM ICG absorption spectrum (obtained from Ref. [90]). It was noted that though the spectral curve shape was close to the ICG curve, the measured spectra were red-shifted. This

119

phenomenon was observed in previous work as well (see Ref. [73]). The primary reason for the red-shift was that at longer wavelengths, scattering in Intralipid® was reduced. Consequently, fewer photons would be diffusively reflected back to the surface, causing a shift of the intensity peak towards longer wavelengths. In addition, the measured spectra were from a mixture of ICG and Intralipid^{TM} and the imaging contrast was primarily determined by the ratio between ICG absorption and Intralipid^{TM} scattering. The weaker scattering of Intralipid^{TM} at longer wavelengths would enhance the contrast as long as the ICG absorption remained high. This would appear as an apparent red-shift in the measured spectra.
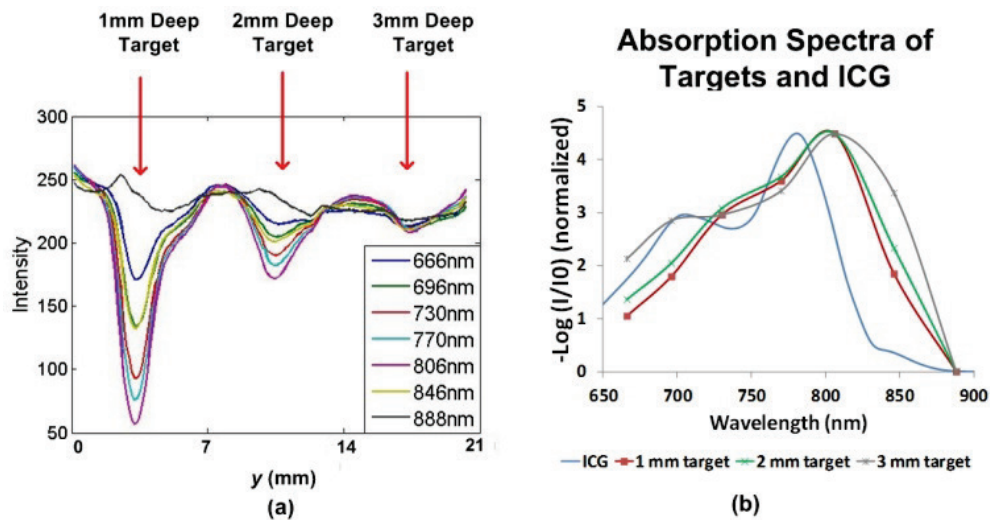
Fig. 7-4 (a) The spectral responses along A-A' in Fig. 7-3(h) in 0.7 wt% Intralipid^{TM} phantom. The illumination beam was focused on the phantom surface. (b) Normalized absorption spectra of three targets versus theoretic 20 µM ICG transmission spectrum after 1 cm^{-1} optical path.

7.3.3.   Image segmentation results at different wavelengths

The image restoration and multi-spectral analysis results described above confirmed that DI-ADSI could successfully detect shallow absorbers (1 mm deep) inside a tissue-mimicking phantom at the peak absorption wavelength and identify its material composition according to the spectral information. However, identification of deeper targets was more challenging due to the weak SNR. For example, the 2 and 3 mm deep ICG targets shown in Fig. 3(a-g) were blurred, and the signal strength (defined as the

height of the absorption peak) reduced by ~ 10x from 1mm deep target to 3 mm deep target in Fig. 7-4(a) at 806 nm while the background noise remained the same. To aid identification in these borderline cases, we utilized an algorithm based on histogram equalization and segmentation to identify the target boundary (Section 7.2.4). Fig. 7-5(a-g) presents the histogram equalization and segmentation results. Each image was divided into 3 zones where each zone contained targets at a depth of 1 mm, 2 mm or 3 mm. Receiver operating characteristic (ROC) analysis was performed to measure the effectiveness of the classification algorithm in terms of the TPR (True Positive Rate) and the SPC (Specificity or True Negative Rate, equivalent to 1 - False Positive Rate (FPR)). The TPR and the SPC were calculated by examining pixels one by one with respect to the expected location of targets as marked in Fig. 7-5(h). Fig. 7-6(a-b) shows the sensitivity and specificity measurements for targets at three different depths at each wavelength. Both TPR and SPC should have been equal to 1 if the classification was ideal. The worst classification was at 888 nm as TPR, representing the sensitivity, was extremely low, and the second worst case was at 666 nm as either TPR or SPC or both were low for all targets. For 666 nm and 888 nm, the algorithm failed to identify targets at all depths, which was expected due to the low absorption of ICG at these wavelengths.
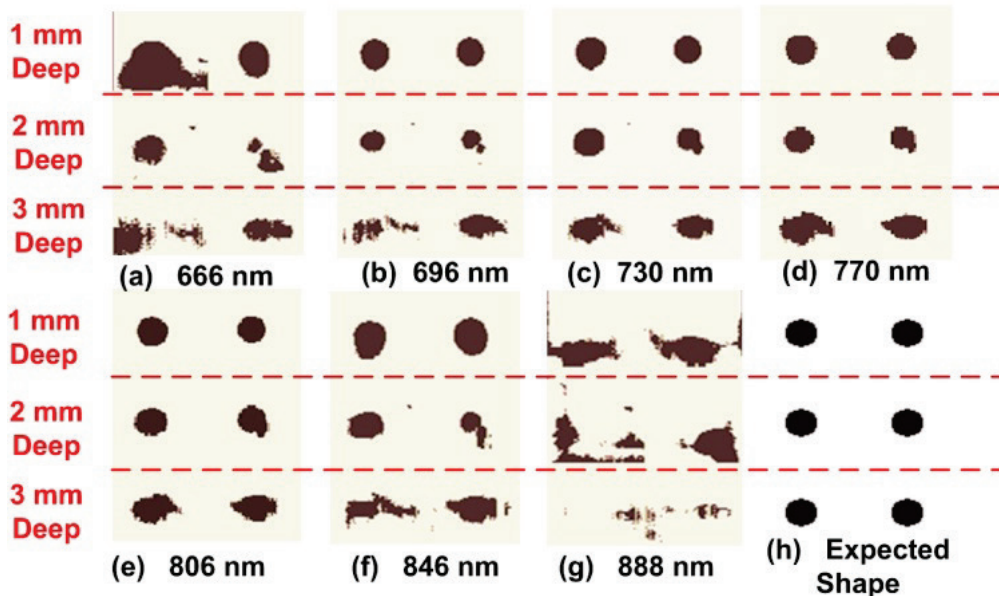
Fig. 7-5 The histogram equalization and image segmentation results for images presented in Fig. 7-3(a – g).

Targets at a depth of 1 mm were successfully recovered at wavelengths between 696 nm and 846 nm as shown in Fig. 7-5(b-f). At 806 nm, both TPR and SPC were close to 1 and the recovered shape and size were nearly identical to the expected shape (see Fig. 7-5(f)). The ROC result obtained at 770 nm for the 1 mm deep target was the second best overall. At 846 nm, the estimated targets were larger than the expected shape and corresponded to poorer specificity than those at 806 nm and 770 nm. For 2 mm deep targets, the geometry was recoverable with DI-ADSI between 730 nm and 806 nm. In comparison to 1 mm deep targets, specificity did not degrade, but the sensitivity was reduced, consistent with the fact that a portion on the right side of the target could not be recognized (Fig. 7-5(c-e)). As for 3 mm deep targets, the estimated shape and size of targets could not be successfully recovered and it was apparent due to a low specificity (FPR doubled); however, sensitivity was similar to the 2 mm deep targets. Taken together, the results suggested that 3 mm was near the reliable detection limit of DI-ADSI for a 0.7 wt% Intralipid^{TM} phantom.
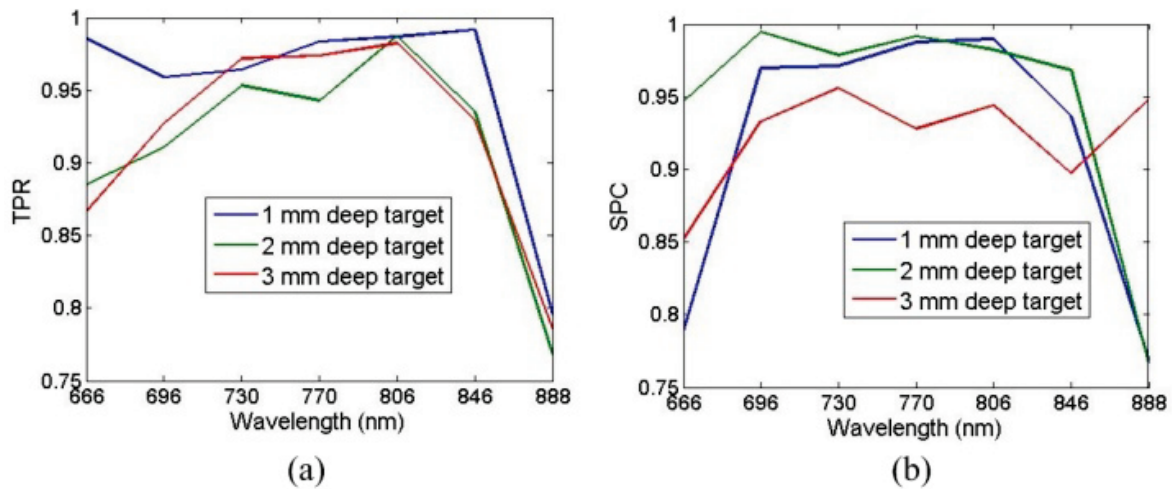
Fig. 7-6 (a) TPR plot for targets at three different depths shown in Fig. 7-5(a-g). (b) SPC plot for targets at three different depths shown in Fig. 7-5(a-g).

7.3.4. Impact of Intralipid^{TM} concentration on image brightness and contrast

A dependence of image brightness on Intralipid® concentration was observed. Fig. 7-7(a) shows an intensity line profile along line A-A' in Fig. 7-3(h) at 806 nm for phantoms with 0.7 wt% to 2.0 wt% Intralipid^{TM}. The intensity was normalized according to the exposure time used in each scan. The overall brightness of the image dropped as the concentration increased. For instance, from 0.7 wt% to 1.2 wt% Intralipid^{TM}, brightness dropped by 70-80%. To compare image contrast, the measured intensity line profiles were normalized according the minima at the 1 mm deep target Fig. 7-7(b)). The contrast of targets increased when Intralipid^{TM} concentration increased from 0.7 wt% to 0.9 wt% and then decreased afterwards. Targets at all three depths remained detectable even when the background Intralipid^{TM} concentration increased beyond 1.5 wt% ($\mu'_s \geqslant$ 13.6 cm⁻¹). This behavior suggested that the dependence of the number of image-forming photons on the Intralipid^{TM} concentration was more complicated for DI-ADSI compared to transmission-based ADSI. Earlier work from our group found that image contrast dropped monotonically as Intralipid^{TM} concentration increased during trans-illumination imaging. The effect was attributed to increased scatter and reduced numbers of image-forming quasi-ballistic photons reaching the detection side of the sample [69]. The biphasic contrast response observed with DI-ADSI might be related to the fluence-depth profile for a scattering medium, which is expected to have a peak below the surface, where the position and size of the peak are dependent on the scattering level (i.e. Intralipid^{TM} dilution factor). For a target at a fixed depth, a greater number of backscattered photons (i.e. the source of photons available for image formation) would be expected for an intermediate scattering level, where the peak of the fluence-depth profile occurs at a depth greater than the target. In comparison, weaker scattering levels would give fewer image-forming backscattered photons and higher scattering levels would place the peak in front of the target. In both cases the apparent image contrast would be lower.

7.3.5. *Impact of illumination focal depth of image brightness and contrast*

Compared to single point illumination, dual beam illumination was expected to improve image contrast and image brightness. Furthermore, image quality was expected to improve when the illumination beams were focused at an optimal depth. Focusing below the surface had the advantage of preventing specular reflections from entering the detection optics since the illumination beams were limited to two narrow lines physically separated from the line of detection. We performed a series of experiments at three different focal depths (0, 2, and 4 mm) using a phantom with a 1.2 wt% Intralipid^{TM} concentration. For each illumination scenario, the angle of incidence and location of the illumination beams were left unchanged. Fig. 7-7(c) shows the measured light intensity along A-A' in Fig. 7-3(h) at 806 nm. These curves were normalized to their minima at the 1 mm deep targets (Fig. 7-7(d)). Fig. 7-7(c) reveals that the overall brightness of the image dropped as the focal point increased in depth. However, the drop in image brightness was accompanied by an increase in contrast Fig. 7-7(d)). To better understand this behavior, we compared the experiment to the simulation results presented in [134, 135], where the absorption density, or the fluence rate transport, T, in a turbid light-scattering medium was simulated, while the focus of the illumination beam was scanned vertically down through the medium. The reference simulations indicated that the fluence delivered to the focal point (i.e. proportional to the background illumination in DI-ADSI) was reduced substantially when the beam was focused from the sample surface to within one mean free path (MFP). Beyond one MFP, the fluence continued to drop but at a slower rate. On the other side, the signal intensity reduced while the background illumination source moved deeper and the reduction could be explained by μ'_s, which was a constant. Therefore, the reported simulation suggested that the image contrast (signal / background) would slightly increase though the overall brightness would drop while the focal depth of the illumination beams increased, which was consistent with our experimental results.
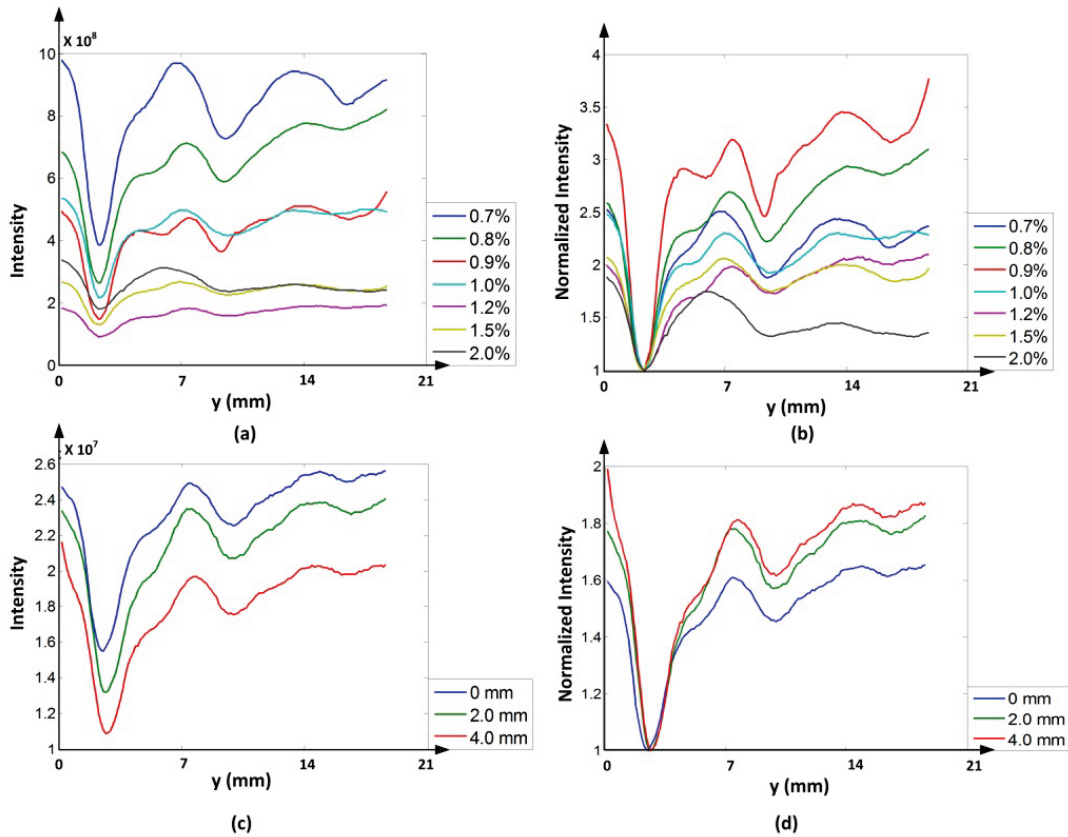
Fig. 7-7 (a) Intensity line profiles obtained along A-A' in Fig. 7-3(h) at 806 nm for multiple phantoms with different Intralipid[TM] concentrations. (b) Normalized curves representative of data in (a). (c) Intensity line profile along A-A' in Fig. 7-3(h) for the phantom with 1.2 wt% Intralipid[TM] background. The focal depth of the illumination beam was 0 mm, 2 mm, or 4 mm deep. (d) Normalized curves representative of data in (c).

7.3.6. Spatial resolution of DI-ADSI

The spatial resolution of DI-ADI has been examined in earlier work for a moderately scattering medium (see Ref. [50]), where a series of L-shape targets were imaged. The earlier work demonstrated that DI-ADI could resolve L-shaped targets with lines and spaces of about 0.2 mm up to 3 mm below the surface of a medium with μ'_{eff} of 4.7 cm^{-1}. For images acquired with DI-ADSI, spatial resolution was limited by both instrument capability and sample properties. The instrument capability was determined by AFA geometry, the scanning step size, and the camera resolution, which were 0.1 mm (channel periodicity), 0.2 mm, and 8 µm (along the longitudinal axis of the AFA),

respectively. Therefore, we expected the image resolution of DI-ADSI system to be less than 1 mm.

The spatial resolution is also affected by the structure and the optical properties of the sample and can be estimated from the PSF. In real tissue samples with natural chromophores, heterogeneity, and high levels of scattering, the resolution will drop as the depth increases and the PSF will be wider with stronger noise levels. Fig. 7-5(e) was considered as the best candidate image to compute an estimate of the PSF, which is presented in Fig. 7-8(noise less than half of the peak signal magnitude was not presented). For 1 mm deep targets, the PSF estimates suggested that the spatial resolution was about 0.4 mm. For 2 mm deep targets, the computed PSFs showed that the resolution was poorer in the x-direction at approximately 0.6 mm. For 3 mm deep targets, the central peak of the PSF was not measurable and the spatial resolution of the image could not be properly evaluated. Taken together, the previous work on DI-ADI in combination with the current phantom results, led us to conclude that DI-ADSI could provide sub-millimeter spatial resolution for targets at a depth between 2 and 3 mm.
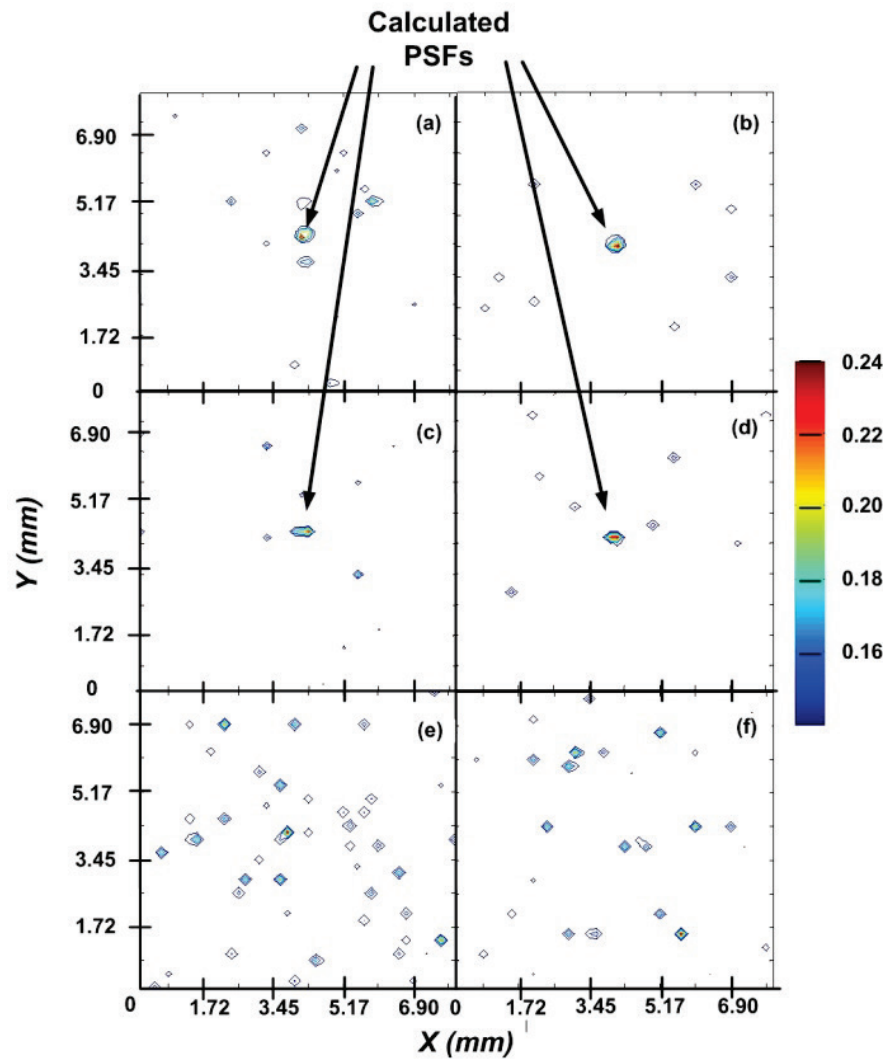
Fig. 7-8(a-f) Calculated PSFs for objects in Fig. 7-5(e) from top left to bottom right

7.4. The applications of DI-ADSI and limitations

Review of the work described in Refs. [42, 107, 109] suggested that the reduced scattering coefficients of human skin, including epidermis, dermis, and subcutaneous fat are expected to be within the range of 10 cm^{-1} to 40 cm^{-1} in the spectral range from 600 nm to 900 nm, which are similar to the optical properties of the tissue mimicking phantoms. In addition, the absorption coefficient of human skin has been reported to be typically less than 1 cm^{-1} [40, 42, 107] and blood is known to have an absorption coefficient that is up to 2-3 orders of magnitude larger between 600 nm and 700 nm due

to hemoglobin [41]. Based on these estimates, the attenuation due to blood vessels near the skin should be comparable to the attenuation observed from ICG and Intralipid^{TM} in the tissue mimicking phantoms. Therefore, DI-ADSI should be capable of non-invasive imaging of subcutaneous features, such as the vasculature that feed skin tumors. Furthermore, based on our findings DI-ADSI should be capable of imaging these high contrast objects up to at least 2 mm below the skin surface with a spatial resolution better than 1 mm.

In comparison to the earlier work, our results demonstrated that the dual illumination setup was capable of generating uniform background illumination, which resulted in improved image contrast. Furthermore, the measurement result in Section 7.3.5 led us to conclude that the illumination beam should be focused as deep as possible as long as the overall brightness is sufficient for detection. We estimated the detection limit for DI-ADSI to be approximately 3 mm; therefore, 4 mm represents a reasonable focal depth for future work.

Our multispectral analysis method only utilized 7 wavelength bands. Although the analysis was effective with strongly absorbing targets, better spectral resolution would likely be required for accurate identification of material composition of targets in tissue imaging applications, where targets are likely to be more complex in shape and spectral response, and of lower optical absorption. In these more difficult cases, hyperspectral analysis implemented with a spectrometer may prove to be superior.

7.5. Conclusion

This chapter presented developments related to DI-ADSI, which is a reflectance-based optical imaging technique based on an AFA. The work also utilized tissue-mimicking phantoms with absorptive targets to evaluate DI-ADSI. Image restoration and segmentation of DI-ADSI data resulted in successful identification of 3-mm diameter absorptive targets up to 2~3 mm below the surface of phantoms composed of 0.7 wt% to 2.0 wt% Intralipid^{TM} and agarose gel. The spatial resolution was less than 1 mm and the field of view was 2.5 cm by 3.0 cm. Multispectral analysis successfully extracted the absorption spectra of the targets according to the measured intensity at the target

locations. The spectra of the detected ICG-loaded targets were similar to the ICG absorption spectrum as expected. The relationships between image brightness, image contrast, Intralipid^{TM} concentration and the focal depth of the illumination beams were measured. The results confirmed that DI-ADSI was able to detect absorptive targets (such as 20 μM ICG) embedded in a scattering medium representative of human skin.

8. Summary and future work

8.1. Overview

This chapter summarizes the dissertation based on the results from the studies described in Chapter 2 through 7. The summary is categorized into two sections: angular domain spectroscopic analysis devices and angular domain spectroscopic imaging. The potential applications of the developed technologies are proposed. In addition, a perspective and outlook for future research are discussed. Finally, this chapter concludes the thesis with the overview of the scientific contributions of the project.

8.2. Angular domain spectroscopic analysis devices

8.2.1. Device development

The primary function of Radial Angular Filter Array (RAFA) is to collect the angular distribution of photons for angle-resolved spectroscopic analysis without scanning or rotating the sample or the detector. The basic concept of RAFA is to use a radial-distributed series of micro-channels, facing a focal point which is several millimetres away from the edge of the device, as waveguides to capture and guide photons in different directions to the detector. Precise angular filtration, easy output coupling and achromaticity are three key features offered by RAFA for target applications.

RAFA achieves precise angular filtration in the same way as AFA in ADI, in which each micro-channel only allows photons traveling within its acceptance angle to pass through. Smaller acceptance angle can be achieved via increasing the aspect ratio (length / width) of the channel. However, the signal strength drops at the same time. Two design paradigms, constant acceptance angle and constant aspect ratio, were described

in Section 2.3.2. Constant acceptance angle designs modify the channel shape to preserve a very high angular resolution, however, crosstalk increases due to the reduction in channel wall thickness. Constant aspect ratio devices are able to achieve smaller acceptance angle and less cross-talk with the scarification in angular resolution. Other design improvements in terms of angular filtration were addressed in Section 2.3.5. The main idea is to pattern the channel wall for better noise reduction due to photons outside the acceptance angle.

Multiple design and simulation efforts have been conducted to reduce the complexity of output coupling. A mirror-like reflection plane inside RAFA channels is the critical element to ensure the outputs of all RAFA channels are collimated and a significant improvement in signal uniformity from the conceptual device (Section 2.3.2 and 2.3.3).

The chromaticity of RAFA is determined by the micro-channels geometry design. Layouts presented in Section 2.3.8 and dimension reports in Section 2.3.2 confirm that the angular filtration of the device shall not be affected by the photon wavelength in visible or near infrared spectra.

Other design considerations were detailed in Section 2.3.2 through 2.3.8. The overall design optimization goal is to minimize the crosstalk and reduce output signal non-uniformity as seen in the conceptual device by up to several magnitudes to enable the actual usage of RAFA in angular spectroscopic characterization. 14 designs with different combinations of the design parameters were proposed in Section 2.3.8 and they were fabricated via the procedure developed in Section 2.4.

8.2.2. Device validation

Chapter 3 presented the characterization results of proposed RAFAs, established a procedure to calibrate RAFA prior to usage, and demonstrated the usefulness of the RAFA as a device suitable for obtaining angle-resolved hyperspectral measures of light scattered from a turbid sample.

A series of experiments were performed to evaluate the impacts to channel crosstalk, channel leakage, and channel achromaticity due to different channel

structures, center channel blockage, and different output coupling schemes. The focal length in the studied range was confirmed to have no impact to RAFA performance. The signal output intensity variations at different angles of the best design were reduced from a few of orders of magnitude to within one order of magnitude across 70° with an angularly uniform incident beam. The inter-channel crosstalk in one of the best designs was reduced dramatically from that in the preliminary conceptual design, and the output light distribution was well-collimated within at least 6 mm from the output of the device. All RAFA designs maintained reasonable chromaticity in the evaluation. Results indicated that it was less than ±10% variations in device spectral response from 690 nm to 910 nm over 45° range. This result could be used to further compensate measured spectral response of the targets in subsequent applications.

RAFA calibration procedure followed the concept introduced in Section 1.2.1 and was developed in Section 3.2.3. In trial applications, the selected RAFA was calibrated first, then used to measure a series of homogeneous Intralipid™ dilutions with or without ICG additions. Results presented in section 3.4 demonstrated the capability of RAFA to measure the angular distribution of photons due to scattering and identify the differences in scattering behaviours at different wavelengths. In addition, the selected RAFA was able to detect the existence of an absorptive element inside the turbid medium from the angle-resolved absorptive spectra.

8.2.3.   Applications

The motivation of developing RAFA was to achieve real-time, low cost and simplified angular spectroscopy measurement. The aim was to replace bulky and slower goniometer-based instruments in macro-scale or complicated interferometric systems in micro-scale. Trial applications in Chapter 3 confirmed that the challenges due to design flaws with the conceptual RAFA were overcome by the latest RAFA designs. RAFA was able to offer similar angular resolution and coverage to what most goniometer-based systems offer; however, the data acquisition was only limited only by the exposure time of one camera, eliminating rotational scanning and the use of additional detectors. In addition, the RAFA offered a competitive advantage over low-coherence interferometry systems by enabling multispectral and hyperspectral measurements with simple

instrumentation. Subsequently, Chapter 4 to 6 focused on implementing RAFA to measure the angular spectroscopy of different sets of samples, in which the optical properties of the targets, the sample structure, and sample material composition were analyzed.

The first RAFA application was to measure the angle-resolved spectroscopy of homogenous scattering media (Intralipd^{TM} and Intralipid^{TM}/ICG solutions) as described in Section 3.4. The success encouraged the author to utilize RAFA to evaluate heterogeneous samples. Chapter 4 described a method to measure the depth of absorptive features inside a turbid medium with a RAFA. Experiments were performed with a focused illumination beam and a thin graphite rod inside Intralipid^{TM} dilutions at different concentration levels (up to 1.0 wt%, $\mu'_s = 9.0\ cm^{-1}$). The position mapping results confirmed that RAFA was able to measure the traverse location and depth of an absorptive sub-mm feature inside 0.3 wt% Intralipid^{TM} within 4.5 mm from the surface via the obtained angular distributions of the scattered photons. The next step was to evaluate the feasibility of using RAFA to characterize the optical abnormalities in human tissues (Chapter 5). A RAFA-based angular spectroscopy system was employed to measure the absorptive targets embedded within a tissue-mimicking phantom. The body of the phantom was made of Intralipid™/agarose gel and the targets were spherical (1.5 mm in radius) and contained 10 µM ICG. The measurement system included a broadband near infrared (NIR) collimated beam, RAFA and a pushbroom spectrometer. Experimental results indicated that this system could not only detect the existence of ICG targets, but also identify its material composition as the obtained absorptive spectrum of ICG was consistent with the literature result and data measured elsewhere [73]. Furthermore, the scattering properties of the background phantom could be extracted successfully via the measured angular spectroscopy disregarding the disturbances from the embedded ICG targets. In Chapter 6, RAFAs were used to characterize the optical angular transmission property of a sample which was not turbid. The light output from a nano-hole array (NHA) in an optically thick gold film contained large spectral variations due to the surface plasmon resonances (SPR) at different incident angles. The blue-shift and red-shift of the features in the surface plasmon features due to surface change at the NHA had become the fundamentals of SPR sensing. These behaviours were successfully characterized by RAFA-based angular

spectroscopies of NHAs. This apporach might improve the performance for sensing applications in micro-scale that utilize NHAs or other surface plasmon resonance coupling structures. Above all, this thesis project validated that RAFA based characterization systems were capable of measuring the angular spectroscopies of the objects important for structural characterization, bio-sensing, and material identification in both macro- and micro-scales.

8.2.4. Improvement to the existing system

As a novel angular spectroscopy analysis device, RAFA offers unique features and makes itself superior to existing macro- or micro- analysis devices. RAFA is similar to a convex lens as both of them can collect photons emitting from the focal point and guide them into the trajectories parallel to the optical axis. However, RAFA is significantly better than a lens when characterizing the material at the focal point because it is able to surpresses the noise due to photons emitting from other locations. As shown in Fig. 8-1, RAFA only allows photons emitting from the focal point to be transmitted to the camera and rejects photons emitting from other points in its focal plane. It is not the case when a lens is employed, in which the user won't be able to distinguish the source of the photons collected by the camera, not allowing to analyze the angular distribution of the photons emitting from the focal point only. This feature is particular important while a heterogenous turbid medium needs to be analyzed. Secondly, RAFA provides an achromatic high numerical aperature optical component with a cost as low as a few dollars. In this project, the numerical aperature of the RAFA is up to 0.64 and the device is achromatic in the near infrared spectrum. A lens with the similar optical properties will be at least 10 times more expensive.

As confirmed in Chapter 3, RAFA is able to collect photons propagating within the numercial aperature of the device at one exposure and identify their angles via their position in the camera image. In comparison to macro-scale scattering measurement system as shown in Fig. 1-4, RAFA is superior to the goniometer based systems (Fig. 1-4(a)) because it eliminates the angular scan of detector or sample which is lenghy or hard to be implemented. At the same time, the light output of the RAFA can be easily captured by a line camera. It does not require the multi-heads imaging system as shown

in Fig. 1-4(b). This enables the significant cost reduction, more importantly, the simplification of the measurement system.

(a)

(b)
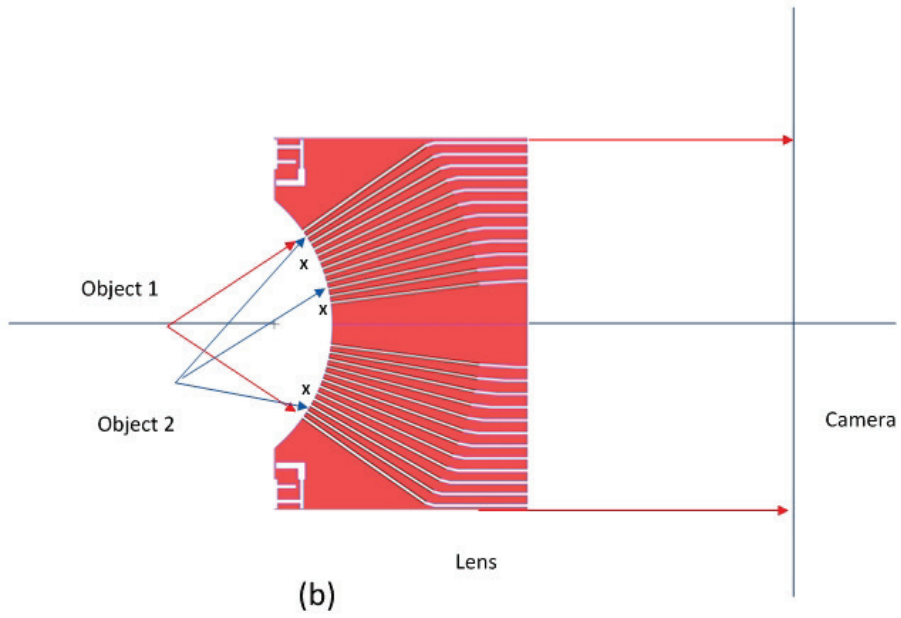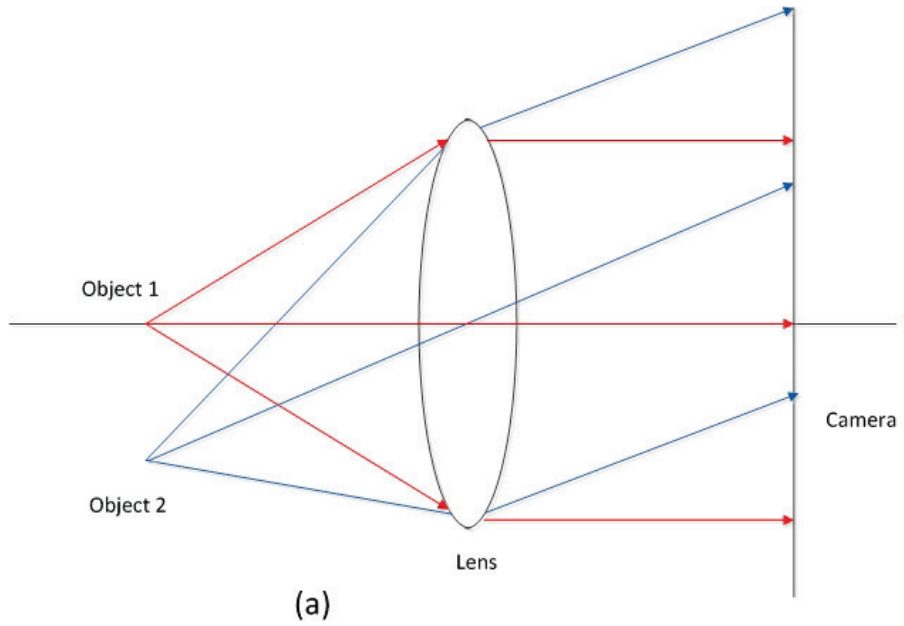
Fig. 8-1(a) Photons emitting from different locations can always pass through the lens and reach the camera. (b) Photons not emitting from the focal point will have high probability to be rejected by the RAFA and fail to reach the camera.

The low-coherent interferometry scattering measurement system (Ref [81]) is a representative of micro-scale scattering measurement system. It uses a drum lens to collect lights in the angular range of ~ ± 20 deg and photons are collimated after the lens. A point illumination to the lens focal point is employed to optically section the sample to avoid the issues associated with the lens as described in Fig. 8-1. However, it does not work well with highly scattered medium unless an inversion process is established like DOT. This method only provides the depth penetration to 1 mm while the RAFA focal length could be at least 7 mm as presented in this thesis project. Both RAFA and the low-coherent interferometric measurement system can measure the depth information of the target. RAFA achieves it via scanning the focal point of the device at different depths and the low-coherent interferometric measurement system obtains the depth information by interfering the scattered lights with the reference lights. In this case, RAFA can work with broad band light sources and spectrometers to gather both depth and spectral information at one exposure while a spectral scan is required with low-coherent interferometric measurement system.

8.3. Angular domain spectroscopic analysis in imaging fields

8.3.1. Improvement to the current system

Both RAFA and AFA are constructed from the concept of rejecting information-destroying photons and extracting information-bearing photons via angular filtration. RAFA focuses on processing photons from the focal point towards different directions while AFA works with photons from a line and propagating towards the direction aligned to the detector. Besides the progress made in RAFA, this thesis also expands the application of AFA to a novel reflectance optical imaging method, named as deep-illumination angular domain spectroscopic imaging (DI-ADSI). Different from most ADI and ADSI setups, this modality works in a reflectance illumination mode instead of well-

developed transillumination mode. The DI-ADSI modality enables multi-spectral imaging of sub-surface features for samples too thick for trans-illumination ADSI approaches. In addition, the improvements to the existing DI-ADI setups were incorporated and characterized in Chapter 7, which included using dual line illumination instead of a point laser illumination for better background uniformity and contrast, and employing a series of tissue mimicking phantoms instead of regular turbid media to understand the applications in biological tissues better.

8.3.2. Applications

DI-ADSI was developed as a non-invasive and *in-vivo* imaging modality to replace low resolution X-ray screening in areas such as mammograms and brain scans. In this thesis, this approach is implemented to characterize the tissue mimicking phantoms whose scattering level is up to 20 cm^{-1} in NIR, which is within the same range of the reduced scattering coefficients of human skin, including epidermis, dermis, and subcutaneous fat [42, 107, 109]. The attenuation due to ICG targets inside the tissue mimicking phantoms is comparable to the attenuation due to blood vessels near the skin. Measurement results indicates that DI-ADSI should be capable of non-invasive imaging of high contrast objects up to at least 2 mm below the skin surface with a sub-mm spatial resolution. In addition, blood is known to have an absorption coefficient that is up to 2-3 orders of magnitude larger human skin due to hemoglobin in NIR [41]. Thus, DI-ADSI system will be useful for subcutaneous tumour imaging while measuring the vasculature that feed skin tumours.

8.4. Future work

Future work in angular domain spectroscopic analysis device will focus on improving RAFA designs to facilitate new applications. The calibration and validation of the RAFA designs shall be performed with additional materials, where the size of the scatters is well known and the results could be compared against Mie theory. Also, the range of detection angles could be improved by adopting a design that avoids the use of center blocking channels, but incorporates other techniques to reduce the transmission efficiency for channels around the optical axis. Lastly, the current RAFA design is

essentially a point detector; however, device stacking could be used to build a device capable of angularly-resolved measurements across a line on the sample. Chapter 5 demonstrated the potential application of RAFA based angular spectroscopy in biomedical applications via charactering absorptive objects in the tissue mimicking phantom. The next step is to implement it to analysis biological soft issues like small animals, human breast and subcutaneous tissues.

Extensive efforts will focus on validating the predicted design advantages of RAFA-NHA system over other NHA based on SPR sensing devices. Miniaturized RAFA-NHA based SPR sensors will be designed and fabricated, the bulk sensing performance of the RAFA setup will be evaluated using solutions of known refractive index, and the sensitivity of the system in bio-sensing applications will be measured. We will also study the application of RAFA in non-NHA based SPR sensing devices, for example, using RAFA in Kretschmann configuration in which the resonance angle strongly depends upon the refractive index (RI) of the material immediately adjacent to the sensing surface and the determination of this angle provides a sensitive measurement of refractive index near the surface [136, 137, 138]. Furthermore, the use of angular response collected with the RAFA in the absence of spectral information could be considered as a design paradigm for constructing an integrated sensing device.

We propose that future work in angular domain spectroscopic imaging should include the implementation of hyperspectral detection and principle component analysis to examine whether DI-ADSI can accurately identify absorbers inside more complex turbid media. The influence of the illumination angle and the distance between the illuminators also needs additional investigation. However, a prudent next step will be to test DI-ADSI on a sample with unknown optical properties and validate the results via other methods, such as optical sectioning. The capability of DI-ADSI to image tissues with both heterogeneous scattering and absorptive properties should also be explored. After that, the successful imaging of biological soft tissues like like insects, animal embryos or small animal extremities shall be the next development target.

Ultimately, RAFA is expected to be utilized in angular domain optical tomography modalities like DI-ADSI and DI-ADFI. It will provide the depth information to allow three dimensional imaging in a simple setup. The angular spectroscopy obtained from RAFA

will potentially help to diagnose the observed abnormities in tissues in-situ. These features will enable the applications of deep illumination in angular domain spectroscopic imaging in diagnostically screening at point-of-care centers. Comprehensive angular spectroscopic characterization of biological tissues, new RAFA/AFA designs which integrate these two together, and improvements in spatial resolutions, portability and data acquisition speed are required to enable the applications in this field.

8.5. Conclusion

Scientific contributions of this thesis focus on angular domain spectroscopic analysis and imaging. The primary contribution of this thesis project was to develop RAFA from a concept to a full functioning device. In contrast to the AFA employed in ADI and ADSI, RAFA consists of a series of radially-distributed, instead of parallelly-distributed, micro-machined channels, where the long axes of the channels converge at a focal point. The output of the RAFA represents the angular distribution of photons emitted from the focal point. In particular, RAFA is an achromatic device in visible and near-infrared spectra. It enables both angular distribution analysis and hyper-spectral analysis simultaneously. The development of RAFA in this thesis project includes: 1) evaluating the preliminary conceptual device and proposing new design concepts to solve the issues that prevent the conceptual RAFA from real applications, including the non-uniform device output profile and inefficient output coupling due to inter-channel crosstalk; 2) designing and fabricating a series of RAFAs to validate all interested design parameters; 3) characterizing RAFA designs and establishing a calibration procedure to enable RAFA for actual applications; 4) using RAFA to obtain angle-resolved spectroscopies to characterize a series of biological homogenous and heterogeneous turbid media; 5) using a RAFA-NHA based angular spectral measurement system to characterize samples that have higher spectral variations compared to turbid samples. The main novelty of the contributions includes the idea of RAFA (co-invented with the former Phd student in the lab, Fartash Vasefi), new RAFA design paradigms (constant solid angle, constant aspect ratio, mirror bending structures, channel wall engineering , center channel blockage, and etc), and new applications associated with RAFAs (rapid angular spectroscopy measurement for material characterization and sensing, depth

resolved angular spectroscopy, and surface plasmons based angular spectroscopic sensing system).

The secondary contribution of this thesis project was to incorporate spectroscopy to the existing technique which we called Deep-Illumination Angular Domain Imaging (DI-ADI). A series of test system improvements and extensive imaging process techniques were practised to enable Deep-Illumination Angular Domain Spectroscopic Imaging (DI-ADSI) to image tissue-mimicking phantoms. The proposed imaging system demonstrated that its depth penetration, field of view and spatial resolution were between micro-reflectance-imaging technologies such as OCT and CM, and macro-reflectance-imaging technologies such as DOT. These results matched the value-proposition of the technology and suggested that DI-ADSI had the potential for low-cost and fast *in-vivo* tissue scanning for superficial targets. The main novelty of the contributions is the invention of reflectance multi-spectral angular domain imaging method.

Reference

1.	A. A. Kokhanovsky, *Light scattering media optics: problems and solutions*, 3rd edition, Springer- Praxis, UK, 2004.

2.	D. Contini, F. Martelli, and G. Zaccanti, "Photo migration through a turbid slab described by a model based on diffusion approximation. I. Theory," Appl. Opt. **36** (19), 4587 - 4599 (1997).

3.	D. A. Boas, "Diffuse photon probes of structural and dynamical properties of turbid media: theory and biomedical applications," Phd Thesis, University of Pennsylvania, (1996).

4.	A. Wax and V. Backman, *Biomedical applications of light scattering*, McGraw-Hill, NY, 2010.

5.	F. Mayinger and O. Feldmann, *Optical measurements*, 2nd edition, Springer, NY, 2001.

6.	J. C. Stover, *Optical scattering: measurement and analysis*, 3rd edition, SPIE press, Bellingham, WA, 2012.

7.	B. B. Das, F. Liu, and R. R. Alfano, "Time-resolved fluorescence and photon migration studies in biomedical and model random media", Rep. Prog. Phys. **60**, 227 - 292 (1997)

8.	S. R. Arridge, M. Schweiger, M. Hiraoka, and D. T. Delpy, "A finite element approach for modeling photon transport in tissue," Med. Phys. **20** (1), 299 - 309 (1993).

9.	N. Pfeiffer, "Imaging of turbid media using trajectory filter methods," Phd Thesis, Simon Fraser University (2009).

10.	F. Vasefi, "Advancements in angular domain optical imaging in biological tissue," Phd Thesis, Simon Fraser University (2010).

11.	E. Ambrocio, "A self-consistent obstacle scattering theory for the diffusion approximation of the radiative transport equation," MSc. Thesis, University of California, Merced (2008).

12.	T. R. Khan, "On derivation of the radiative transfer equation and its diffusion approximation for scattering media with spatially varying refractive indices," Technical Report, Clemson University (2007)

13. T. Durduran, A. G. Yodh, B. Chance, and D. A. Boas, "Does the photon-diffusion coefficient depend on absorption?," J. Opt. Soc. Am. A. **14** (12), 3358 - 3365 (1997).

14. S. L. Jacques, C. A. Alter, and S. A. Prahl, "Angular dependence of HeNe laser light scattering by Human Dermis," Laser Life Sci. **1**, 309 - 333 (1987)

15. L. Henyey and J. L. Greenstein, "Diffuse radiation in the galaxy," J. Astrophys., **93**, 70 - 83 (1940)

16. T. Vo-Dinh, *Biomedical photonic handbook*, CRC, 2003.

17. D. P. Gibbs, A. K. Fung, and A. J. Blanchard, "A bistatic optical scattering measurement system: design, fabrication, and experimental results," Proc. of Geoscience and Remote Sensing Symp., 2133-2136 (1990).

18. P.   Kadkhoda, W. Sakiew, S. Gunster, and D. Ristau, "Fast Total Scattering Facility for 2D Inspection of Optical and Functional Surfaces," Proc. SPIE 73890S (2009).

19. N. N. Boustany and N. V. Thakor, "Light Scatter Spectroscopy and Imaging of Cellular and Subcellular Events", in *Biomedical Photonics Handbook*, CRC press **16**, 1-23 (2003).

20. J. Miettinen, A. Harkonen, and T. H. Piironen, "An optical scattering measurement instrument for the design of machine vision illumination," Proc. SPIE **1614**, 45-56 (1991)

21. C. Y. Liu, T. A. Liu, and W. E. Fu, "Polarized optical scattering measurements of nanoparticles upon a thin film silicon wafer", Proc. IEEE Conf. on Nanotech.,116-119 (2008).

22. T. Weyrich, W. Matusik, H. Pfister, A. Ngan, and M. Gross, "Measuring skin reflectance and subsurface scattering," Mitsubishi Electric Research Laboratories.

23. R. Drezek, A. Dunn, and R. Richards-Kortum, "Light scattering from cells: finite-difference time-domain simulations and goniometric measurements," Appl. Opt. 38, 3651–3661 (1999).

24. R. Lu and Y. Peng, "Development of a multispectral imaging prototype for real-time detection of apple fruit firmness," Opt. Eng. **46** (12), 123201 (2007)

25. A. Wax, C. Yang, V. Backman, M. Kalashnikov, R. R. Dasari, and M. S. Feld, "Determination of particle size by using the angular distribution of backscattered light as measured with low-coherence interferometry," J. Opt. Soc. Am. A **19**, 737-744 (2002).

26. N. Bosschaart, D. J. Faber, T. G. van Leeuwen, and M. C. G. Aalders, "Measurements of wavelength dependent scattering and backscattering coefficients by low-coherence spectroscopy," J. Biomed. Opt. **16** (3), 030503 (2011).

27. F. E. Robles and A. Wax, "Measuring structural features using a dual window method for light scattering spectroscopy and fourier-domain low coherence interferometry," Proc. SPIE 7573, 757310 (2010).

28. R. Xu, *Particle characterization: light scattering methods*, Kluwer Academic Publishers, MA (2000).

29. J. C. Stover and E. L. Hegstrom, "Scatter metrology of photovoltaic textured surfaces." Proc. SPIE 7771, 777109 (2010)

30. T. F. Schiff, J. C. Stover, and B. D. Swimley, "Mueller matrix measurements of scattered light," Proc. SPIE 1753, 269 - 277 (1992)

31. J. D. Paumi, "Laser vs. camera inspection in the paper industry," Tappi Journal, Nov. (1988)

32. W. Burchard, "Static and dynamic light scattering from branched polymers and biopolymers," Adv. Polym. Sci., **48**, 1 - 123 (1983)

33. D. Some, "Light scattering based analysis of biomolecular interactions," Biophysical Reviews **5** (2), 147-158 (2013)

34. M. Wallace, L. T. Perelman, V. Backman, J. M. Crawford, M. Fitzmaurice, M. Seiler, K. Badizadegan, S. J. Shields, I. Itzkan, R. R. Dasari, J. van Dam, and M. S. Feld, "Endoscopic detection of dysplasia in patients with Barrett's esophagus using light-scattering spectroscopy," Gastroenterology **119** (3), 677 – 682 (2000).

35. V. Backman, V. Gopal, M. Kalashnikov, K. Badizadegan, R. Gurjar, A. Wax, I. Georgakoudi, M. Mueller, C. W. Boone, R. R. Dasari, and M. S. Feld, "Measuring cellular structure at submicrometer scale with light scattering spectroscopy," IEEE J. Sel. Top. Quantum Electron. **7** (6), 887-893 (2011)

36. V. V. Tuchin, *Handbook of optical biomedical diagnostics*, SPIE Press Bellingham WA (2002).

37. J. R. Mourant, I. J. Bigio, J. Boyer, R. L. Conn, T. Johnson, and T. Shimada, "Spectroscopic diagnosis of bladder cancer with elastic light scattering," Lasers Surg. Med. **17**, 350–357 (1995).

38. J. R. Mourant, A. H. Hielscher, A. A. Eick, T. M. Johnson, and J. P. Freyer, "Evidence of intrinsic differences in the light scattering properties of tumorigenic and nontumorigenic cells," Cancer **84**, 366–374 (1998).

39. http://www.nmr.mgh.harvard.edu/martinos/research/MultimediaGallery/DOT_mat erials/dot.html

40.   A. P. Dhawan, B. D'Alessandro and X. Fu, "Optical imaging modalities for biomedical applications," IEEE Rev. Biomed. Eng. **99**,1-25 (2010)

41.   S. Prahl, "Optical absorption of hemoblobin," http://omlc.ogi.edu/spectra/hemoglobin/index.html.

42.   R. R. Anderson and J. A. Parrish, "The optics of human skin," J. Invest. Dermatol. **77** (1), 13-19 (1981).

43.   M. A. O'Leary, D. A. Boas, B. Chance, and A. G. Yodh, "Experimental images of heterogeneous turbid media by frequency-domain diffusing-photon tomography," Opt. Lett. **20** (5), 426-428 (1995).

44.   Y. Zhang, F. Vasefi, E. Ng, A. Chamson-Reig, B. Kaminska, J. J. L. Carson, "Deep illumination angular domain spectroscopic imaging: tissue-mimicking phantom study," Proc. SPIE, 7896, 789676 (2011).

45.   A. F. Fercher, "Optical coherence tomography - principles and applications," Rep. Prog. Phys. **66**, 239–303 (2003).

46.   J. G. Fujimoto, "Optical coherence tomography," C.R. Acad. Sci Ser. IV (Phys. Astrophys.) **2**, 1099–1111 (2001).

47.   N. K. Logothetis, J. Pauls, M. Augath, T. Trinath, and A. Oeltermann, "Neurophysiological investigation of the basis of the fMRI signal," Nature **412**(6843), 150–157 (2001).

48.   S. T. Flock, S. L. Jacques, B. C. Wilson, W. M. Star, and M. J. C. van Gemert, "Optical properties of intralipid: a phantom medium for light propagation studies," Lasers Surg. Med. **12**, 510-519 (1992)

49.   H. Ding, J. Q. Lu, K. M. Jacobs, and X. H. Hu, "Determination of refractive Indices of Porcine Skin Tissues and Intralipid at Eight Wavelengths between 325 nm and 1557 nm," J. of Opt. Soc. Am. A **22** (6), 1151-1157 (2005).

50.   F. Vasefi, P. K. Y. Chan, B. Kaminska, and G. H. Chapman, "An optical imaging technique using deep illumination in the angular domain," IEEE J. Selected Topics in Quant. Elect. **13** (6), 1610-1620 (2007).

51.   R. Orzekowsky-Schroeder, A. Klinger, B. Martensen, M. Blessenohl, A. Gebert, A. Vogel, and G. Huttmann, "In vivo spectral imaging of different cell types in the small intestine by two-photon excited autofluorescence," J. Biomed. Opt. **16** (11), 116025 (2011).

52.   P. Zakharov, A. C. Volker, M. T. Wyss, F. Haiss, N. Calcinaghi, C. Zunzunegui, A. Buck, F. Scheffold, and B. Weber, "Dynamic laser speckle imaging of cerebral blood flow," Optics Express **17** (6), 13904-13917 (2009).

53.   A. M. Zysk, F. T. Nguyen, A. L. Oldenburg, D. L. Marks, and S. A. Boppart, "Optical coherence tomography: a review of clinical development from bench to bedside," J. Biomed. Opt. **12**, 051403 (2007).

54.   R. Wang, J. X. Yun, X. Yuan, R. Goodwin, R. R. Markward, and B. Z. Gao, "Megahertz streak-mode fourier domain optical coherence tomography," J. Biomed. Opt. **16** (6), 066016 (2011).

55.   H. Skvara, H. Kittler, J. A. Schmid, U. Plut, and C. Jonak, "In vivo fluorescence confocal microscopy: indocyanine green enhances the contrast of epidermal and dermal structures," J. Biomed. Opt. **16** (9), 096010 (2011).

56.   H. F. Zhang, K. Maslov, G. Stoica, and L. V. Wang, "Functional photoacoustic microscopy for high-resolution and noninvasive in vivo," Nat. Biotechnol. **24**, 848-851 (2006).

57.   N. Pfeiffer, B. Wai, and G.H. Chapman, "Angular Domain Imaging of phantom objects within highly scattering mediums," Proc. SPIE 5319, 135 - 145 (2004).

58.   J. Beuthan, O. Minet, G. Muller, V. Prapavat, "IR-diaphanoscopy in medicine," in *Medical Optical Tomography: Functional Imaging and Monitoring* (G. Muller, B. Chance, R. Alfano et al. eds.), 263-282(1993).

59.   K. Shimizu and M. Kitama, "Fundamental study of near-axis scattered light and its application to optical computed tomography," Opt. Rev. **7**, 383-388 (2000).

60.   P. van der Zee, R. Khalaf, L. Dixon, A. Davies, and R. Roy, "Optical medical tomography for the localisation of oxygenation in the limb," Proc. SPIE **3196**, 61-70 (1998).

61.   M. Tank and G.H. Chapman, "Micromachined silicon collimating detector array to view objects in highly scattering medium", Can Jour Elec. & Comp. Eng, .**25** (1), 13-18 (2000).

62.   V. Prasad, D. Semwogerere, E. R. Weeks, "Confocal microscopy of colloids," J. Phys.: Cond. Mat. **19**, 113102 (2007).

63.   G. H. Chapman, M. Trinh, N. Pfeiffer, G. Chu and D. Lee, "Angular domain imaging of objects within highly scattering media using silicon micromachined collimating arrays," IEEE J. Selected Topics in Quant. Elect. **9** (2), 257-266 (2003).

64.   G. H. Chapman, M. Trinh, G. Chou, N. Pfeiffer and D. Lee, "Optical imaging objects within highly scattering material using silicon micromachined collimating arrays," Proc. SPIE **4955**, 464-473 (2003).

65.   G. H. Chapman, P.K.Y. Chan, J. Dudas, J. Rao and N. Pfeiffer, "Angular domain image detectability with changing turbid medium scattering coefficients," Proc. SPIE **5695**, 160-171 (2005).

66. F. Vasefi, B. Kaminska, P. K. Y. Chan, and G. H. Chapman, "Multi-spectral angular domain optical imaging in biological tissues using diode laser sources," Optics Express **16**, 14456-14468 (2008).

67. F. Vasefi, B. Kaminska, G. H. Chapman, and J. J. L. Carson, "Image contrast enhancement in angular domain optical imaging of turbid media," Opt. Express **16**, 21492-21504 (2008)

68. F. Vasefi, E. Ng, B. Kaminska, G. H. Chapman, K. Jordan, and J.J.L. Carson, "Transmission and fluorescence angular domain optical projection tomography of turbid media," Appl. Opt. **48**, 6448-6457 (2009).

69. F. Vasefi, M. Najiminaini, E. Ng, B. Kaminska, G. H. Chapman, and J. J.L. Carson, "Angular domain trans-illumination imaging optimization with an ultra-fast gated camera", J. Biomed. Opt. **15** (6), 061710 (2010).

70. F. Vasefi, M. Belton, B. Kaminska, G. H. Chapman, and J. J. L. Carson, "Angular domain fluorescence imaging for small animal research," J. Biomed. Opt. **15** (1) (2010) .

71. M. Najiminaini, F. Vasefi, K. M. Tichauer, T.Y. Lee, B. Kaminska, and J. J. L. Carson, "Angular domain fluorescence lifetime imaging: a tissue-like phantom study," Opt. Express **18** (22), 23247-23257 (2010).

72. E. Ng, F. Vasefi, B. Kaminska, G. H. Chapman, and J. J.L. Carson, "Contrast and resolution analysis of iterative angular domain optical projection tomography," Opt. Express **18** (19), 19444-19455 (2010).

73. F. Vasefi, M. Naijiminaini, E. Ng, Astrid Chamson-Reig , Bozena Kaminska , Muriel Brackstone , and Jeffrey J.L. Carson, "Trans-illumination hyperspectral imaging for histopathological examination of excised tissue," J. Biomed. Opt. **16** (8) 086014 (2011).

74. F. Vasefi, B. Kaminska, G. H. Chapman, and P. K. Y. Chan, "Angular domain imaging for tissue mapping," Proc. Bio Micro and Nanosystems, 39 - 45 (2006).

75. P. P. Dendy and B. Heaton, *Physics for diagnostic radiology*, 3rd Ed., CRC Press. (1999).

76. D. J. Brenner and E. J. Hall, "Computed tomography - an increasing source of radiation exposure,". N. Engl. J. Med. **357** (22), 2277 - 2284 (2007).

77. J. Bushburg, A. Seibert, E. Leidholdt, and J. Boone, *The essential physics of medical imaging*, Lippincott Williams & Wilkins, ISBN 0683301187 (2002).

78. R. Georgescu, D. Khismatullin, R. G. Holt, J. L. Castagner, O. A'amar, and I. J. Bigio, "Design of a system to measure light scattering from individual cells excited by an acoustic wave," Opt. Express **16**, 3496-3503 (2008).

79. Y. Oshikane, T. Kataoka, M. Okuda, S. Hara, H. Inoue, M. Nakano, "Observation of nanostructure by scanning near-field optical microscope with small sphere probe," Sci. Technol. Adv. Mater. **8**, 181-185 (2007).

80. A. Wax, C. Yang, V. Backman, K. Badizadegan, C. W. Boone, R. R. Dasari, and M. S. Feld, "Cellular organization and substructure measured using angle-resolved low-coherence interferometry," Biophys. J. **82**, 2256-2264 (2002).

81. Y. Zhu, N. G. Terry, J. T. Woosley, N. J. Shaheen, and A. Wax, "Design and validation of an angle-resolved low-coherence interferometry fiber probe for *in vivo* clinical measurements of depth-resolved nuclear morphology," J. Biomed. Opt. **16** (1), 011003 (2011).

82. D. P. Gibbs, A. K. Fung, and A. J. Blanchard, "A bistatic optical scattering measurement system: design, fabrication, and experimental results," Proc. Geosci. Remote Sensing, 2133-2136 (1990).

83. V. Krishnaswamy, P. J. Hoopes, K. S. Samkoe, J. A. O'Hara, T. Hasan, and B. W. Pogue, "Quantitative imaging of scattering changes associated with epithelial proliferation, necrosis, and fibrosis in tumors using microsampling reflectance spectroscopy," J. Biomed. Opt. **14** (1), 014004 (2009).

84. C. Lau, O. Scepanovic, J. Mirkovic, S. McGee, C. C. Yu, S. Fulghum, M. Wallace, J. Tunnell, K. Bechtel, and M. Feld, "Re-evaluation of model-based light-scattering spectroscopy for tissue spectroscopy, " J. Biomed. Opt. **14** (2), 024031 (2009).

85. T. Dennis, S. D. Dyer, A. Dienstfrey, G. Singh, and P. Rice, "Analyzing quantitative light scattering spectra of phantoms measured with optical coherence tomography," J. Biomed. Opt. **13** (2), 024004 (2008).

86. F. Vasefi, M. Najiminaini, E. Ng, B. Kaminska, H. Zeng, G. H. Chapman, and J. J. L. Carson, "Angle-resolved spectroscopy using a radial angular filter array," Proc. SPIE **7562**, 756209 (2010).

87. S. T. Flock, S. L. Jacques, B. C. Wilson, W. M. Star, and M. J. C. van Gemert, "Optical properties of Intralipid: a phantom medium for light propagation Studies," Lasers Surg. Med. **12**, 510-519 (1992).

88. H. G. van Staveren, C. J. M. Moes, J. Marle, S. A. Prahl, and M. J. C. van Gemert, "Light scattering in Intralipid -10% in the wavelength range of 400-1100 nm," Appl. Opt. **30**, 4507-4514 (1991).

89. Y. Zhang, F. Vasefi, M. Najiminaini, B. Kaminska, and J. J. L. Carson, "Optimization of radial angular filter arrays for detecting the angular distribution of light," Proc. SPIE **7894**, 78940M (2011).

90. S. Prahl, "Optical Absorption of Indocyanine Green (ICG)," http://omlc.ogi.edu/spectra/icg/index.html

91. M. L. J. Lnadsman, G. Kwant, G. A. Mook, and W. G. Zijlstra, "Light-Absorbing Properties, Stability, and Spectral Stabilization of Indocyanine Green," J. Appl. Physiol., **40**, 575-583 (1976).

92. F. Vasefi, B. Kaminska, K. Jordan, G. H. Chapman, and J. J. L. Carson, "Angular Domain Optical Projection Tomography in Turbid Medium," Proc. SPIE **7174**, 71740D (2009).

93. S. C. W. Hyde, R. Jones, N. P. Barry, J. C. Dainty, P. M. W. French, K. M. Kwolek, D. D. Nolte, and M. R. Melloch, "Depth-Resolved Holography Through Turbid Media Using Photorefraction," IEEE J. Selected Topics in Quant. Elect. **2** (4), 965 – 975 (1996).

94. C. Dunsby and P. M. W. French, "Techniques for depth-resolved imaging through turbid media including coherence-gated imaging," J. Phys. D: Appl. Phys. **36**, 207-227 (2003).

95. S. N. Ivers, S. A. Baranov, T. Sherlock, K. Kourentzi, P. Ruchhoeft, R. Willson, and K. V. Larin, "Depth-Resolved Imaging and Detection of Micro-Retroreflectors within Biological Tissue Using Optical Coherence Tomography," Biomed. Opt. Express **1** (2), 367-377 (2010).

96. S. C. W. Hyde, N. P. Barry, R. Jones, J. C. Dainty, and P. M. W. French, "Sub-100-µm Depth-Resolved Holographic Imaging Through Scattering Media in the Near Infrared," Opt. Lett. **20** (22), 2330-2332 (1995).

97. P. Ye, J. L. Paredes, Y. Wu, C. Chen, G. R. Arce, and D. W. Prather, "Compressive Confocal Microscopy: 3D Reconstruction Algorithms," Proc. SPIE **7210**, 72100G (2009).

98. L. Sacconi, I. M. Tolic-Norrelykke, R. Antolini, and S. F. Pavone, "Combined Intracellular Three-Dimensional Imaging and Selective Nanosurgery by a Nonlinear Microscope," J. Biomed Optics **10** (1), 014002 (2005).

99. B. B. Das, K. M. Yoo, and R. R. Alfano, "Ultrafast Time-Gated Imaging in Thick Tissue: A Step Toward Optical Tomography," Opt. Lett. **18**, 1092-1094 (1993).

100. K. M. Yoo, Q. R. Xing, and R. R. Alfano, "Imaging Objects in Highly Scattering Media Using Femtosecond Second Harmonic Generation Cross Correlation Time-Gating," Opt. Lett. **19**, 1019-1021 (1991).

101. J. A. Moon, R. Mahon, M. D. Duncan, and J. Reintjes, "Three-Dimensional Reflective Image Reconstruction Through a Scattering Medium Based on Time-Gated Raman Amplification," Opt. Letter. **19**, 1234 – 1236 (1994).

102. J. Watson, P. Georges, T. Lepine, B. Alonzi, and A. Brun, "Imaging in Diffuse Media with Ultrafast Degenerate Optical Parametric Amplification," Opt. Lett. **20**, 231-235 (1995).

103. Y. Zhang, F. Vasefi, M. Najiminaini, B. Kaminska, and J. J. L. Carson, "Radial angular filter arrays for angle-resolved scattering spectroscopy," Opt. Express **21**, 2928-2941 (2013).

104. S. Jacques, "Optical Properties of 'IntralipidTM', an Aqueous Suspension of Lipid Droplets," http://omlc.ogi.edu/spectra/intralipid/index.html.

105. M. R. Hee, J. A. Izatt, E. A. Swanson, and J. G. Fujimoto, "Femtosecond Transillumination Tomography in Thick Tissues," Opt. Lett. **18**, 1107-1109 (1993).

106. Y. Zhu, N. G. Terry, and A. Was, "Scanning Fiber Angle-Resolved Low Coherence Interferometry," Opt. Lett., **34** (20), 3196-3198 (2009).

107. A. N. Bashkatov, E. A. Genina, V. I. Kochubey, and V. V. Tuchin, "Optical properties of human skin, subcutaneous and mucous tissues in the wavelength range from 400 to 2000 nm," J. Phys. D: Appl. Phys. **38** (15), 2543-2555, (2005).

108. M. J. C. van Gemert, S. L. Jacques, H. J. C. M. Sterenborg, and W. M. Star, "Skin optics," IEEE Trans. Biomed. Eng. **36** (12), 1146-1154 (1989).

109. E. Salomatina, B. Jiang, J. Novak, and A. N. Yaroslavsky, "Optical Properties of Normal and Cancerous Human Skin in the Visible and Near-Infrared Spectral Range," J. Biomed. Opt. **11** (6), 064029 (2006).

110. O. C. Marina, C. K. Sanders, and J. R. Mourant "Correlating light scattering with internal cellular structures," J. Biomed. Opt. **3**, 296-312 (2012).

111. Y. Oshikane, T. Kataoka, M. Okuda, S. Hara, H. Inoue, M. Nakano, "Observation of nanostructure by scanning near-field optical microscope with small sphere probe," Sci. Technol. Adv. Mater. **8**, 181-185 (2007).

112. K. A. Tetz, L. Pang, and Y. Fainman, "HIgh-resolution surface plasmon resonance sensor based on linewidth-optimized nanohole array transmittance," Opt. Lett. **31**, 1528-1530 (2006).

113. E. Ozbay, "Plasmonics: merging photonics and electronics at nanoscale dimensions," Science **311**, 189-193 (2006).

114. X. Dou, P. Y. Chung, P. Jiang, and J. Dai, "Surface plasmon resonance and surface-enhanced raman scattering sensing enabled by digital versatile discs," Appl. Phys. Lett. **100**, 041116 (2012).

115. P. Adam, M. Piliarik, H. Sipova, T. Springer, M. Vala, and J. Homola, "Surface plasmons for biodetection," in *Photonic sensing: principles and applications for safety and security monitoring,* G. Xiao and W. J. Bock eds. (Wiley. 2012).

116. J. R. Sambles, G. W. Bradbery, F. Yang, "Optical excitation of surface plasmons: an introduction," Contemp. Phys. **32**, 173-183 (1991).

117. T. W. Ebbesen, H. J. Lezec, H. F. Ghaemi, T. Thio, and P. A. Wolff, "Extraordinary optical transmission through sub-wavelength hole arrays," Nature **391**, 667-669 (1998).

118. M. H. Lee, H. Gao, J. Henzie, and T. W. Odom, "Microscale arrays of nanoscale holes," Small **3**, 2029-2033 (2007).

119. H. F. Ghaemi, T. Thio, D. E. Grupp, T. W. Ebbesen, and H. J. Lezec, "Surface plasmons enhance optical transmission through subwavelength holes," Phys. Rev. B **58**, 6779-6782 (1998).

120. D. Sinton, R. Gordon, and A. G. Brolo, "Nanohole arrays in metal films as optofluidic elements: progress and potential," Microfluid Nanofluid, **4**, 107-116 (2008).

121. L. Pang, G. M .Hwang, B. Slutsky, and Y. Fainman, "Spectral sensitivity of two-dimensional nanohole array surface plasmon polariton resonance sensor," Appl. Phys. Lett. **91**, 123112 (2007).

122. A. A. Yanik, A. E. Cetin, M. Huang, A. Artar, S. H. Mousavi, A. Khanikaev, J. H. Connor, and H. Altug, "Seeing protein monolayers with naked eye through plasmonic Fano resonances," PNAS **108**, 11784-11789 (2011).

123. W. L. Barnes, W. A. Murray, J. Dintinger, E. Devaux, and T. W. Ebbesen, "Surface plasmons and their role in the enhanced transmission of light through periodic arrays of sub-wavelength holes in a metal film," Phys. Rev. Lett. **92**, 107401 (2004).

124. J. C. Yang, H. Gao, J. Y. Suh, W. Zhou, M. H. Lee, and T. W. Odom, "Enhanced optical transmission mediated by localized plasmons in anisotropic 3D nanohole arrays," Nano Lett. **10**, 3173-3176 (2010).

125. M. G. Salt and W. L. Barnes, "Photonic band gaps in guided modes of textured metallic microcavities," Opt. Comm. **166**, 151-162 (1999).

126. M. Najiminaini, F. Vasefi, B. Kaminska, and J. J. L. Carson, "Optical resonance transmission properties of nano-hole arrys in a gold film: effect of adhesion layer," Opt. Express **19**, 26186-26197 (2011).

127. Y. Zhang, F. Vasefi, M. Najiminaini, B. Kaminska, and J. J. L. Carson, "Use of a radial angular filter array to estimate the position of an optically attenuating object within a turbid medium," Proc. SPIE **8230**, 82300A (2012).

128. Y. Zhang, F. Vasefi, M. Najiminaini, B. Kaminska, and J. J. L. Carson, "Angle-resolved spectroscopy: a tissue-mimicking phantom study," Proc. SPIE **8221**, 8221B (2012).

129. C. Escobedo, "On-chip nanohole array based sensing: a review," Lab Chip, http://pubs.rsc.org/en/content/articlelanding/2013/lc/c3lc50107h (2013).

130. C. Escobedo, S. Vincent, A. I. K. Choudhury, J. Campbell, A. G. Brolo, D. Sinton, and R. Gordon, "Integrated nanohole array surface plasmon resonance sensing device using a dual-wavelength source," J. Micromech. Microeng. **21**, 115001 (2011).

131. G. M. Hwang, L. Pang, E. H. Mullen, and Y. Fainman, "Plasmonic sensing of biological analytes through nanoholes," IEEE J. Sensors. **8** (12), 2074 - 2079 (2008).

132. C. J. Alleyne, P. J. R. Roche, S. Filion-Cote, and A. G. Kirk, "Analysis of surface plasmon spectro-angular reflectance spectrum: real-time measurement, resolution limits, and applications to biosensing," Opt. Lett. **36**, 46-48 (2011).

133. R. C. Gonzales and R. E. Woods, *Digital Image Processing*, 3rd ed, Harlow: Pearson/Prentice Hall, 2008.

134. L. V. Wang and G. Liang, "Absorption distribution of an optical beam focused into a turbid medium," Appl. Opt. **38** (22), 4951-4958 (1999).

135. S. Jacques, "Confocal microscopy," http://omlc.ogi.edu/animation/FfocusScatt.html.

136. S. J. Kim, K. V. Gobi, R. Harada, D. R. Shankaran, and N. Miura, "Miniaturized portable surface plasmon resonance immunosensor applicable for on-site detection of low-molecular-weight analytes," Sens. Actuators. B **115**, 349-356 (2006).

137. P. Pfeifer, U. Aldinger, G. Schwotzer, S. Diekmann, and P. Steinrucke, "Real time sensing of specific molecular binding using surface plasmon resonance spectroscopy," Sens. Actuators. B **54**, 166-175 (1999).

138. T. M. Chinowsky, S. D. Soelberg, P. Baker, N. R. Swanson, P. Kauffman, A. Mactutis, M. S. Grow, R. Atmar, S. S. Yee, and C. E. Furlong, "Portable 24-analyte surface plasmon resonance instruments for rapid, versatile biodetection," Biosens. Bioelectron. **22**, 2268-2275 (2007).